University of Pardubice

Jan Perner transport faculty

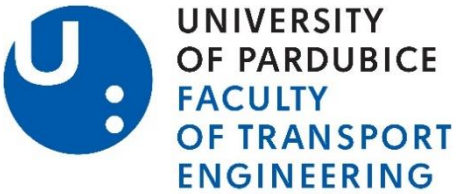

FRACTURE TOUGHNESS ANALYSIS OF AUTOMOTIVE STEEL IN PLANE STRESS

A thesis submitted for

The degree of Doctor of Philosophy

2021 Sunilkumar M R

Programme of Study:

P3710 Technique and Technology in Transport and Communications

Branch of Study:

3706V005 - Transport Means and Infrastructure

Supervisor:

Prof. Ing. Eva Schmidová, Ph.D.

Dissertation Title:

Fracture toughness analysis of automotive steel in plane stress

The doctoral dissertation has arisen at the supervising:

Educational and Research Centre in Transport (ERCT)

AUTHOR'S DECLARATION

I hereby declare:
This thesis was prepared individually. All the literary sources and the information I used in the thesis are listed in the bibliography.

I was familiar with the fact that rights and obligations arising from the Act No. 121/2000 Coll., the Copyright Act, apply to my thesis, especially with the fact that the University of Pardubice has the right to enter into a license agreement for the use of this thesis as a school work pursuant to § 60, Section 1 of the Copyright Act, and the fact that should this thesis be used by me or should a license be granted for the use to another entity, the University of Pardubice is authorized to claim from me a reasonable contribution to cover the costs incurred during the making of the thesis, according to the circumstances up to the actual amount thereof.

I agree with the reference-only disclosure of my thesis in the University Library.

In ……. on …../…../……...

Sunilkumar M R

ABSTRACT

DOCTORAL THESIS

Fracture toughness analysis of automotive steel in plane stress

Sunilkumar M R

University of Pardubice

Faculty of Transport Engineering

Department of Mechanics, Materials and Machine Parts

Supervisor: Prof. Ing. Eva Schmidová, Ph.D.

2021

Determination of fracture toughness of the automotive steels in the plane stress dominant condition (thin sheets) using essential work of fracture methodology is the research work's objective. The lack of proper international standards and complicated testing methodology has forced us to search for an easy and reliable alternative method. Most of the existing international standards to measure fracture toughness are primarily designed based on plane strain dominant condition (thickness constraint). A comprehensive literature survey has been done on the essential work of fracture (EWF) method, and the parameters affecting it are studied. The essential work of fracture (EWF) methodology has been successfully used to determine the fracture toughness of dual-phase (DP450) steel and Interstitial free steel. The feasibility of the EWF methodology in mode-2 and mixed-mode is tested. The effect of notch tip radius on the fracture toughness in the EWF methodology is analysed. Using the EBSD analysis, comprehensively all material parameters affecting the fracture toughness are studied. Fractographic analyses of the fractured surfaces after the EWF test is done using a scanning electron microscope (SEM). Local strain during the essential work of fracture methodology has been studied for the DP450 and the IF steel. Forming limit diagrams (FLD) and fracture forming diagrams (FFD) are constructed for the DP450 and the IF steel. A hole expansion test is also done for the DP450 steel and the IF steel. Finally, a thorough comparison is made between all the parameters mentioned above.

Keywords: Fracture toughness, EWF, Dual-phase steel, DP450, Interstitial free steel, Plane stress, FLD.

ANOTACE

DIZERTAČNÍ PRÁCE

Fracture toughness analysis of automotive steel in plane stress

Sunilkumar M R

Univerzita Pardubice

Dopravní fakulta Jana Pernera

Katedra mechaniky, materiálů a částí strojů

Školitel: Prof. Ing. Eva Schmidová, Ph.D.

2021

Cílem výzkumné práce bylo stanovení lomové houževnatosti ocelí pro aplikace na karoserie automobilů v podmínkách dominantní rovinné napjatosti (tenké plechy) hodnocením energie spotřebované rozvojem lomu. Nedostatek vhodných mezinárodních standardů a komplikovaná metodologie testování byly motivací pro hledání spolehlivé alternativní metody. Většina stávajících mezinárodních norem pro měření lomové houževnatosti je primárně navržena na základě dominantního stavu rovinné deformace. Proveden byl komplexní průzkum metod, založených na přímé evidenci energie při rozvoji lomu a studovány parametry, které ji ovlivňují. Pro stanovení lomové houževnatosti dvoufázové oceli (DP450) a oceli bez intersticí (IF) byla úspěšně použita metoda „Essential Work of Fracture" (EWF). V práci je ověřena aplikovatelnost metody EWF v různých režimech zatížení – tah, smyk, kombinovaný mód; analyzován je vliv poloměru vrubu na lomovou houževnatost.

Pomocí krystalografických analýz (EBSD) jsou komplexně studovány všechny parametry materiálu ovlivňující lomovou houževnatost. Fraktografické analýzy lomových ploch po EWF testu jsou provedeny pomocí rastrovacího elektronové mikroskopie (SEM). Pro oceli DP450 a IF byla studována lokální deformace vyvolaná během rozvoje lomu. Mezní diagramy tvařitelnosti (FLD) a diagramy meze destrukce (FFD) jsou konstruovány pro DP450 a IF ocel a doplněny o vyhodnocení zkoušek rozšiřování otvoru. Finálně je provedeno komplexní srovnání a analýza provázanosti výše uvedených parametrů.

Klíčová slova: lomová houževnatost, EWF, dvoufázové oceli, DP450, oceli bez intersticí, FLD, rovinné napětí.

ACKNOWLEDGEMENTS

I am deeply thankful to my supervisor Professor **Ing. Eva Schmidová, Ph.D.,** for her guidance, invaluable suggestions, technical expertise, and moral support. I am honoured to work under such a great human being with a dynamic research passion.

I want to express my endless gratitude to Professor **Dr. Neelakantha V Londe** (Mangalore Institute of Technology and Engineering, Moodabidre, Karnataka, INDIA) for his time and for offering helpful comments.

I also would like to convey my appreciation to **Ing. Jakub Zajíc** and **Ing. Filip Klejch** for their help in the laboratory, as well as their good friendship.

It is a pleasure to thank **Ing. Luboš Fidrmuc**, **Ing. Zdeněk Hošek, Ph.D**., **Ing. Jan Pánek** and **Ing. Petr Sobotka** for their unconditional support during the internship at Material technology and special measurements, ŠKODA AUTO a.s., Mladá Boleslav, Czech Republic. I am also grateful to **ŠKODA AUTO a.s**. company for allowing me to work.

I am incredibly thankful to **Ing. Tomáš Pilvousek, Ph.D.**, (ŠKODA AUTO a.s., Mladá Boleslav, Czech Republic) for providing materials, sharing results, and offering suggestions.

I want to thank **Professor Ing. Bohumil Culek**, CSc. for his help and effort during the conduction of my experiments.

I am also grateful to Professor **Ing. Petr Paščenko, Ph.D**., for his guidance and support in my study.

I want to thank **Dr. Fatih Bozkurt** (Eskisehir Technical University, Eskisehir, Turkey) for his suggestions and motivation throughout my study.

I want to thank the staff of the machine shop, but especially to **Ing. Pavel Svoboda, Ph.D**., **Jiri Tlustos**, **Jan Cernohlavek**, and **Martin Rehak**.

I want to thank my brother **Ing. Rathan Kumar M R** for his affectionate support throughout my study.

Finally, I would like to dedicate this thesis to my parents **Kanthamani** and **Ramesha M K.** This study would be nothing without their unconditional support and enduring love.

Sunilkumar M R
2021

LIST OF FIGURES

LIST OF TABLES

CONTENTS

NOMENCLATURE

δ_c^e	Crack tip opening displacement from EWF Test
a	Crack Length (ASTM E1820)
A_{50}	Elongation at the fracture (tensile test)
A_g	Elongation at ultimate stress (tensile test)
A_{pl}	Plastic area under the force-displacement (ASTM E1820)
B	Thickness of the sample(ASTM E1820)
b_o	Ligament length (ASTM E1820)
d_f	Final diameter at fracture (Hole expansion test)
d_o	Initial diameter of the hole (Hole expansion test)
E	Young's modulus
J_c	Critical *J*-integral
K_{1C}	Critical stress intensity in mode-1
L	Length of the ligament (EWF Test)
n	Strain hardening exponent
r_p	Plastic anisotropy
t	Thickness of the specimen (EWF Test)
v_f	Elongation at fracture
W	Specimen width (DENT)
W	Width of the specimen (EWF Test)
W_e	Essential work of fracture
w_e	Specific essential work of fracture
w_f	Specific work of fracture
W_f	Total work of fracture
W_p	Non-essential work of fracture
w_p	Specific non-essential work of fracture
β	Shape factor of plastic deformation (EWF Test)
ἑ	Strain rate (tensile test)
ρ_c	Critical notch tip radius (EWF Test)
σ_u	Ultimate tensile strength
σ_y	Yield strength
ψ^e	Crack tip opening angle from EWF Test
λ	Hole expansion ratio (Hole expansion test)
mm	Millimeter
μm	Micrometer

ABBREVIATIONS

AHSS	:	Advanced High Strength Steel
ASTM	:	American Society for Testing and Materials
BCC	:	Body Centred Cubic
BH	:	Bake Hardened
C(T)	:	Compact Tension
CNC	:	Computer Numerically Controlled
CP	:	Complex Phase
CTOD	:	Crack Tip Opening Displacement
DENT	:	Double edge notched tension
DIC	:	Digital Image Correlation
DP	:	Dual Phase
EBSD	:	Electron Back Scatter Diffraction
EDM	:	Electric Discharge Machining
ESIS	:	European Structural Integrity Society
EWF	:	Essential Work of Fracture
FFL	:	Fracture Forming Limit
FLC	:	Forming Limit Curve
FLD	:	Forming Limit Diagram
HAGB	:	High Angle Grain Boundary
HAZ	:	Heat Affected Zone
HSL	:	High Strength Steels
HSLA	:	High Strength Low Alloy
IF	:	Interstitial Free
IFHS	:	Interstitial Free High Strength
IPF	:	Inverse Pole Figure
IQ	:	Image Quality
ISO	:	International Organization for Standardization
KAM	:	Kernel Average Misorientation
LAGB	:	Low Angle Grain Boundary
M(T)	:	Middle Tension
ND	:	Normal Direction
RD	:	Rolling Direction
SEM	:	Scanning Electron Microscope
SEN(B)	:	Single Edge Notch Bent
SEN(T)	:	Single Edge Notch Tension
SFFL	:	Shear Fracture Forming Limit
SPIF	:	Single Point Incremental Forming
TD	:	Transverse Direction
TRIP	:	Transformation Induced Plasticity
TWIN	:	Twinning Induced Plasticity

1 INTRODUCTION

Automotive manufacturing has been a significant contributor to the rapid economic growth of most countries on earth since the 19th century. A faster mode of transportation helps in moving goods and people from one place to another at a higher speed in comparison to traditional methods. Lack of infrastructure and automotive technology in developing and underdeveloped countries have failed to transport goods and people from one place to another place quickly, which led to slower economic progress. The automotive industry has made significant and progressive changes from the initial days, and it is a never-ending process. Today, the automotive industry is going through unprecedented changes such as electric vehicles, hybrid vehicles, autonomous driving, hydrogen fuel cell vehicles, and many more.

In the dawn of the automotive industry era, manufacturing a vehicle was a mammoth task, and vehicles were produced in small batches. Later, in the mass production assembly-line era, manufacturers' interest shifted towards speed, comfort, efficiency, reliability, quality, cost, robustness, etc. Today, extensive competition and strict norms from the government forced the automotive industry to produce more efficient and safer cars. The vehicle's weight has a significant effect on the vehicle's efficiency, and the safety of the cars is equally essential. Increased safety norms from the government and higher crash safety rating expectations from customers are constantly growing. Both efficiency and crash test performance of the vehicles are significantly dependent on the material used for vehicle manufacturing. To reduce gross weight and simultaneously to increase the strength of the vehicle, automakers have started to use advanced high strength steels (AHSS) in the last few decades. These advanced high-strength steels have higher strength than ordinary steel and have a significantly higher strength-to-weight ratio.

AHSS steels are expected to have good manufacturability, formability, weldability, corrosion resistance, durability, and cost-effectiveness. Ordinary low carbon steel has good ductile properties; however, it has relatively lower strength. Advanced high-strength steels are developed with different microstructural phases and alloying elements. Generally, these steels have very high yield strength and ultimate strength. Some of the advanced high strength steels used in the automotive industry are dual-phase (DP) steel, martensitic steel, complex steel, ferrite-bainitic steel, transformation induced plasticity (TRIP) steel, twinning induced plasticity

steel, and many more. Generally, these steels have yield strength of more than 550 MPa (not a strict definition). Based on strength, fatigue, toughness, cost, and stiffness, these steels are used in various automotive components. Extensive research is needed on these steels in all areas to understand their mechanical properties entirely.

Fracture toughness parameters are critical for automotive steel. Fracture toughness has a direct influence on crashworthiness, formability, crack growth, and many more aspects. The majority of international Standards that measure fracture toughness are valid in plane strain conditions, i.e., for relatively thicker materials. A large portion of the automotive vehicle is made up of thin sheets. Determination of fracture toughness for thin sheets in-plane stress dominant condition is complicated, and there are no suitable and consistent international standards available.

Study and analysis of fracture toughness and microstructure of a few automotive steel sheets in plane stress dominant condition are among the primary focus of this research work. Dual-phase steel and interstitial free steel were chosen for the research work. These steels are extensively used in the automotive industry.

The essential work of fracture (EWF) method is used in this research work to find out fracture toughness of thin sheets in plane stress dominant condition. The EWF method and the parameters affecting it will be analysed. Double edge notched tension (DENT) samples with fatigue pre-cracks are used. The EWF experiments are conducted in a universal tensile testing machine in assistance with ARAMIS digital image correlation (DIC) technique. The tested samples are analysed in an optical and electronic microscope for fractographic study. Electron backscatter diffraction (EBSD) analysis is done for the tested samples. Finally, fracture toughness of the dual-phase steel and the interstitial free steel are analysed, and their microstructural behaviours are studied using the EBSD analysis.

1.1 Automotive steels

Since the beginning of the automotive industry, steel has been a primary choice of material for automobiles. Steel has excellent formability, weldability, strength, availability, and economic advantages. In the beginning, the automotive industry's primary focus was technological advancement rather than the vehicle's safety or efficiency. During the twentieth century's second half, due to increased road accidents, higher pollution caused by automobiles, and increased fuel prices forced the government in western countries to adopt standards on safety, emission, and efficiency. High strength steel (HSL) usage was limited due to a lack of technological development for mass-production and stamping-related problems.

In comparison to mild steels, high strength steels have low ductility, less formability, low fracture toughness, higher cost, and difficulty to stamp. Initially, high strength low alloy (HSLA) was the choice of material for higher strength due to manufacturing and technological problems associated with high strength steels like dual-phase and martensitic steels [1]. A trade-off between strength and formability was the deciding factor in the material selection of some complex components; they require extreme high stretching, which is fulfilled at the cost of strength.

In a crash, the material should absorb as much energy as possible and direct the crash forces in a controlled manner. The vehicle's design also plays a crucial role in distributing the energy and maximising the contact area during the crash. A controlled deformation of the crumple zone during the crash helps keep the structural integrity of the passenger cabin. Mechanical properties of the material play a dominant role in energy absorption, which intern depends on the microstructure of the material [2].

Mild steel is being used in the automotive industry extensively from the automotive industry dawn till now. Although the constant increase in usage of high strength steels (HSS) and new generation advanced high strength steels (AHSS), mild steel has its advantages. Some complex parts, exterior body parts, and sharp designs for styling purposes require high formability, often met by mild steel. Mild steel is relatively cheaper, easy to manufacture, and has good forming properties. The corrosive nature of mild steel is often suppressed by hot-dip galvanizing (zinc coating). The ferromagnetic nature of mild steel helps in easy sorting and recycling.

Interstitial free (IF) steel is another important type of steel used in automobiles, mainly for the door, fenders, sunroof, tailgate, and interior floor. Extreme low content of carbon (<0.005

weight percentage) and nitrogen in interstitial free steel makes an ideal choice for deep drawing applications. Vacuum degassing technology helps in keeping the carbon content below 30 ppm. Titanium and niobium are also added to form carbides and nitrides, further reducing the interstitial carbon and nitrogen atoms. IF steel yield strength is around 140 to 150 MPa, and ultimate strength of up to 280 MPa. The addition of solid solution strengthening elements such as manganese and silicon will significantly improve the strength of IF steel additionally up to 100 MPa but at the cost of formability. Cold-rolled and annealed sheets are widely used in the automotive industry. A strong texture {111}|| normal direction (ND) (γ-fibre) is desirable to get high formability and increase in carbon content or solid solution strengthening elements is detrimental to the {111}/{100} ratio (decreases). Along with the formation of carbides and nitrides, Niobium helps stabilize the formation of {111}|| normal direction crystallographic orientation of iron atoms[3].

Bake hardened (BH) steel can be any steel whose strength will be increased by strain hardening and subsequent thermal paint baking. Bake hardened steel has very low carbon content, which helps in forming complex parts. Later, during paint baking, the carbon atoms will be pinned with dislocations created during the forming. Combined work hardening and paint baking increase the strength of the material up by 100 MPa. However, non-uniform dislocations generated due to complex shapes in forming vary strength across the component. During paint baking, along with dislocation pinning of carbon atoms, precipitation hardening of carbides also increases the material's strength. Aluminium-killed and interstitial free steels can be bake hardened to increase dent resistance, fatigue resistance, and formability[4].

High strength low alloying (HSLA) steel entered the automotive industry in the 70s after the global oil crisis. HSLA steels met the requirement of reducing the vehicle's weight to increase efficiency due to their easy availability and cost-effectiveness. HSLA steels are a category of steels characterised by their unique mechanical properties rather than chemical compositions. HSLA steels have strength ranging from 260 to 520 MPa. HSLA steels are low carbon steels having alloying elements such as Titanium (Ti), Niobium (Nb), and Vanadium (V). HSLA steels increase their strength and fatigue resistance by grain refinement, precipitation hardening, and inclusions. A good balance between formability and strength is the critical property of this steel[5].

Dual-phase (DP) steel usage is constantly increasing in the automotive industry, and it is expected to grow higher in the future. Dual-phase steel has both ferrite and martensite phases;

the ferrite phase gives ductility to the steel, while the martensite enhances the strength. The strength of dual-phase steel is ranging widely from 400 to 1200 MPa. Both high formability and strength are the main advantage of dual-phase steel; also, it has good strain hardening ability, dent resistance, impact resistance, and bake hardenability. Generally, DP steel strength increases with an increase in the volume fraction of the martensite. The size, shape, and distribution of the martensite significantly influence the dual-phase steel's mechanical properties. Grain refinement and solid solution strengthening of the ferrite phase also help improve the strength of the material. Coarser distribution of the martensite is detrimental to fracture resistance, and extreme hardness of the martensite can be reduced by post quench tempering[6].

Advanced high strength steels (AHSS) are characterised by their microstructural multi-phases and high strength ranging from 550 MPa to 1200 MPa (non-standard). Steels such as dual-phase (DP) steel, complex steel (CP), transformation induced plasticity (TRIP) aided steel, twinning induced plasticity (TWIP) steel, and martensitic steels are classified as advanced high strength steels. Complex phase (CP) steels have ferrite and bainite microstructure phases along with a small amount of martensite and residual austenite. CP steel has a higher yield strength than dual-phase steel but has similar tensile strength. Some of the excellent properties of CP steel are high-energy absorption, good formability, and stretch flange-ability. Transformation-induced plasticity is an effect in which residual austenite transforms into martensite upon plastic deformation and thereby increasing the strain hardening effect. TRIP-aided steels have bainite and martensite in desired proportion to vary strength and elongation. TRIP-aided steels have high strain hardening rates and sustain high work hardening until enormous strains, enabling a good combination of strength and formability. TWIP steels have a high amount of manganese (15-25%) which helps in stabilising austenite at room temperature. A combination of low stacking fault energy and mechanical twinning inside the grain helps in achieving high strain hardening as well as excellent forming. The maximum strength of 1000 MPa can be achieved without significantly losing formability. Martensitic steels have a very high strength of up to 1800 MPa. The extreme strength is a result of the sizeable martensitic phase transformed from the sudden cooling of austenite. A small quantity of ferrite and bainite is also present. Hot forming is ideally suitable because of its high strength and low elongation. Post quenching tempering helps to increase ductility, toughness and reduce extreme hardness.

1.2 Stamping problems

The new era of advanced high-strength steels (AHSS) is entering the automotive industry to increase fuel efficiency, reduce emissions, and better crash performance. AHSS having better strength and formability, is an excellent replacement for conventional high strength steels. Figure 1.1 shows the strength versus ductility diagram of automotive steels. Steels such as interstitial free steel, mild steel, and bake hardened steel have excellent forming properties but have low strength. In contrast, the AHSS, such as dual-phase steel, TWIP steel, TRIP aided steel, complex phase steel, and martensitic steels, have a wide range of strength and ductility characteristics.

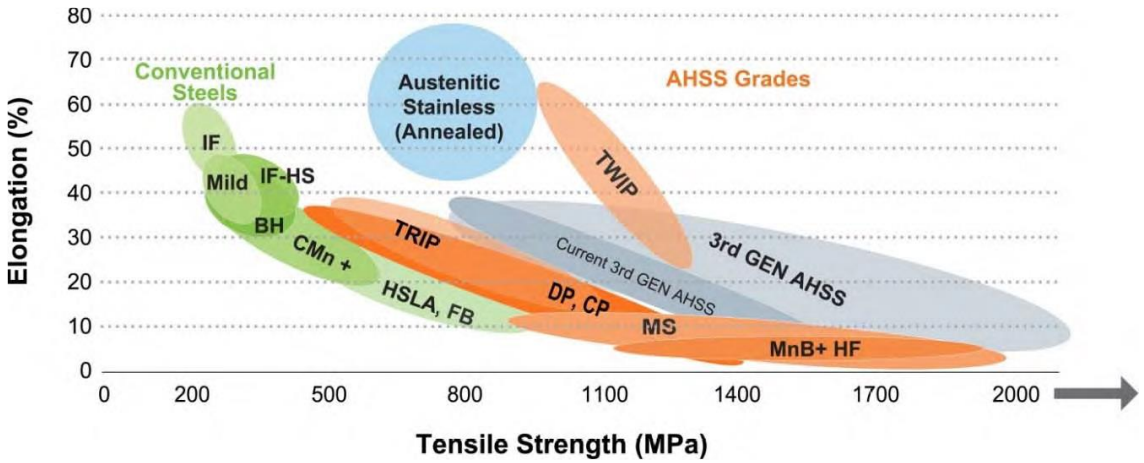

Figure 1.1 Strength versus ductility diagram for various automotive steels.[7]

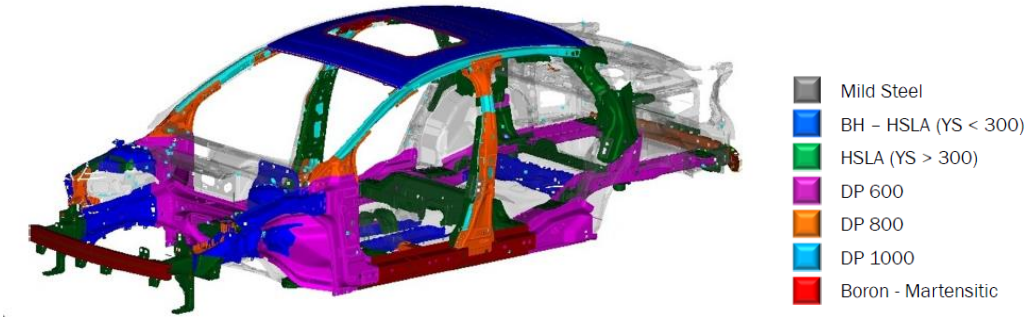

Figure 1.2 2013 Ford Fusion Body-In-White steel usage.[8]

Figure 1.2 shows the usage of various steels in the 2013 Ford Fusion. The use of AHSS is constantly increasing in the automotive industry. To meet the new norms, automotive manufactures increase the share of AHSS in every successive model. Steels that are upgraded from the previous generation with a slight change do not affect manufacturability significantly. However, new steel for a component often has many stamping-related problems like spring back effect, edge cracks (formed during shearing, trimming, and piercing), wrinkling of pressed

parts, and wavy stamped parts. Edge fractures appear during stamping for various reasons like abnormal die clearance, improper and worn-out tools, higher forces on dies and punches, and many more stamping-related parameters.

In contrast, conventional HSLA steels, mild steel, and interstitial free steels have low yield strength and strain hardening, making them easier for trimming, blanking, and shearing of sheets without local edge failures. High yield strength, high strain hardening, and hard phases like martensite in AHSS make them prone to edge fractures more often than conventional steels used in the automotive industry[9]. Figure 1.3(a) shows a typical edge fracture in DP980 steel after forming, and Figure 1.3(b) shows four general zones of sheared steel sheet across the thickness. Conventionally, a burr height of 10% of the material thickness is a limiting factor to check the quality of sheared edge. This conventional technique no longer applies to AHSS; AHSS are more prone to edge cracks than traditional steels.

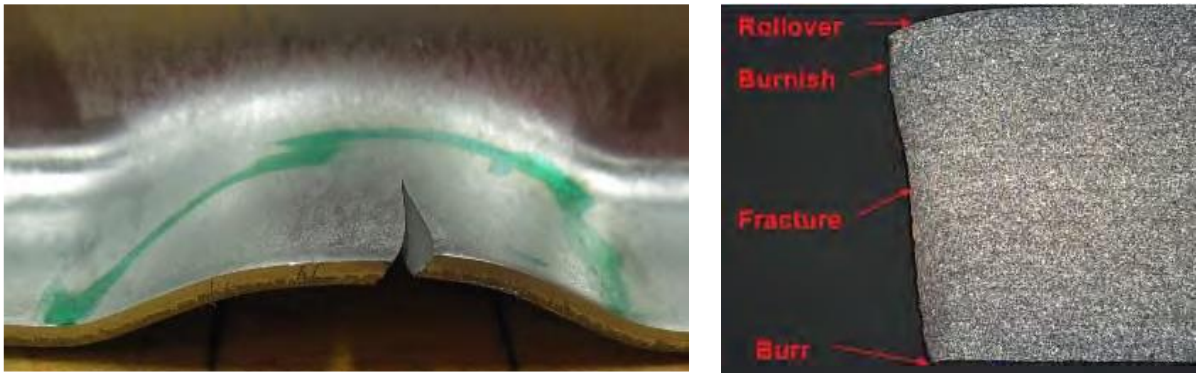

Figure 1.3 (a) An edge crack appeared in DP980 after forming; (b) Zones of the sheared edge. [7]

Forming limit curves (FLC) help identify a global failure limit caused during stamping (necking is the failure criteria). Edge fracture is a result of local failure of material rather than global failure. Two ways primarily cause edge fracture; first, issues related to stamping tools, dies, clearances, and second, problems related to the material. Excessive work hardening at the sheared edge and voids formation in martensite and ferrite interface during trimming is a source for edge fracture initiation. Edge fracture causes a considerable amount of scrap generation in AHSS. Fracture toughness of the material directly influences the edge crack formation and crack growth in subsequent forming processes. Measuring the fracture toughness of these steels would help in identifying the material's ability to resist the edge cracks. Fracture toughness of material would play a decisive role in material selection. In section 1.3, standard fracture-toughness measurement tests are discussed in detail.

1.3 Applicability of fracture toughness tests

The fracture toughness of a material is characterised in two ways, that are, single value and resistance curve methods. In the case of the single value method, parameters like *K* (stress intensity factor), *J* (J-integral), and *CTOD* (crack tip opening displacement) are used to define the critical point during crack growth. While in the case of the resistance curve method, the same parameters mentioned above are plotted against the crack growth. To determine the material's fracture toughness in a single value, generally, the material must have a flat resistance curve and follows cleavage fracture. Ductile materials often have a raising-resistance curve, which makes it challenging to characterise in a single value. In the raising-resistance curve, crack growth happens from a coalescence of micro-voids and consumes more energy as the crack grows (ductile fracture). American Society for Testing and Materials (ASTM), International Organization for Standardization (ISO), and many international organizations have developed standards for measuring fracture toughness. ASTM standards are widely accepted and used in the fracture mechanics' field. In 1970, ASTM first published the ASTM E399 standard to measure critical stress intensity factor K_{1C} in plane strain dominant condition. Later, ASTM published standards for various fracture toughness parameters and upgrading previous standards after every few years to reduce variations in the experimental results.

ASTM E399[10] *standard test method for linear-elastic plane-strain fracture toughness K_{1C} of metallic materials* is intended to determine the critical stress intensity factor K_{1C} of materials in linear elastic condition. To define the fracture toughness of a material using stress intensity factor K_{1C}, the material behaviour should be linear-elastic and plastic deformation around the crack tip should be sufficiently small. The word '*linear elastic*' is recently added to the standard's title (after 2013). The concept of plane-strain fracture toughness was always associated with the thick sections and plain-stress with thin sections. However, the plane stress and the plane strain conditions exist in all sections proportional to thickness. The updated E399 standard has less restriction on thickness compared to the previous E399 standards. Compact tension (C(T)) and single edge notch bent (SEN(B)) are widely used shapes in K_{1C} testing. For the C(T) specimen, the thickness requirement is $2 \leq W/B \leq 4$ (W is the width of the specimen and B is the thickness), the thickness of the specimen is dependent on the width, which intern depends on the ability to produce the most miniature sample to conduct the test successfully. To reduce the variation of K_{1C}, the ratio of crack length (a) to the specimen's width is kept between 0.45 to 0.55 ($0.45 \leq a/W \leq 0.55$). The value of provisional stress intensity factor K_Q calculated using the following equation.

$$K_Q = \frac{P_Q}{B\sqrt{W}} f\left(a/W\right) \tag{1.1}$$

P_Q is the load (not peak load) at which unstable crack growth begins, and it is determined by various methods depending on the load-displacement curve of the tested sample. $f\left(a/W\right)$ is the dimensionless geometric factor based on specimen shape, crack length, and width of the specimen. To validate the provisional stress intensity factor, the ligament length should satisfy equation 1.2.

$$(W - a) \geq 2.5\left(\frac{K_Q}{\sigma_Y}\right)^2 \tag{1.2}$$

Materials having high strength and low toughness are better suitable for this standard. In other words, higher toughness material or the material exhibit raising resistance to crack growth are unable to characterise using the K_{1C}.

ASTM E1820[11] *Standard Test Method for Measurement of Fracture Toughness* is primarily used to determine *J*-integral (J_{1C}) and crack tip opening displacement (CTOD). *J*-integral is a path-independent line integral around the crack tip and equivalent to energy release rate (*G*) for linear elastic materials. There are two methods to calculate critical *J*-integral (J_{1C}), the basic method and the resistance curve method. In the basic method, crack growth is not monitored, and many samples are loaded up to a varying amount of deformation. The value of the *J*-integral is calculated based on the initial ligament length. The J-integral is divided into two parts elastic and plastic. The elastic part of the *J*-integral is the first part of equation 1.3.

$$J = \frac{K^2(1 - \mu^2)}{E} + J_{pl} \tag{1.3}$$

Where *E* is the young's modulus, and μ is the poisons ratio. The stress intensity factor value is calculated using similar equations (Eq. 1.1) mentioned in the ASTM E399. The plastic section of the *J*-integral is calculated using equation 1.4.

$$J_{pl} = \frac{\eta A_{pl}}{B b_o} \tag{1.4}$$

Where η is the dimensionless constant (η=1.9 for SE (B) and η=2+0.522b_o/*W* for CT(T) specimen), A_{pl} is the plastic area under the force-displacement curve, and b_o is the ligament length at the beginning of the test. The *J*-integral value is plotted against the initial crack lengths (of the different samples) to find the critical *J*-integral (Figure 1.4). Unlike the E399 (for K_{IC}), the value of J_{1C} cannot be determined from a specific critical load (P_Q). An exclusion line is

drawn from a 0.2 mm crack extension with a slope of 2. The curve's horizontal limit is an intersection of the 1.5 mm exclusion line and the plotted data curve. The vertical limit of the curve is given by equation 1.5.

$$J_{lim} = \frac{b_o \sigma_Y}{7.5} \tag{1.5}$$

Where σ_Y is the average of yield and the ultimate strengths, the value of J_{1C} (critical *J*-integral) is chosen at the intersection of the 0.20 mm exclusion line and power-law regression line (Figure 1.4).

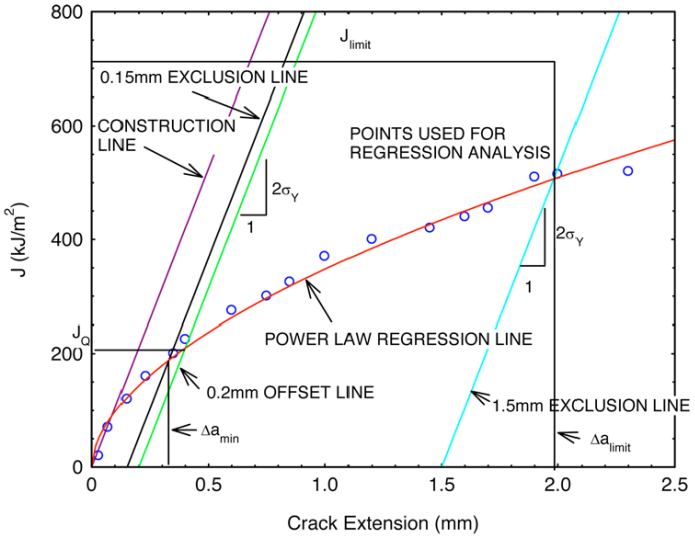

Figure 1.4 *J*-integral versus crack extension to determine J_{IC}. [11]

In the *J-R* curve testing method, the crack growth must be monitored, and the value of (*W-a)* is updated at several intervals. Crack growth is monitored from the unloading compliance method, potential drop method, or normalization method. In the unloading compliance method, the specimen is unloaded partially at several intervals before the final fracture. The value of (*W-a*) is calculated at each partial unloading cycle using compliance. The ASTM has given a polynomial equation to relate compliance and crack growth for standard specimen shapes. The potential drop method uses a change in the material's electrical resistance to find the crack growth, and the normalization method is used in dynamic tests. The *J*-integral value is calculated at several points (generally, equal to the number of partial unloading), and the *(W-a)* value is updated at each point. The elastic part of the *J*-integral is calculated like the basic method, and the plastic part is calculated from the following equations.

$$J_{pl(i)} = \left[J_{pl(i-1)} + \left(\frac{\eta_{pl(i-1)}}{b_{(i-1)}}\right)\left(\frac{A_{pl(i)} - A_{pl(i-1)}}{B_N}\right)\right] \times \left[1 - \gamma_{pl(i-1)}\left(\frac{a_{(i)} - a_{(i-1)}}{b_{(i-1)}}\right)\right] \tag{1.6}$$

Where η and γ are dimensionless constants, $(A_{pl(i)} - A_{pl(i-1)})$ is the area under the load-plastic displacement curve between two consecutive points.

ASTM E561[12] *Standard Test Method for K-R Curve Determination* published by the ASTM to determine stress intensity factor versus crack growth for thin sheets having a raising R-curve. Both the ASTM E399 and the ASTM E1820 restrict thickness or indirectly on the specimen's width. Most automotive body components are made up of rolled thin sheets; hence, they do not meet thickness constraints for the standard stress intensity factor (K_{1C}) and the *J*-integral (J_{1C}) tests. Thin sheets of ductile materials have a raising R-curve because of slant fracture, crack growth by coalescence of microvoids, and plane stress dominant crack-tip stresses. The point of instability on the R curve is dependent on the crack driving force, and hence, single point value toughness will be influenced by geometry and loading conditions. Generally, compact tension (C(T)) and middle tension (M (T)) specimens are widely used and accepted. Middle tension (M(T)) specimen is suitable for low strength and high toughness materials. During the testing, crack growth must be monitored either by optical measurement technique or compliance method. Due to the low thickness, the crack front variation across the thickness is low, and optical crack measurement is enough. The compliance technique uses two ways, which are compliance by partial unloading and compliance determined directly from the load-displacement curve. The actual crack length is inferred from compliance at the point of measurement using ASTM standard equations. The value of *K* is determined from equation 1.1. Generally, anti-buckling plates are used to keep the loading conditions in mode-1. Unlike the K_{1C} or *J-R* curve, the effective crack length is used instead of the actual crack length for the resistance curves. The effective crack length is calculated from Irwin plastic zone correction or secant compliance method. Iterative substitution of the *K* and the *a* is done until values converge. To verify the elastic nature of the un-cracked ligament, the length of the un-cracked ligament at any point must be equal to or greater than eight times the Irwin first order plastic zone, and it is given by equation 1.7

$$\left(W - a_p\right) \geq \frac{4}{\pi}\left(\frac{K_R}{\sigma_{YS}}\right)^2 \tag{1.7}$$

ASTM E561 *K-R* values depend on the material property and the thickness of the sample to be tested. A material with higher toughness may exhibit size-dependent values, and the sample size can be too large to meet the standard validity (Eq. 1.7). Unlike the K_{1C} and the J_{1C}, the *K-R* curves do not have a single critical value, and the transfer of values to an actual structure can be difficult and require extensive testing of a large variety of samples.

2 OBJECTIVE AND AIM OF THE RESEARCH WORK

2.1 Problem definition

Components used in automotive body-in-white are primarily hot or cold stamped steel. Ultra-high strength components are often hot-stamped, while components like the door, fender, roof, tailgate, etc., are often cold stamped. Cracks that appeared during stamping constitute a significant problem in sheet metals. Components with larger (visible) cracks are scrapped immediately; however, the microscopic cracks of length in orders of micrometers may grow in successive forming processes or in-service life. Forming limit diagrams (FLD) are used to set the limit for unstable plastic deformation during stamping. During stamping, the global failure of components by necking is identified using Forming limit curves (FLC) and simulation of stamping. However, **edge cracks formed in stamping are a local formability failure, which cannot be characterised by FLC.** The usage of advanced high-strength steel (AHSS) is constantly increasing in the automotive industry. The AHSS are more likely to be damaged by edge cracks than traditional mild steel or interstitial free steel. As edge cracks are non-repairable and non-reversible, components with edge cracks are often scraped instead of rework. Higher importance is being given to the maintenance of stamping tools to avoid the edge cracks of AHSS. Material selection is critical in preventing edge cracks, as it has the most significant influence on the formation of edge cracks. Fracture toughness of the material is an important parameter, which helps in characterising the crack resistance ability of the material during stamping as well as service life. Material having lower fracture toughness is more susceptible to edge cracks. Fracture toughness of material will depend on microstructural parameters like phase, grain size, the orientation of crystallography, inclusions, alloying elements, work hardening, etc. **Determination of fracture toughness of the material in its original thickness is essential for material characterisation.** Standard fracture-toughness measurement tests have direct or indirect restrictions on thickness, while the thickness of the sheet metal is determined by rolling (fixed sheet metal thickness).

2.2 Scope of the research work

Fracture toughness is a vital property of material, which helps select better the material for stamping applications. International standards for the measurement of fracture toughness

use parameters like stress intensity factor (K_{IC}), J-integral (J_{IC}), and crack tip opening displacement (CTOD), for the determination of fracture toughness. However, in all the standards, plain strain dominant condition (thicker sample) is utilised to avoid the effect of geometry and excessive plastic deformation. Determining the fracture resistance of a material in its original cross-section is essential and vital for material selection. Automotive outer body components are made up of thin sheets of thickness in orders of millimetres**. Fracture toughness of material in plane stress dominant condition (thin sheets) is an important parameter to be determined.** The fracture toughness of the material determines the material's ability to resist the formation of edge cracks and avoid further growth during the service life. Several steels are used in the automotive outer body components based on the requirement, cost, manufacturability, corrosion resistance, weight, strength, and many more factors.

Advanced high-strength steels are replacing conventional steels to improve strength and reduce the weight of an automobile. A more simple and effective method is essential for the measurement of fracture toughness of sheet metals. International standards like ASTM, ISO, etc., are expensive, tedious, and inappropriate for thin sheets. B. Cotterell first proposed the essential work of fracture (EWF) technique, and J. K. Reddel is relatively simple, and samples are prepared in their original thickness. European Structural Integrity Society (ESIS) has accepted the method for testing polymers. A small volume of research has been done on the method, especially for metals.

Dual-phase steel and interstitial free steel are widely used in the automotive industry. While interstitial free steel is being used for a long-time, dual-phase steel usage is continuously increasing.

2.3 Objective of the research work

- Study and analysis of Essential Work of Fracture (EWF) methodology for automotive body thin sheet metals.
    - Theoretical study of the methodology and application on sheet metals.
- Determination of fracture toughness using essential work of fracture (EWF) methodology for automotive body steels like dual-phase steel and interstitial free steel.
    - DENT specimens prepared from laser cutting and Electrical discharge machining (EDM) are used to determine fracture toughness in plane stress prevailing conditions.

    - Utilization of digital image correlation (DIC) technique to determine the local and global strain distribution during the EWF tests.
    - Microstructure and fractographic analyses using SEM and EBSD.
    - Comparison of the fracture toughness between the interstitial free steel and the dual-phase steel.
    - Determination of fracture toughness in mode-2 and mixed-mode.

- Optimization of geometrical parameters for a simplified method of testing.
    - Parameters like the sample's geometry, sample preparation method, fatigue crack, etc., are optimised for better results.
    - The consequence of notch tip radius and fatigue crack on the results are studied.

- Construction of Forming limit diagrams based on necking as well as the fracture.
    - Fracture forming limit (FFL) lines constructed from the same EWF tested samples.

2.3.1 Organization of report

Chapter 1 is about the problem with sheet metals' stamping and how standard fracture toughness tests cannot solve the problem. Chapter 2 is about the scope, need, and objectives of the research work. Chapter 3 is about the fundamentals of fracture mechanics. Chapter 4 is about the theory of essential work of fracture (EWF) methodology and its parameters. Chapter 5 is about forming limit diagrams (FLD). Chapter 6 is about the materials used and the methodology of experimentation. Chapter 7 is about the results and discussion of the EWF experiments. In chapter 8, microstructural analysis using EBSD and fractographic analysis in SEM are done. Chapter 9 is about strain analysis during the EWF test by DIC techniques, FLD results, and the Nakajima test results. Chapter 10 is about the conclusion of the research work.

3 FRACTURE MECHANICS

Researchers and engineers started their interest in fracture mechanics in the first half of the 20th century. In the beginning, materials selected for constructions, machines, and transportation, were based on the concept of strength alone. The fracture was not a crucial issue back then, because most materials used were wood, stone, and sand. At the beginning of the 20th century, Inglis first showed stress distribution in an elliptical hole and derived equations for stress concentration. Later, Griffith used thermodynamics laws to prove that energy available for crack growth is released from the strain energy stored in the body, which overcomes the surface energy of the material to propagate a crack. Series of Liberty ships were damaged during the second world war while sailing in the Atlantic sea and during docking. The ship's hull was welded instead of riveting to increase the pace of production during the war. Even though ductile material was chosen for the ship body, the hull broke into two parts in some cases. This incident triggered the research in fracture mechanics at the naval research laboratory lead by Irwin. Later, Paris, Westergaard, Rice, and many more researchers contributed to fracture mechanics development.

3.1 Linear Elastic Fracture Mechanics

Concepts developed in fracture mechanics before 1960 mainly focused on linear elastic materials. These concepts are only applicable to materials having linear elastic behaviours. However, with a slight modification, it will also be applied to ductile materials having low toughness. Elastic-plastic fracture mechanics (EPFM) and dynamic fracture mechanics are also developed on the extension of linear elastic fracture mechanics (LEFM) concepts. The study of basic concepts such as Griffith energy balance, Inglis concept, and stress intensity factor is vital in understanding fracture mechanics.

3.1.1 Stress Concentration factor by Inglis

The theoretical strength of a material is far higher than its experimental strength. Theoretically, materials will only fail when the atomic level's stress is more than the cohesive force. In reality, stresses at the atomic level are magnified by the presence of inclusions, cracks, and flaws. The ratio of local stress (at flaws) to nominal stress (far-field stress) is called the stress concentration factor (K_t). Inglis explained the stress concentration effect in a wide plate containing an elliptical hole, shown in figure 3.1. The ellipse's major axis is 2a, the minor axis

is 2b, and forces are applied perpendicular to the major axis. Stress at the point *'A'* (Figure 3.1) is given by

$$\sigma_A = \sigma\left(1 + \frac{2a}{b}\right) \tag{3.1}$$

Where σ is nominal stress, if *a=b*, the ellipse will become a circle and crack tip stress will be three times the nominal stress, i.e. $\sigma_A = 3\sigma$. For convenience, Inglis added radius of curvature ρ for the case of sharp crack.

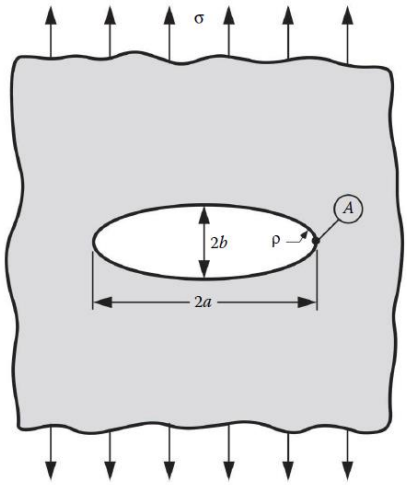

Figure 3.1 Stress concentration due to an elliptical hole.[13]

$$\sigma_A = \sigma\left(1 + 2\sqrt{\frac{a}{\rho}}\right) \tag{3.2}$$

$$\rho = \frac{b^2}{a} \tag{3.3}$$

For a sharp crack, *a>>b*, we can write the above equation as

$$\sigma_A = 2\sigma\sqrt{\frac{a}{\rho}} \tag{3.4}$$

As ρ decreases, the value of σ_A will continue to increase. For a sharp crack, ρ is close to zero and the σ_A will become infinite. No material would withstand infinite stress, and hence, this theory can't be applied to engineering problems. Inglis concept did not help to establish solid mathematics to solve the fracture problems; however, it did help in understanding the importance of a sharp crack[14].

3.1.2 Griffith energy balance

Griffith used the laws of thermodynamics to express energy associated with crack growth. For a crack to appear or an existing crack to grow, the total energy associated with the system remains the same, and the net change in energy is zero. Potential energy available in the system is utilised for crack growth. The potential energy supplied by the system must be higher than the surface energy of the material for a crack to grow. Consider a thorough crack in an infinite wide plate shown in figure 3.2 subjected to remote tensile stresses. *'2a'* is the length of the crack, *B* is the thickness of the plate[15].

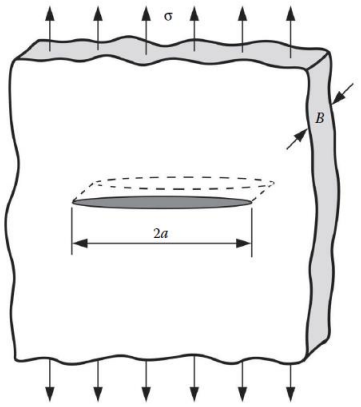

Figure 3.2 Crack in an infinite wide plate with remote tensile stresses.[13]

The net change in energy during an incremental crack growth is given by

$$\frac{dE_t}{dA} = \frac{d\pi}{dA} + \frac{dW_s}{dA} = 0 \tag{3.5}$$

Where E_t is the total energy of the system, π is the potential energy, A is the surface area of the incremental crack growth and W_s is the work required to create a new surface.

$$-\frac{d\pi}{dA} = \frac{dW_s}{dA} \tag{3.6}$$

The potential energy of the system is supplied by strain energy and external forces applied. The change in potential energy during the crack growth can be written as

$$\pi = \pi_0 - \frac{\pi\sigma^2 a^2 B}{E} \tag{3.7}$$

Where $\pi_0$is the potential energy of the un-cracked plate, and the second term is the lost in potential energy during the incremental crack growth. The loss in potential energy for the incremental crack growth is given by

$$-\frac{d\pi}{dA} = \frac{\pi\sigma^2 a}{E} \tag{3.8}$$

Work done to create two of the new surfaces is given by

$$W_s = 4aB\gamma_s \tag{3.9}$$

Where γ_s is surface energy and work done per incremental crack growth is given by

$$\frac{dW_s}{dA} = 2\gamma_s \tag{3.10}$$

Equating equations 3.6, 3.8, and 3.10,

$$\sigma_f = \left(\frac{2E\gamma_s}{\pi a}\right)^{1/2} \tag{3.11}$$

σ_f is failure stress, and the above equation can be used to solve engineering problems. However, Griffith's theory is most suitable for brittle materials. Along with surface energy, plastic deformation and heat dissipation also consume energy during crack growth. Irwin modified Griffith's equation to accommodate the plastic deformation and is given by

$$\sigma_f = \left(\frac{2E(\gamma_s+\gamma_p)}{\pi a}\right)^{1/2} \tag{3.12}$$

Where $\gamma_p$is the plastic energy per unit area and equation 3.12 applies to metals having linear elastic behaviour and plasticity should be confined to a small area around the crack tip and should not increase during crack growth. Also, Irwin expressed fracture resistance of material as energy release rate *G* (G_c-critical energy release rate) instead of surface energy or work of fracture.

3.1.3 Stress intensity factor

The stress intensity factor approach to crack growth is an extension of the Inglis concept. A single parameter, *stress intensity factor* (K_I), is enough to define the stress field around the crack tip. Consider figure 3.3, which describes the stress field around a crack in a polar coordinate system.

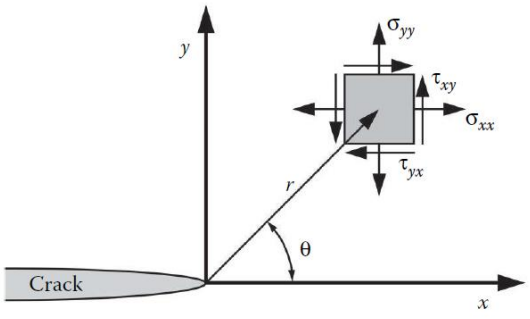

Figure 3.3 Crack tip stress field.[13]

Stresses in the ‘x’ and the ‘y’ directions at θ=0 are given by

$$\sigma_{xx} = \sigma_{yy} = \frac{K_1}{\sqrt{2\pi r}} \tag{3.13}$$

Where K_1 is the stress intensity factor (mode-1), stresses σ_{xx} and σ_{yy} vary singularly with $1/\sqrt{r}$. As *r* approaches zero, the value of the stress tends to infinity. These stress components are valid only for linear elastic, isotropic material and only near the crack tip, where $1/\sqrt{r}$ singularity dominates. Stresses far from the crack tip are dependent on remote boundary conditions. Stress intensity factor (K_1) can be determined by remote load and specified standard geometry. It is given by

$$K_1 = \sigma\sqrt{\pi a}\, f\left(a/W\right) \tag{3.14}$$

Where σ is the nominal remote stress, a is the half-crack length and $f(a/W)$ is the dimensional function of the geometry. At fracture, $K_1 = K_{1c}$, where $K_1$is the crack driving force and $K_{1c}$is the material resistance. K_{1c} is the fracture toughness of the material, which can be determined by the testing standard geometric samples. Stress intensity factor (K_1) can be related to the energy release rate.

$$G = \frac{K_1^2}{E} \tag{3.15}$$

3.2 Elastic-Plastic Fracture Mechanics

Linear elastic fracture mechanics (LEFM) is only valid for linear elastic materials, and non-linearity should be restricted only to a small area around the crack tip. Most of the engineering materials (metals) have nonlinear behaviour due to plastic deformation and strain hardening, making LEFM no longer valid for the most vital portion of engineering materials. Elastic-plastic fracture mechanics (EPFM) applies to materials having nonlinear deformation behaviour. Crack tip opening displacement (CTOD) and *J*-integral are two parameters used to describe the fracture toughness of material in the EPFM. Both the parameters are independent of specimen size and accommodate relatively large crack tip plasticity.

3.2.1 Crack tip opening displacement

While measuring the fracture toughness of high toughness materials, Wells observed a different crack tip behaviour. Which is, the crack's faces were moved apart, and the crack tip was blunted before the fracture. Crack blunting is mainly due to the plastic deformation around

the crack tip and is proportional to the material's toughness. Later, Wells defined CTOD as a parameter of fracture toughness.

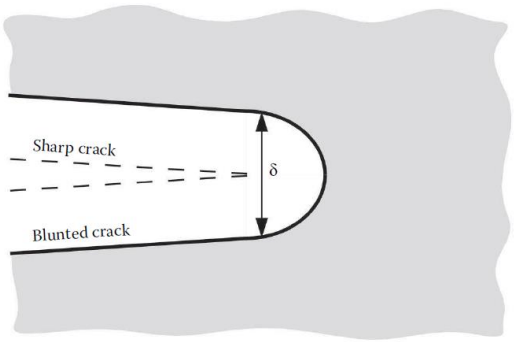

Figure 3.4 Blunting of a crack due to plastic deformation.[13]

CTOD can be defined as displacement at crack tip perpendicular to the crack plane, as shown in figure 3.4. For small-scale plasticity, it is possible to define CTOD in terms of *K* and *G*.

$$\delta = \frac{4K_1^2}{\pi\sigma_y E} \tag{3.16}$$

$$\delta = \frac{4G}{\pi\sigma_y} \tag{3.17}$$

Where δ is the crack tip opening displacement. CTOD for through crack is given by (strip yield model)

$$\delta = \frac{K_1^2}{m\sigma_y E} = \frac{G}{m\sigma_y} \tag{3.18}$$

Where *m* is a dimensional constant. To determine CTOD, *G* is replaced with *J*-integral in ASTM E1820. The ASTM E1290 and many international standards are used to measure the CTOD of metallic materials.

3.2.2 *J*-Integral

J-integral is one of the most important fracture toughness parameters for elastic-plastic materials. The non-linear behaviour of the elastic-plastic material is idealised with non-linear elastic materials to define *J*-integral. Both non-linear elastic materials and elastic-plastic materials will have a similar kind of deformation behaviour unless unloaded; only during unloading or cyclic loading, the material behaviour is different. *Deformation theory of plasticity* is used to define *J*-integral. *J*-integral can be used as both energy parameter and stress parameter at the crack tip. *J*-integral can be defined as the energy absorbed by the material to grow a unit crack length and is obtained by a contour line integral around an arbitrary path of a crack[16]. *J*-integral is given by

$$J = \int_{\Gamma} \left(w dy - T_i \frac{\partial u_i}{\partial x} ds \right) \tag{3.19}$$

Where Γ is an arbitrary contour line, w is strain energy density, T_i is traction vector components, and ds is the incremental length along the contour.

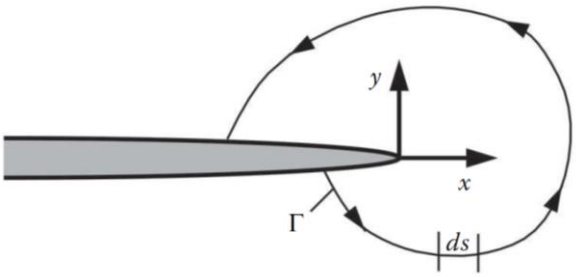

Figure 3.5 Crack tip contour path.[13]

Stress and strain components near the crack tip can also be expressed with the help of *J*-integral and are given by

$$\sigma_{ij} = k_1 \left(\frac{J}{r} \right)^{\frac{1}{(1+n)}} \tag{3.20}$$

$$\epsilon_{ij} = k_2 \left(\frac{J}{r} \right)^{\frac{n}{(n+1)}} \tag{3.21}$$

k_1 and k_2 are proportionality constants, r is the distance from the crack tip (polar coordinate), and n is the strain-hardening coefficient.

4. ESSENTIAL WORK OF FRACTURE

4.1 Fracture toughness dependence on thickness

Most international standards that measure fracture toughness are designed on plane strain dominant conditions. The primary reason is the large plastic deformation near crack-tip in plane stress prevalent condition (thin sheets). In thin materials, the plastic zone's size near the crack tip is larger than the thickness of the material. The plain strain tri-axial stress condition is relatively minimal in the case of thin materials. In the case of thin materials, the proportion of slant fracture is much more significant. In thick sections, due to the larger tri-axial stress zone, a significant portion of the triaxial stress state will come outside the plastic zone, except near the in-plane surfaces. This high tri-axial stress (in thick sections) will help in flat fracture and smaller shear lips near the surfaces.

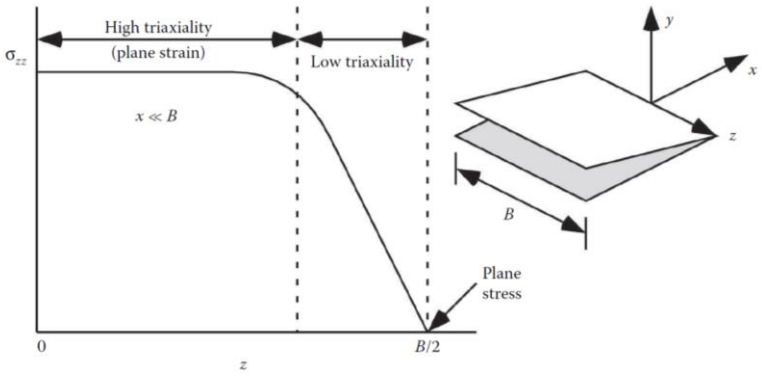

Figure 4.1 Transverse stress versus specimen thickness.[13]

Figure 4.1 shows the variation of stress σ_{zz} (stress in the thickness direction) at a crack tip in the z-direction. In thicker sections, at z=zero position, the crack tip stresses are in a maximum tri-axial stress state along the x-direction. As z increases (closer to the in-plane surface), the tri-axiality zone will become smaller and closer to the crack tip and falls inside the plastic zone near the in-plane surface. Near the surface, plane stress will prevail ($\sigma_{zz} \approx 0$) that leads to slant fracture and higher energy consumption. In the centre region, the triaxiality will prevail, which leads to flat cleavage fracture (microvoid coalescence is also possible), and the energy consumption is relatively low. This tri-axial stress state behaviour has a significant influence on fracture toughness measurement. The tri-axial state of stress at the crack tip helps in creating the weakest link and keeps the plastic zone smaller, which makes a thicker section ideal for geometry independent fracture toughness measurement. In thin specimens, the hydrostatic

stress (tri-axial stress state) varies with thickness. The sample thickness should be large enough so that the plane stress state will be a lot smaller than the thickness.

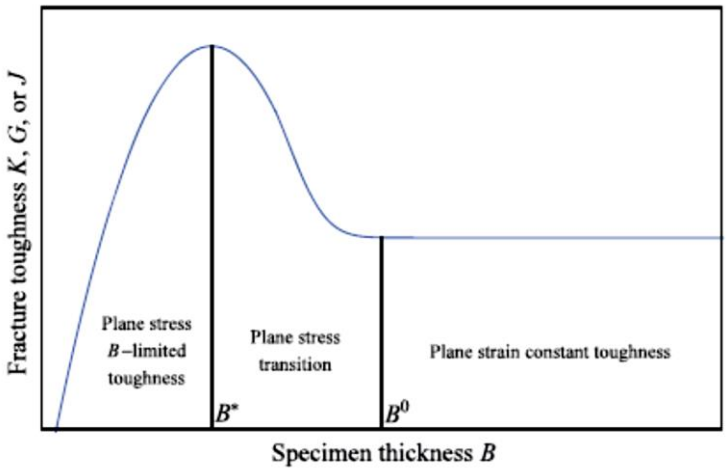

Figure 4.2 *K* versus specimen thickness.[17]

Figure 4.2 shows the critical stress-intensity factor dependence on the thickness of the specimen. In a very low thickness range, the stress intensity factor slightly increases with an increase in thickness, and later, it starts decreasing significantly as the thickness increases. The stress intensity factor will be insensitive to the thickness of the specimen after the critical thickness. To assess the fracture toughness as a truly geometry independent material property, the specimen thickness must be larger than the critical thickness. Due to the reason mentioned above, the measurement of fracture toughness for thin sheets is complicated. The closest international standard that helps measure the fracture resistance for thin material is the ASTM E561 *Standard Test Method for K-R Curve Determination*.

4.1.2 Plane stress fracture toughness: Confusion, misleading, and facts

Conventionally, the fracture toughness of a material is called plane stress and plane strain fracture toughness based on the thickness of the material. The fracture toughness of material in a thin section is higher than the thicker section of the same material. Beyond critical thickness, fracture toughness will be asymptotic with further increase in thickness. This thickness independent fracture toughness was traditionally called plane strain fracture toughness. At the same time, the fracture toughness of the thin material was called plane stress fracture toughness. ASTM E399 was called *Standard Test Method for Plane-Strain Fracture Toughness of Metallic Materials*. The advancement in three-dimensional finite element analysis gave a clear picture of stress triaxiality at the crack tip (clearly explained in section 4.1). In current ASTM standards, the term *linear elastic* is added to the heading to avoid confusion.

Even in thin sheets, the plane strain triaxiality exists, but only at the very vicinity of the crack tip. In thick sections, the pure plane stress state exists only at the surface of the sample. Whether it is a wide section or a thin section, both the plane strain triaxiality and the pure plane stress conditions exist in the material in relative proportions. Generally, high crack-tip triaxial stresses in the plane strain conditions lead to flat fracture, while the plane stress state leads to shear lipped fracture. If the sample thickness increases, it does not change the stress state completely from plane stress to plane strain. Instead, the stress state will change only in relative proportions. The conventional classification of plane strain fracture toughness and plane stress fracture toughness based on the thickness is somewhat misleading. The name of this proposed doctoral thesis is '*Fracture toughness analysis of automotive steel in plane stress.'* The word *plane stress* may also be misleading in the above context. The word *plane stress* means plane stress dominant stress state in this report. All the materials used in this research work are thin steel sheets (less than 1 mm). These sheets will have a dominant plane stress state at the crack tip; hence, the name *plane stress* is used and must not be confused with plane stress fracture toughness.

4.2 Essential Work of Fracture theory

K.B. Broberg[18] introduced the concept of crack tip regions and explained the hypothesis of an autonomous end region near the crack tip. According to Broberg, using regular fracture mechanics theories based on stress and surface energy concepts, it is irrelevant to explain the crack tip autonomous region, leading to singularity. This small autonomous crack tip region is the material property, and the plastic region outside this autonomous zone is not a material property. The plastic deformation around the autonomous region is dependent on geometry and loading conditions.

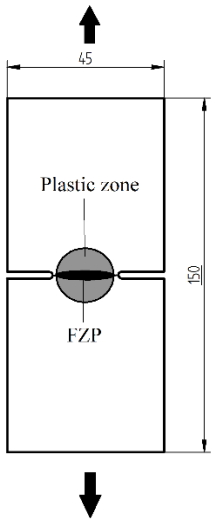

Figure 4.3 Schematic representation of fracture zones (mm).[19]

B. Cotterell and J. K. Reddel[20] extended Broberg's concept and proposed essential work of fracture concept (EWF). The authors divided the crack tip deformation zone into two separate zones, the fracture process zone (FPZ) and the outer plastic deformation zone. The fracture process zone (FPZ) in ductile materials is independent of geometry or loading conditions, and it can be characterised as true material property.

In brittle materials, plastic deformation is minimal, and linear elastic fracture mechanics theories are enough to characterise the fracture behaviour. Generally, ductile materials have sizeable plastic deformation, and energy consumption increases as the crack grow. In plane strain prevailing conditions, the amount of energy distributed to the fracture process zone and the plastic deformation zone is almost constant throughout the crack growth. However, in the case of plane stress dominant loading conditions, energy distributed for the plastic deformation is constantly increasing as the crack grows. As the crack extends, a more considerable portion of the energy is spent on the plastic deformation, while the amount of energy consumed in the

fracture process zone is constant. This rising energy consumption for plastic deformation will make linear elastic fracture mechanics inappropriate for thin sheets. Figure 4.3 shows the schematic representation of a Double Edge Notched Tension (DENT) specimen with FPZ and outer plastic deformation zone.

In the EWF method, the total energy absorbed by a specimen to fully fracture the specimen is taken as an output measurement. The energy consumed by the specimen is calculated by the area under the load-displacement curve and is given by

$$W_f = \int_0^{V_f} P dv \tag{4.1}$$

W_f is the total energy consumed by the specimen to break completely, v_f is the displacement at fracture, and P is the load. This total energy is divided into two parts, the first part is the energy consumed by the fracture process zone (FPZ) near the crack tip (W_e), and the second part is the energy consumed for the plastic deformation around the crack tip (W_P).

$$W_f = W_e + W_P \tag{4.2}$$

These energies are called essential energy and non-essential energy, respectively. The essential energy is the energy consumed by the fracture process zone, and it is proportional to the ligament area. The non-essential energy is the energy consumed by the outer plastic deformation, which is a function of volume.

$$W_f = w_e L t + w_p L^2 t \beta \tag{4.3}$$

Where w_e is specific essential work of fracture, w_p is specific non-essential work of fracture, L is the ligament length, t is the thickness of the sheet, and β is the plastic zone shape factor. The plastic zone shape factor is $\pi a/4b$, where a and b are the major axis and minor axis of the ellipse. For a circular shaped plastic zone, β will become $\pi/4$. If the whole equation (Eq. 4.3) is divided by the area of the ligament. Then,

$$w_f = W_f/Lt = w_e + w_p L \beta \tag{4.4}$$

Where w_f is specific work of fracture, it is a linear function of the ligament length with a slope of $w_p\beta$. Testing samples of different ligament lengths can calculate the value of w_e. Plot the results of w_f versus the ligament length L, and then w_e will be the intersection at zero ligament length. The w_f values are extrapolated to zero ligament length using a linear regression curve. Specific essential work of fracture is constant for a material thickness. Generally, specific

essential work of fracture increases with an increase in thickness[21]. Some basic requirements must be met during the experiments to validate the essential work of fracture methodology. The ligament should be fully yielded before the crack growth begins, and the ligament must be in a state of plane stress dominant condition. The crack growth before the complete yielding of the specimen leads to a contradiction of the methodology's fundamental principle. To keep the ligament in plane stress condition, the lower ligament length should be higher than three times the sample's thickness. The sample's upper ligament is restricted to less than one-third of the total sample width or Irwin's second-order plastic zone. The upper limit is to avoid the formation of two individual plastic zones. Inside the ligament, a quasi-plane strain condition will prevail at the crack beginning on either end. Equation 4.5 depicts the ligament length limits of the DENT sample for the EWF test. Figure 4.4 shows the variation of specific essential work of fracture against ligament length. The lower limit of the ligament length is governed by quasi plane strain conditions, while the upper limit is restricted by forming two independent plastic zone.

$$3t \sim 5t < L < \frac{W}{3} \tag{4.5}$$

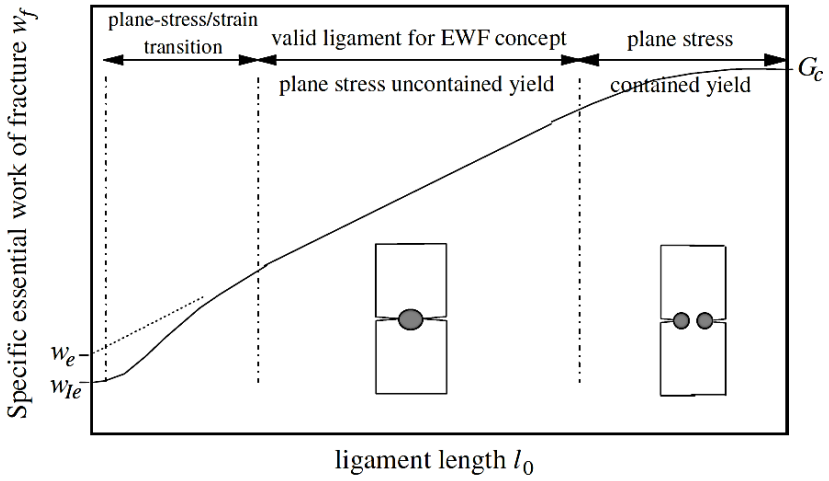

Figure 4.4 Specific essential work of fracture versus ligament length.[21]

B. Cotterell and J. K. Reddel also attempted to find out crack tip opening displacement (CTOD) using elongation at fracture in the EWF test. Crack tip opening displacement is a fracture toughness parameter mainly used in elastic-plastic materials. However, standard CTOD measurement has strict regulations on the sample's thickness to limit the size of plastic deformation. Several researchers have made attempts to calculate CTOD by considering the effect of plastic deformation. The specific essential work of fracture at the crack tip should be larger than the product of CTOD and average stresses at the crack tip.

$$w_e > \sigma\delta \tag{4.6}$$

Where σ is average stresses near the end region, and δ is crack tip opening displacement. B. Cotterell and J. K. Reddel used Tetelman and McEvilly[22] concept of maximum extension near the crack tip is similar to the general extension from the tensile test for that thickness and is given by $\delta = \epsilon_f t$. The w_e can also be expressed in terms of total elongation and yield strength.

$$w_e > 6.7 \times 10^{-4} \sigma_y \epsilon_f t \tag{4.7}$$

Where σ_y is yield strength and ϵ_f is failure strain obtained from a uniaxial tensile test, and t is the thickness of the sample. Elongation at fracture v_f is a linear function of the length of the ligament and is defined as follows,

$$v_f = \delta_c^e + \frac{\psi^e}{2} L \tag{4.8}$$

Where v_f is the extension of the specimen at fracture, δ_c^e is experimentally determined crack tip opening displacement, ψ^e is experimentally determined crack tip opening angle, and L is ligament length. Theoretical background and related experiments of EWF methodology are found in the literature[23–30].

4.3 Essential Work of Fracture parameters

4.3.1 Fracture Energy

B. Cotterell and J. K. Reddel[20] were the first researchers to define the essential work of fracture (EWF) methodology and defined the essential work of fracture as true material constant. During the test, the maximum load is reached after the yielding, and this should be proportional to ligament length within limits and is expressed as

$$P_{max} = kLt \tag{4.9}$$

Where *k* is proportionality constant, for ligament lower lengths (<3*t*), the above equation is not valid because of the shift of stress state towards the quasi-plane strain condition. The work of fracture defined as follows

$$W_f = \gamma k L v_f = w_e L t + w_p L^2 t \tag{4.10}$$

Where γ is the shape factor for load-displacement curves. Generally, the area under the load-deformation curve is used to calculate work of fracture using direct integration. The second term in equation 4.10 is not a popular method to calculate the work of fracture.

Y. Marchal and E Delannay[31] have worked on the influence of various parameters on the essential work of fracture methodology and established a particular relation among those parameters. They also discussed the consistency, applicability, and limitations of the methodology. They replaced *k* in equation 4.9 by σ_a(mean stress) over the ligament length. The value of σ_a can be used as an indicant of stress limits for upper and lower ligament lengths. Marchal observed the behaviour of the plastic deformation in different ligament lengths. In the smaller ligament lengths, the plastic deformation shape is circular and becomes more elliptical for the larger ligaments. After plotting the height of the plastic deformation perpendicular to the ligament length h versus the ligament length L for a sample thickness of 1.3 mm, the following power-law expression is established

$$h = kL^{0.69} \tag{4.11}$$

Where *k* is a constant. Marchal defined the shape factor used in equation 4.4 as $\beta = \frac{\pi a}{4b}$. For elliptical plastic deformation, *a* is the height of the plastic deformation, and *b* is ligament length. Marchal conducted the experiments of essential work of fracture on zinc alloy sheets. Marchal performed the experiments under varying parameters like the sheet's thickness, deformation

rate, grain size, and direction of rolling. As the thickness increases, the specific essential work of fracture also increases, with a slight reduction in the ligament's average stress. Finer recrystallized grains have higher specific essential work of fracture w_e than the courser grains. Higher deformation rates (high strain rates) will increase the specific work of fracture in his experiments.

B. Cotterell et al.[21] described two new terminologies within the fracture process zone, which are the necking and the final separation energies. During the testing, a reduction in thickness will happen independently of the specimen thickness. The height of the fracture process zone depends on the thickness of the sample. The energy absorbed in the fracture process zone's necking is directly proportional to the square of the sample's thickness, and final separation energy is directly proportional to the thickness of the sample. Specific essential work of fracture in terms of necking and final separation can be written as

$$w_e = \Gamma_0 + w_n \beta t \tag{4.12}$$

Where Γ_0 is work of final separation, w_n is work of necking, and β is the shape factor based on the shape of plastic deformation in the ligament.

The fundamental hypothesis of EWF methodology is that **Crack initiation** happens after full yielding of the specimen. Several researchers[24,25,31] have divided the total energy consumed by the sample W_f into two entities, which are the work of crack initiation W_i and the work of crack propagation W_t.

$$W_f = W_i + W_t \tag{4.13}$$

Figure 4.5 shows the schematic representation of the force-displacement diagram in an EWF test, along with the indication of crack initiation. According to Y.W. Mia and B. Cotterell[24], the specific energy consumed till the point of crack initiation is independent of the ligament length; this is because of lower crack tip opening displacement at initiation than propagation[32]. Unlike the specific work of fracture w_f, specific work of initiation w_i is not a linear function of ligament length. Generally, the amount of energy consumed to begin the crack, i.e., W_i, is smaller than the work of crack propagation W_t.

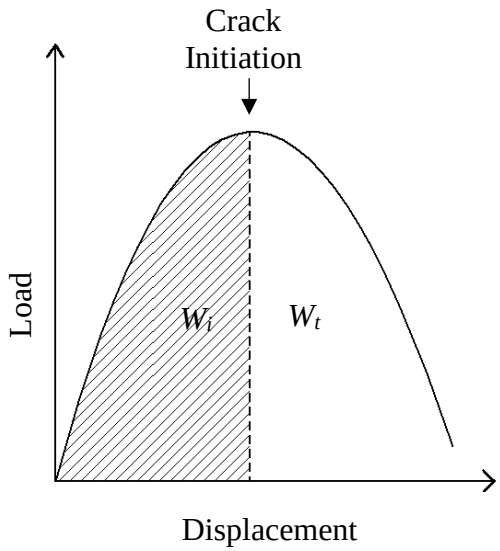

Figure 4.5 Schematic representation of force-displacement diagram in EWF test.

4.3.2 Experimental validation parameters

At the beginning of crack propagation, the state of stress will be quasi-plane strain dominant. However, as the crack propagates, the stress state will change into a plane stress-dominant state. This change of stress state condition will happen in all the ligament lengths. The change of stress state will affect energy consumption as crack propagate. Due to this shift of stress state, lower ligaments will have less specific work of fracture than higher ligament lengths, leading to a slight off-setting of values when plotted against the ligament length. The length of the stress transition (transitional length) is proportional to the thickness of the sample used for testing ($L \gg l_{trans}$). Generally, the transition length will be the same as that of the sample thickness. The lowest ligament length must be several times higher than the transition length so that the offsetting of W_f value for lower ligament lengths will be minimum. For the lowest ligament in the EWF test, a thumb rule of more than three to five times the specimen thickness is widely used. For the higher ligament lengths, the length of the ligament must be smaller than twice the second-order Irwin's plastic zone r_p, and it is given by

$$r_p = \frac{G_c E}{\pi \sigma_y^2} \tag{4.14}$$

The energy release rate will be asymptotic to specific work of fracture. The upper limits of the ligament length are given by

$$l_{max} < \frac{2E w_{fmax}}{\pi \sigma_y^2} \tag{4.15}$$

Where G_c is critical energy release rate (plane stress), it is replaced by specific work of fracture in equation 4.15[21].

Peak stress in the ligament during the essential work of fracture experiments gives important information about the stress state. Hills[33] performed an experimental analysis of plane plastic stress and expressed maximum stress in the ligament in terms of yield strength of the material, which is given by

$$\sigma_{max} = 1.15\sigma_y \tag{4.16}$$

Where σ_{max} is the maximum stress in the ligament and σ_y is the yield strength of the material. Equation 4.16 is an empirical relation used by various researchers to verify the state of plane stress. E.Q. Clutton[26][27] used the above relation in his work on the essential work of fracture for polymers. E.Q. Clutton observed that the maximum stress in the ligament was decreasing as ligament length increases. This change in maximum stress values is used for selecting upper and lower ligament lengths for the validity of plane stress conditions. J.G. Williamson et al.[34] used the statistical approach to validate the stress state as well as results. Instead of yield stress, the average of maximum stresses is used as the deciding parameter. The maximum stress values in the ligament should be in the range of $1.1\sigma_{avg}$- $0.9\sigma_{avg}$. The standard deviation of specific work of fracture w_f versus ligament length L is used in expressing the experimental variation and accuracy of the results. The basic distinction of J.G. Williamson's approach is usage of same experimental data rather than standard parameter like yield stress. Figure 4.6 shows the maximum stress versus ligament length, used by J.G. Williamson et al. to validate the experimental results. A pattern of stress behaviour is seen, i.e., decreasing of maximum stress as ligament length increases.

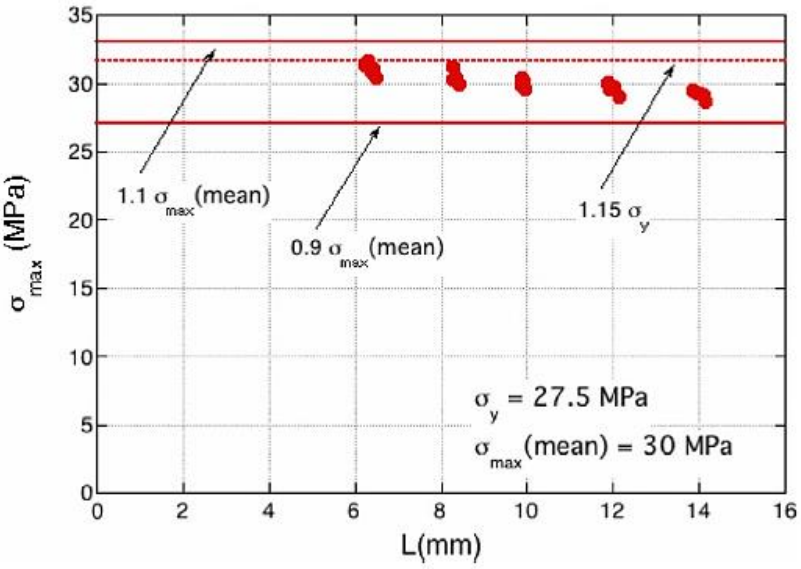

Figure 4.6 Maximum stress versus ligament to validate stress state.[34]

Y. Marchal et al.[35] used a **statistical approach** to validate the experimental results for lower ligament lengths connected with plane stress conditions. The values of specific work of fracture (w_{f1}, w_{f2}, $w_{f3,....}w_{fi}$) for cent percent confirmed (plane stress) ligament lengths ($L_1, L_2, L_{3,.....}L_i$) are first plotted. Later, the w_{fi+1} value for L_{i+1} is added to the plot, where $L_{i+1} < L_i$. If the addition of a value does not change the linear regression of (w_{fi} and L_i) significantly, then the ligament is in plane stress, and the result is valid. A probabilistic variable value '*p'* is used to indicate the linearity of each newly added value. If the *p*-value is greater than 0.05, then the ligament values are considered valid (no mixed mode). If two consecutive points fall outside the regression line, the lower limit is set before the first point. The same statistical procedure can be used to set the upper limit of ligament length also. The loss of linearity in specific work of fracture w_f is the deciding factor for validating the ligament lengths. Y. Marchal conducted EWF experiments for zinc, aluminum, and low-density polyethylene (LDPE). The lowest possible ligament lengths in terms of thickness are 2.6*t*, 4.5*t* and 6-7*t*, respectively. The Thumb rule suggested by B. Cotterell and J. K. Reddel[20] for ligament lengths is suitable for metals, not for polymers. Hence, the plane stress state depends on material properties also rather than thickness alone. Y. Marchal et al.[35] used the finite element method to find out the mean triaxiality for aluminum. Mean triaxiality stress is the average ratio of mean stress to von mises stress across the ligament. Unsurprisingly, the smaller ligaments show high triaxiality than the longer ligaments.

The number of samples (sample data) in EWF experiments plays a vital role in vital parameters like specific essential work of fracture and crack tip opening displacement. Y. Marchal et al.[35] conducted the essential work of fracture experiments for aluminum, zinc, and LDPE. The standard deviation of specific essential work of fracture Δw_e is plotted against the number of data points (Figure 4.7). The graph demonstrates that as the number of data points increases, variation of the specific essential work of fracture decreases. The aluminum and the zinc sheets require a smaller number of specimens to get more precise specific essential work of fracture w_e compared to the LDPE. The exact number of specimens required to get precise w_e is not constant and depends on various factors. Metals do require a smaller number of samples to get precise values in comparison to polymers. A higher value of work of fracture and uniform stress field along the ligament helps in achieving precise w_e in the metals. The standard deviation of specific essential work of fracture Δw_e depends on the dispersion of individual results, material property, machine accuracy, specimen quality, and w_e value. The recent literature works [36,37] on essential work of fracture suggests that a sample size of six to eight is sufficient for metals.

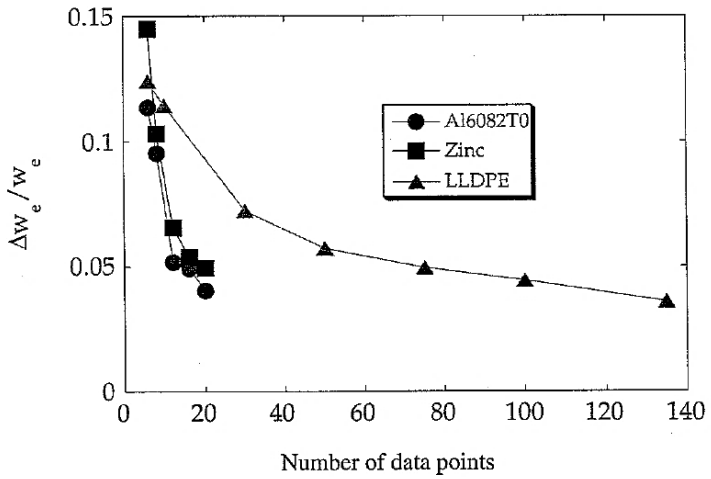

Figure 4.7 Specific essential work of fracture's standard deviation against data points.[35]

4.3.3 Crack Tip Opening Displacement (δ) of EWF method

The primary aim of essential work of fracture methodology is to find out specific essential work of fracture; however, several parameters can also be determined from the EWF tests. The total elongation at fracture v_f in the EWF test is a linear function of ligament length. Equation 4.8 gives the relationship between elongation at fracture v_f and the ligament length L. In a plot of elongation at fracture v_f in the y-axis versus ligament length L in the x-axis, the zero ordinate intercept will be the crack tip opening displacement (CTOD)δ_c^e. This CTOD is the distance between the sides of a propagating crack at the fracture process zone (FPZ). $\psi^e$is the crack tip opening angle (CTOA); it is the angle between the sides for a propagating crack. The conventional CTOD in fracture mechanics δ_c is different from the EWF CTOD δ_c^e. While the former is defined with limited plastic deformation and plane strain dominant conditions.

B. Cotterell and J. K. Reddel[20] defined the relations between elongation at fracture and specific work of fracture. The energy consumed by the specimen during the test is determined by the area under the load-displacement curve, and it can be expressed in terms of elongation at fracture as

$$W_f = \gamma P_{max} v_f \tag{4.17}$$

Where γ is a shape factor for the load-displacement curve and v_f is elongation at fracture (displacement determined from crosshead or extensometer). Above equation can be related to equation 4.3 and 4.9, which was discussed in section 4.2 and 4.3.1 respectively.

$$W_f = \gamma k L t v_f = \left(L t w_e + L^2 t w_p\right) \tag{4.18}$$

$$v_f = (w_e + Lw_p)/\gamma k \tag{4.19}$$

From the above expression, we can plot the fracture elongation as a function of ligament length *L*. Assuming a hypothetical condition of zero ligament length, the fracture elongation will equal the crack tip opening displacement. This crack tip opening displacement will be the zero intercepts of elongation at fracture versus ligament length plot. The crack tip opening displacement obtained from the above method will be depended on the fracture process zone, unlike the standard CTOD measurements.

The total elongation at fracture v_f can further be divided into two parts, viz, elongation at yield (crack initiation) and tearing elongation (tearing displacement).

$$v_f = v_i + v_t \tag{4.20}$$

Where v_i is the elongation or displacement at yielding or initiation (if crack begins after full yielding) and v_t is displacement due to tearing.

Cotterell et al.[21] modelled the necking of FPZ, the height of the fracture process zone can be estimated by considering the shape of the necking as trapezoidal and neglecting the transition lengths at the notch tip caused by stress state change,

$$h_f = \delta_c \frac{1-\epsilon_n+t_f/t}{1+\varepsilon_n-t_f/t} \tag{4.21}$$

Where h_f is the height of the fracture process zone, δ_c is critical crack opening displacement, ϵ_n is the strain at the neck region and t_f is the thickness of the sample after necking and final fracture.

4.3.4 Miscellaneous parameters

Several groups conduct round-robin experiments with ESIS[26]. The round-robin experiments' primary focus was to identify the accuracy, repeatability, and variables in essential work of fracture methodology. The first set of Ethylene propylene polymer samples of 100 µm thickness was prepared by a single group, i.e., similar specimen dimensional parameter. experiments on the EWF method and parameters affecting the EWF method. Appendix A.1 shows the parameters and results of the first set of samples. The first set of Ethylene propylene polymer samples of 100 µm thickness was prepared by a single group, i.e., similar specimen dimensional parameter. Appendix A.2 shows the parameters and results of the second set. In the second set, individual groups prepared the samples.

shows the parameters and results of the first set of samples. Appendix A.2 shows the parameters and results of the second set. In the second set, individual groups prepared the samples. The sharpness of the notch in the first set is not high. In the second set, individual groups prepared the notches, and quality varies among the different groups. In which h is the height of the sample between the grips and S is the standard deviation. The number of samples and test speed is almost similar in both sets. The material's yield strength is similar in all groups, and 27.4 MPa is the average value. The value of maximum stress in the ligament σ_{max} varies from 28 to 32 MPa. The value of w_e for the first set of samples is relatively high, which can be attributed to the notches' low sharpness. At the same time, the value of βw for both sets of samples is similar. In the first set of samples, groups 1, 7, and 8 have a higher standard deviation and Pearson correlation coefficient R^2 of less than 0.98. Meanwhile the specific essential work of fracture w_e is also away from the mean value for these groups. The average value of w_e for the first set is 44.3 kJ/m^2; group 1, 7, and 8 values are not close to the average value. In the second set of samples, it isn't easy to analyses the results as the notch quality significantly affects the results. Group 3, 4, and 6 have low standard deviation and Pearson correlation coefficient R^2 close to one. However, the values of specific essential work of fracture w_e is not similar. Standard deviation S is an excellent parameter to indicate the variation of experimental results. Since the actual value of w_e is unknown, it is extremely hard to validate the experimental results based on standard deviation alone. The value of σ_{max} is the least affected in all results. Based on the above results, the validation of results based on σ_{max} alone is not a safe approach. A combination of quality samples, similar testing conditions, low standard deviation, multiple samples (high sample data), and stress validity would give specific essential work of fracture close to real value.

Notch tip radius and the notches' quality significantly influence fracture toughness of material[38]. Experimental work conducted by V.V. Chaudhari et al.[39] and M. Faccoli et. al.[40] showed that fracture toughness of material increases as the crack tip radius increases. V.V. Chaudhari et al. conducted the standard ASTM E399 fracture toughness tests on cold-rolled low carbon steels with varying notch tip radius. Both the critical load and the crack tip opening displacement increased with an increase in the notch tip radius. M. Faccoli et al. conducted fracture toughness experiments on twinning induced plasticity (TWIP) steel, dual phase (DP) steel and Quenching & partitioning (QP) steel to determine J-integral using DENT specimen. The critical J-integral J_c increased with increasing in the notch-tip radius ρ. For the TWIP steel, J_c will be independent of ρ below the critical value of notch-tip radius ρ_c. M. Faccoli

used the DENT specimens and thinly rolled sheets, hence, critical notch-tip radius ρ_c concept may be valid for EWF tests also. ESIS TC4[26] round-robin experiments are conducted on PET (Polyethylene terephthalate) to assess the effect of notch tip radius and notch quality on specific essential work of fracture. Individual groups prepared notches using different methods. Appendix A.2 shows the type of notch, the notch-tip radius, and their specific work of fracture w_e. It is clear from the data that sharpest notch will have the lowest w_e. Group number 1 and 9 managed to produce 1 µm notch tip radius and have the lowest w_e. Group number 17 and 18 used razors to produce the notch and have relatively high w_e. It is evident from Appendix A.2 data that both notch quality as well notch-tip radius significantly affect specific work of fracture w_e. There is no standard formula or established relationship between fracture toughness and notch tip radius. The intensity of the effect of notch-tip radius on fracture toughness depends on material properties, loading conditions, fracture strain etc.

Table 4.1 Effect of notch quality and notch-tip radius on w_e.[34]

Laboratory	**Type of notch**	**Notch radius (approximate)**	w_e **(kJ/m^2)**
1	Scalpel	~1µm	20.1
	Die punch	50 µm	58.3
5	Sliding razor	<10 µm	31.2
9	Jig cut + razor	~1 µm	22.2
	Scissors cut	-	63.3
16	Razor	-	23.3
17	Razor	25 µm	40
18	Razor	~5 µm	34.3

The geometry of the specimen (width and height) does not have a significant influence on the results of essential work of fracture methodology. Double edge notched tension (DENT) specimens have been used by almost all researchers for EWF tests. DENT specimens do not need any anti-buckling supports, as the stress between ligaments is entirely transverse. There has been no standard to define the width and height of the sample. If the specimen's width is at least more than three times the ligament length, there will be no variation in results. Generally, as a thumb rule, the specimen's height is more than three times the width of the sample. According to the author's knowledge, no attempts have been made to conduct an EWF test other than DENT and SENT (single edge notched tension) samples.

4.3.5 Relationship between essential work of fracture and *J*-integral

Essential work of fracture (EWF) methodology and *J*-integral are developed based on two completely different hypotheses. The main result of the EWF methodology is the specific essential work of fracture w_e; it is the specific energy consumed in the fracture process zone (FPZ) to create two new surfaces. *J*-integral is the energy consumed by the material for a unit crack growth. J_i is the *J*-integral at the crack initiation, and J_{1c} is the critical *J*-integral (0.2 mm) during crack growth. Specific essential work of fracture w_e is the average value calculated over complete crack growth, while J_i and J_{1c} are calculated at the beginning and over a small length, respectively. Even though both the parameters are defined on an entirely different basis, several researchers have tried comparing them. Y.W. Mia et al.[24] and Marta Rink et al.[41] compared specific essential work of fracture w_e and J_i, as well as slopes of *J-R* curve and w_f versus *L* curve. Rice[16] defined *J*-integral as follows,

$$J = -\frac{1}{B}\left(\frac{dU}{da}\right)_v \tag{4.22}$$

B is the thickness of the sample, *U* is the input energy till *v*, *a* is the crack length, and *v* is the displacement. Equation of a linearly varying J-R curve (assumption) can be defined as

$$J = J_i + \frac{dJ}{da}\Delta a \tag{4.23}$$

Equating equations 4.22 and 4.23 and then integrating the resulting equation, the following relationship can be obtained

$$\frac{U}{BL} = J_i + \frac{1}{4}\frac{dJ}{da}L \tag{4.24}$$

Equations 4.24 and 4.4 are similar; the first term of both equations represents the specific work of fracture. According to equations 4.24, specific essential work of fracture w_e and J_i should be identical, as well as the slope of the J-R curve $\frac{dJ}{da}$ will be equivalent to $4\beta w_p$. However, βw_p is the energy density consumed by the sample to plastically deform outside of the fracture process zone and $\frac{dJ}{da}$ is the incremental energy consumed by the material to grow a crack. Marta Rink et al.[41] determined *J-R* curve for three different types of polymers using Bergy-Landes method for DENT specimens. Values of the w_e and the J_i are comparable, but the slopes of the *J-R* curve and the w_f vs. *L* curves are entirely different. Y.W. Mia et al.[24] also have similar results, that the J_i and the w_e were comparable and expressed their interest in comparing slopes of *J-R* curve and w_f vs. *L* curves in their future works. In the Bergy-Landes method, first, specimens having

different ligament lengths are loaded up to fracture, and load, displacement, and crack growth are monitored. A hypothetical constant crack length curve is interpolated from the load-displacement curves. A plot of strain energy versus crack length is constructed for constant displacement. Differentiation of the stain energy versus crack length curves gives *J* integral values for displacement (Equation 4.22). Finally, *J* vs. crack extension *a* and w_f vs. *L* plots are compared.

Another method for determining the *J* integral for DENT specimens is using the conventional fracture mechanics method without considering thickness restriction. The ASTM E1820 has specific restrictions towards the sample's width and thickness to keep plane strain dominant condition. The current ASTM E1820 standard does not have direct restrictions on the thickness, unlike previous standards. The width to thickness ratio suggested for CT(T) specimen is $2 \leq W/B \leq 4$. If the thickness constraint is neglected, the J-integral can be calculated for the DENT samples from conventional fracture mechanics formulas. Researchers have used both the basic procedure method and resistance curve methods to determine *J*-integral[25,32,42]. *J*-integral for the DENT specimen is given by Rice[43] as follows

$$J = \frac{K^2}{E} + \frac{1}{tL}(2\int P du_p - P u_p) \tag{4.25}$$

'*K'* is the stress intensity factor and is given by equation 4.26, and u_p is plastic displacement.

$$K = \frac{P\sqrt{\pi a}}{2tW\sqrt{1-\frac{a}{W}}}\left[1.122 - 0.561\left(\frac{a}{W}\right) - 0.205\left(\frac{a}{W}\right)^2 + 0.471\left(\frac{a}{W}\right)^3 - 0.190\left(\frac{a}{W}\right)^4\right] \tag{4.26}$$

Equation 4.25 can be used in the basic procedure method to determine *J* integral using multiple specimens. In the basic procedure method, multiple specimens are loaded to varying levels of crack growth. A *J-R* curve is constructed from the data obtained from the multiple specimens, and critical values are determined. However, to construct a *J-R* curve from a single specimen, equation 4.25 is not applicable, and crack growth must be monitored. An incremental *J*-integral can be calculated using the load-plastic displacement curve from the following equation.

$$J_n = J_{n-1} + \frac{2\left(A_{pl(n)} - A_{pl(n-1)}\right)}{t(l_{n-1} + l_n)} + \frac{2\left(K_n^2 l_n - K_{(n-1)}^2 l_{(n-1)}\right)}{E(l_{n-1} + l_n)} \tag{4.27}$$

Where A_{pl} is the plastic area under the load-plastic displacement curve. D. Frómeta et al.[25] have calculated the *J-R* curve for DENT and CT(T) specimens for a single specimen(Figure 4.8). The values of J_i and J_{1c} have yet to be verified for multiple ligament lengths.

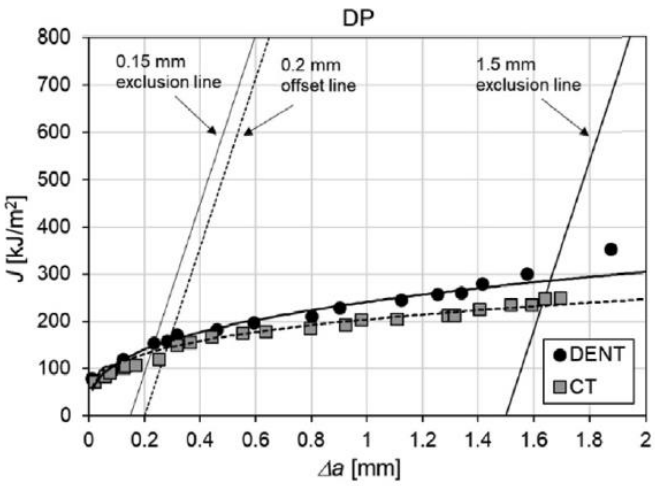

Figure 4.8 *J*-R curve for automotive dual-phase steel.[25]

4.3.6 EWF in mode-II and mixed-mode

The concept of essential work of fracture can also be extended to mode-2 and mixed-mode loading conditions. Several attempts have been made[44–46] to extend the EWF concept to mode-2 and mixed-mode. B. Cotterell et al.[44] used staggered double-edge notched specimen to produce the mixed-mode stress state in the EWF test and successfully found the results. In mode-2 and mixed-mode samples, the specific work of fracture is a linear function of ligament length. João P. Magrinho et al.[45] have successfully used the ASTM Standard B831-11[47] to produce mode-2 samples and staggered samples for the mixed-mode condition. Figure 4.9 shows the different types of EWF samples used by João P. Magrinho et al.[45] to get various stress states. The state of stress during crack initiation will be different from crack propagation. The state of stress in mode-2 and mixed-mode conditions may be better verified using finite element analysis. Specific essential work of fracture *'w_e'* and specific plastic work of fracture w_p are higher for staggered DENT and mode-2 samples. In the staggered DENT samples, the values of w_e and w_p increase with the increase in the angle between notches. In the mode-2 sample, the values of w_e and w_p are highest among all types of EWF tests.

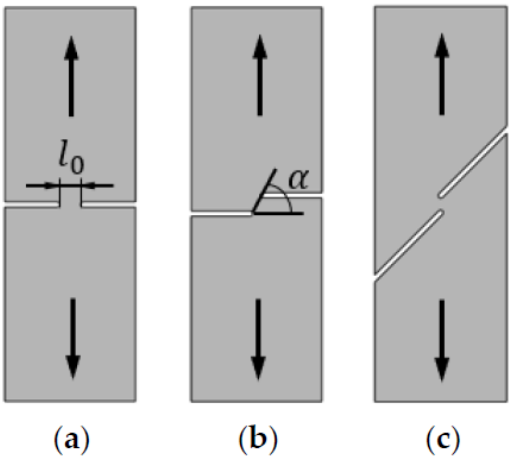

Figure 4.9 EWF samples for different modes of loading: (a) Mode-I; (b) Mixed Mode ; (c) Mode-II.[45]

5. FRACTURE FORMING DIAGRAMS

5.1 Forming limit diagram

Sheet metal's stamping failures occur in various forms such as necking, wrinkling, tearing, Luders bands, flange failures, folding, traces, corner fractures, orange skin surface, etc.[48]. These problems will not be solved by Forming limit diagram (FLD) alone, while the FLD's major focus is identifying necking in global behaviour. Parameters affecting forming can be classified into three ways, which are the material properties, the process parameters, and the strain-related parameters. Parameters like necking, deep drawing, spring back, stretching, strain localization, hole expansion, stretch flange ability, and tearing are related to the strain bounding parameters. **Forming Limit Diagram (FLD)** is a referential diagram constructed for an individual material to determine the limits of forming in sheet metals. FLD was first developed by S. Keeler for the first quadrant (tension-tension) in principal strain space[49]. Later, M. Goodwin extended the FLC curve for the second quadrant (tension-compression) of principal strain space[50]. FLD has Forming Limit Curve (FLC) to identify the point of failure by necking. Forming Limit Diagrams (FLD) are used in tool manufacturing for stamping, material selection for various forming applications, assess material quality for specific applications, etc. In the forming limit evaluation, the component's strain after forming is compared against the standard FLC of that material. The fundamental goal of FLD evaluation is to find out the maximum achievable straining of material for any major and minor strains without necking. FLD is not exclusive material property; it depends on the testing machine, test samples, analysis techniques, loading conditions, etc. Figure 5.1 shows the schematic representation of forming limit diagram with major strain in the y-axis and minor strain in the abscissa. Loading in uniaxial tension ($\varepsilon_1>0$ & $\varepsilon_2<0$) with positive major strain and negative minor strain can be achieved by a standard tensile test specimen. Plane strain condition($\varepsilon_1>0$ & $\varepsilon_2=0$), biaxial tension($\varepsilon_1>0$ & $\varepsilon_2>0$) and equi-biaxial tension($\varepsilon_1=\varepsilon_2>0$) strain states are obtained from different specimen width in Nakajima test.

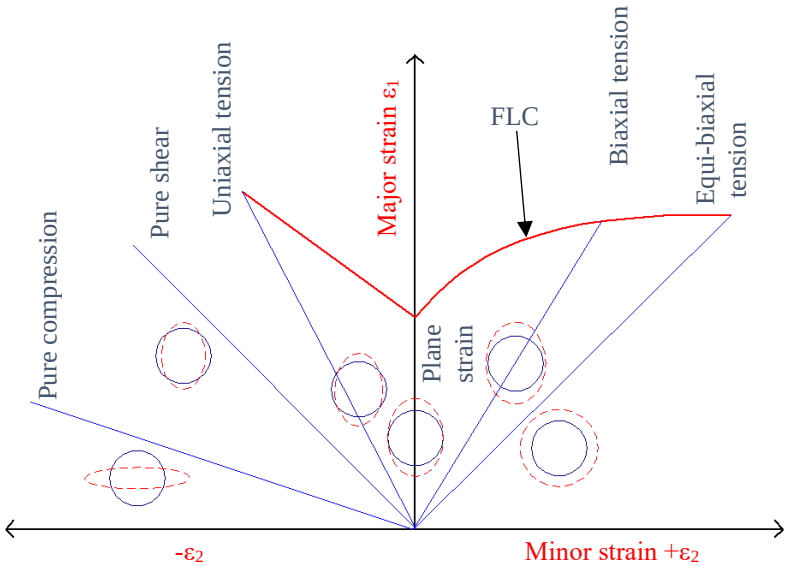

Figure 5.1 Schematic representation of Forming Limit Diagram (FLD).

5.2 Fracture Forming Limit curve

Forming limit curve (FLC) has been extensively used in many forming applications, including the automotive industry. In FLC, the point of necking in the strain loading path is considered as the limit of forming, and fracture limit was never a point of interest. During forming, after plastic instability by necking, the material will undergo rapid thinning with the decrease in load, and finally, fracture happens. The post necking behaviour and the fracture have gained the interest of several researchers in recent times. The complicated procedure and difficulties in identifying necking have shed interest in the fracture also. The general consideration of obvious necking before the fracture is not always true for all strain paths. In single point-incremental forming (SPIF), fracture happens without prior necking. Identifying the fracture limits have advantages in deep drawing, stretched parts, and high straining applications. The standard Fracture Forming limit (FFL) curve is plotted on major versus minor strain space, and it is falling from left to right with the slope of '-1'[51]. The condition to define the FFL is the maximum allowable thickness reduction before the fracture in mode-1. Like the FFL, the shear fracture forming limit (SFFL) curve is constructed in mode-2 fracture. The condition to define the SFFL is the maximum plastic in plane shear work per unit volume[52]. The SFFL is plotted in the second quadrant of principal strain space with a slope of '+1'. Figure 5.2 shows the schematic representation of FLC, FFL, and SFFL in principal strain space. Dotted lines at the end of the FFL and the SFFL indicate the threshold fracture; below the curved lines, the fracture will not happen. FLC is constructed from the standard ISO 12004-2, while FFL has no standard and can be constructed using tensile, Nakajima, and bulge tests. DENT specimens in tension are also used to construct the FFL, mainly in the intersection of FFL and SFFL

regions. Double edge notched shear specimens, and torsion specimens are used in the construction of SFFL[45,52]. In figure 5.2, WLC stands for wrinkling limit curve, which is constructed in compression strain path and helps in wrinkle analysis of formed components.

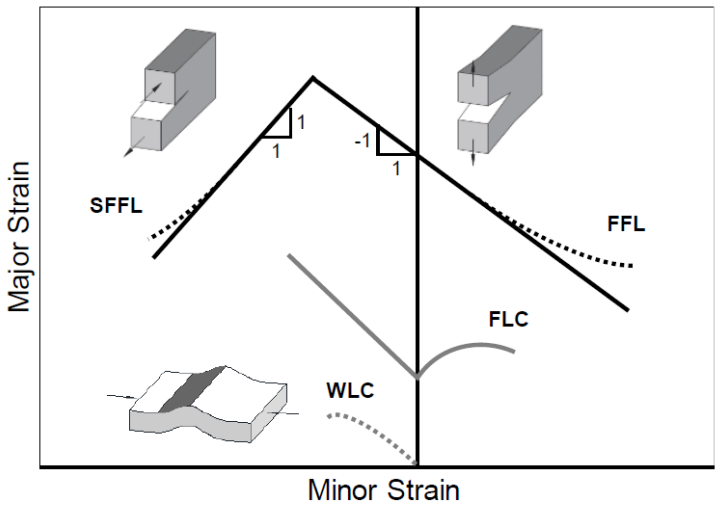

Figure 5.2 Schematic representation of forming limit curve (FLC), fracture forming limit (FFL), and shear fracture forming limit (SFFL) curve in principal strain space.[45]

Isik K. et al.[52] and João P. Magrinho et al.[45] have worked on FFL and SFFL in connection with ductile damage, fracture modes, void coalescence, and plastic instability. The critical damage criteria D_{crit} of void coalescence based on stress and strain till fracture in mode-1 is given by[53]

$$D_{crit} = \int_0^{\bar{\varepsilon}_f} \frac{\sigma_m}{\bar{\sigma}} d\bar{\varepsilon} \tag{5.1}$$

Where $\bar{\varepsilon}_f$ is the effective strain till fracture, σ_m is the mean hydrostatic stress and $\bar{\sigma}$ is the effective von mises stress. The same critical damage criteria can be expressed in terms of major ε_{1f} and minor ε_{2f} fracture strains,

$$D_{crit} = \frac{(1+r)}{3}\left(\varepsilon_{1f} + \varepsilon_{2f}\right) \tag{5.2}$$

Where *r* is the average plastic anisotropic coefficient. The position of FFL in the principal space is the straight-line falling from left to right with a slope of '-1'.

Critical damage criteria of void coalescence in shear mode D^s_{crit} is given by

$$D^s_{crit} = \int_0^{\bar{\varepsilon}_f} \frac{\tau}{\bar{\sigma}} d\bar{\varepsilon} \tag{5.3}$$

Where τ is shear stress. The same shear damage criteria can be explained in terms of major and minor fracture strains as follows

$$D_{crit}^{s} = \frac{1}{2}\frac{(1+r)}{(1+2r)}\left(\varepsilon_{1f} - \varepsilon_{2f}\right) \tag{5.4}$$

SFFL is a straight line from right to left with a slope '+1' and intersects FFL orthogonally.

5.3 Fracture strain

Strain paths of material till fracture in plane stress prevailing conditions are dependent on the stress field. Different strain fields can be obtained from varying sample shapes. G. Gruben et al.[54] have defined stress triaxiality σ^* and lode parameter μ using strain fields on the sample from digital image correlation (DIC) techniques. Figure 5.3 shows three different sample shapes used by G. Gruben to get different strain fields. Simple tensile specimen (figure 5.3(a)) has positive major and negative minor in-plane strains. At the same time, the shape of specimens in Figures 5.3 (b) and (c) are designed to produce plane strain and pure shear strain fields, respectively.

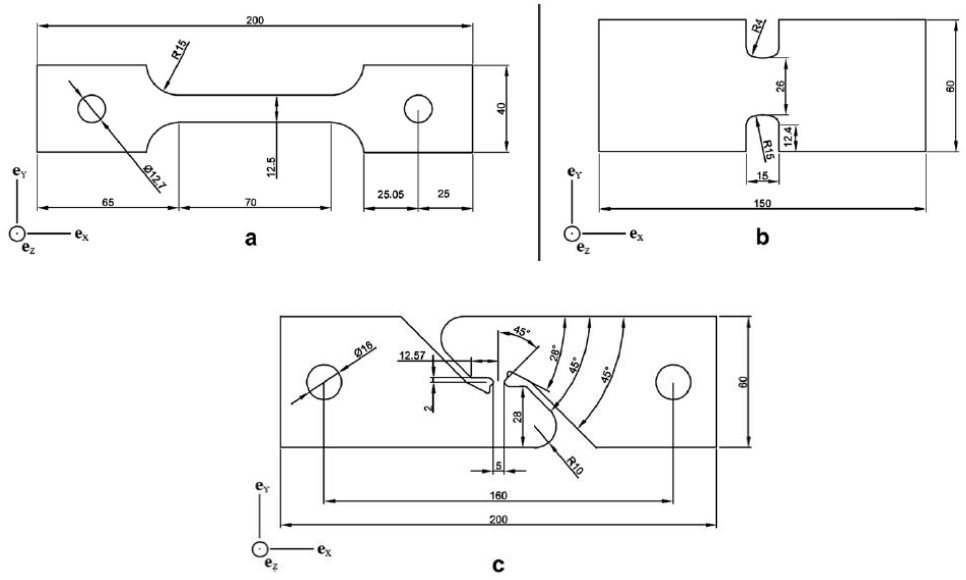

Figure 5.3 Geometry of the specimens (mm): (a) simple tension; (b) plane strain tension and; (c) pure shear strain.[54]

The logarithmic effective strain in the sample in terms of major and minor in plane strains can be explained as

$$\varepsilon_e = \sqrt{\frac{4}{3}(\varepsilon_1^2 + \varepsilon_1\varepsilon_2 + \varepsilon_2^2)} \tag{5.5}$$

Where ε_e is the effective logarithmic strain. Under proportional loading conditions, equivalent strain $\bar{\varepsilon}_e$ will be the same as effective logarithmic strain.

Stress triaxiality σ^* is the ratio of mean hydrostatic stress σ_m to equivalent von mises stress $\bar{\sigma}$. The stress triaxiality can be expressed in terms of strain increments as

$$\sigma^* = \frac{\sqrt{3}}{3}\frac{\beta+1}{\sqrt{\beta^2+\beta+1}} \tag{5.6}$$

Where β is the ratio of incremental minor strain to major strain $\left(\beta \equiv {}^{\Delta\epsilon_2}/_{\Delta\epsilon_1}\right)$. Similarly, the load parameter μ can also be expressed in terms of β. Load parameter is the stress deviator's third invariant and is given by

$$\mu = \begin{cases} 3\frac{\beta+1}{\beta-1} \text{ for } -2 < \beta \leq -{}^1/_2 \\ \frac{3\beta}{\beta+2} \text{ for } -{}^1/_2 < \beta \leq 1 \end{cases} \tag{5.7}$$

Figure 5.4 shows the strain paths calculated from DIC measurements for various strain fields (previously mentioned). Equivalent strain $\bar{\varepsilon}_e$, triaxiality σ^* and load parameter μ are calculated from major and minor in-plane strains from DIC.

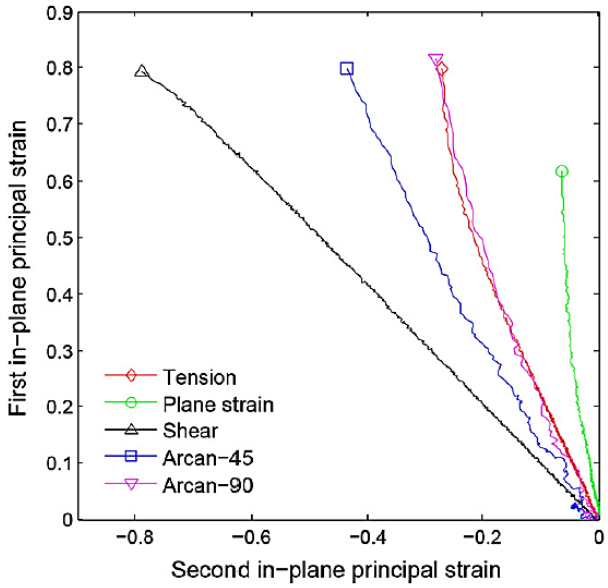

Figure 5.4 In-plane principal stresses calculated from DIC measurements for different strain fields.[54]

6. MATERIALS AND METHODOLOGY

6.1 Materials

Dual Phase (DP) steel

One of AHSS to first enter the auto industry is dual-phase steel or DP steel, developed in the mid-twentieth century and gained the most attention in the recent decade for various outer body and safety parts. DP steel has relatively simple thermomechanical processing and fewer alloying elements (quantity), making it more suitable for large-scale production. Primarily, dual-phase steel consists of ferrite and martensite phases with occasional bainite, residual austenite, and some carbides. The ferrite phase gives ductility, toughness, and formability. Meanwhile, the martensite phase gives high strength and strain hardenability. During plastic deformation, the ferrite undergoes much higher deformation in comparison to the martensite. Although inhomogeneous deformation at the phase level, macroscopically, DP steel has even deformation without any Luders band effect[55]. The volume fraction of the martensite influences the strength of DP steel. Generally, the bigger the martensite content, the higher will be the strength of the material. Along with the martensite volume fraction, various other factors also influence the strength of the dual-phase steel, which are the distribution of martensite (morphology), the grain size of the ferrite, geometric dislocations, alloying elements, and crystallographic orientation. The ferrite grain size also affects overall strength; more refined ferrite grains lead to higher strength and strain hardenability[56]. Dual-phase steel is better suited for outer body stamped components because of its high ultimate strength (attributed to martensite) to low yield strength (attributed to the presence of ferrite), and high initial strain hardening, which makes it ideal for forming applications. Generally, DP steel sheets are produced by both cold rolling and hot rolling based on application. In automotive DP steel, ferrite-pearlite or ferrite-bainite is first cold-rolled and subjected to the continuous cooling process. It consists of heating them to a temperature between A1 and A3 temperatures, followed by quenching below the martensite start temperature. Lower strength DP steels are used in the roof, door, side body, fender, floor panel. High strength DP steels, which are generally hot-rolled, are used in the B-pillar, seats, roof rails and other structural parts. G. Ingarao et al.[57] have worked on spring-back effects of dual-phase steels (DP1000 & DP600) using the finite element method. W. Mocko et al.[58] have worked on the effect of pre-fatigue and strain rate on DP500 steels and found that yield strength increases with an increase in initial loading

cycles. Anindya Das et al.[59] have worked on strain rate sensitivity of DP600 and DP800 steels and found that both yield and ultimate strength increase with the increase in the strain rate. Research work related to the dual-phase can be seen in the following literature [60–62].

DP450 steel is taken here for the analysis, which is a relatively lower strength dual-phase steel. The chemical composition of DP450 steel used in our research work is given in Table 6.1. Figures 6.1 and 6.2 show the microstructure of the DP450 steel in both optical microscope and scanning electron microscope, respectively. The martensite is mainly present along the grain boundary and relatively smaller in size compare to the ferrite. The shape of the martensite and the ferrite are not uniform. It has a carbon percentage of 0.06-0.015 wt.%, which helps the formation of the martensite, manganese helps stabilize the austenite and strengthening the ferrite. Good weldability is expected due to the low carbon content. A relatively high portion of the manganese helps in grain refinement also[63]. Silicon helps to transform the ferrite, and chromium helps to avoid the formation of bainite or pearlite during quenching.

Table 6.2 shows the mechanical properties of the DP450 steel from standard tensile tests. The ultimate strength is almost the same in all directions, and it is 500 MPa. The plastic anisotropy is relatively low, and it is maximum along the rolling direction (RD). Figure 6.3 shows the engineering stress-strain curves for the DP450 steel. Section 6.2.1 explains the detail of the standard tensile test. Continuous yielding and absence of any visible yield point are characteristic of the curve. The DP450 steel deformed uniformly after initial strain hardening without significantly changing the stresses. The elongation at fracture is maximum along the rolling direction and minimum along the 45º to rolling direction.

Table 6.1 Chemical composition of DP450 in weight percentage.

Sample	C	Mn	Si	P	S	Cr	Ni	Cu	Al	Ti	Fe
DP450	0.083	1.72	0.026	0.021	0.0049	0.209	0.0097	0.014	0.056	0.163	~97 %

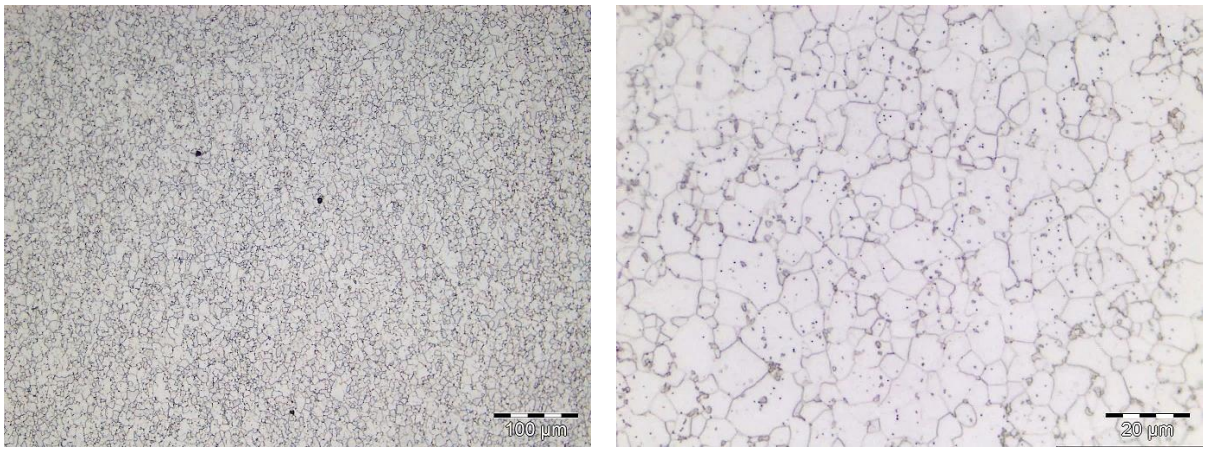

(a) (b)

Figure 6.1 Optical microscope micrographs of DP450 steel at different magnification: (a) 250; (b) 1000.

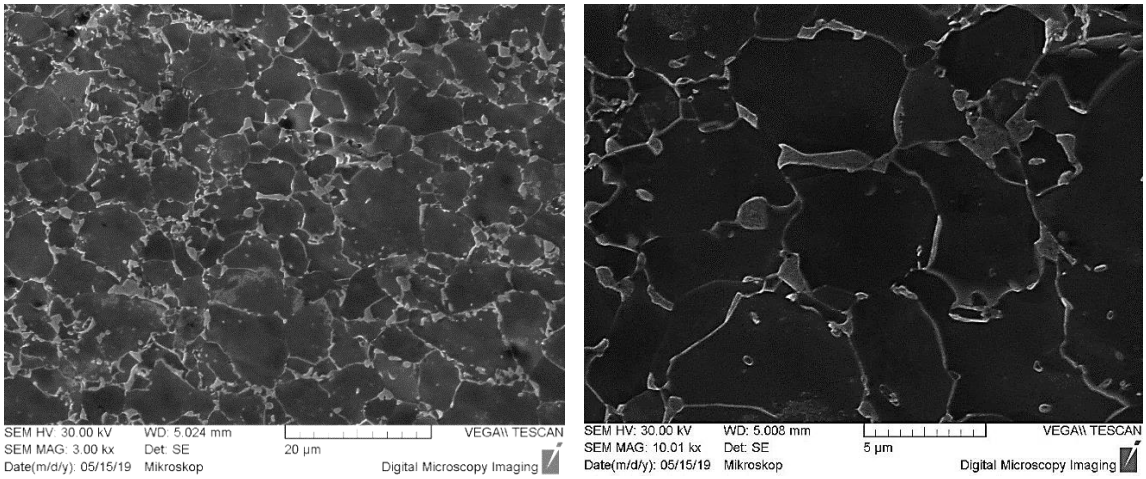

(a) (b)

Figure 6.2 SEM microstructure of DP450 steel at different magnification: (a) 3000; (b) 10000.

Table 6.2 Mechanical properties of tested DP450 steel from standard tensile tests.

Angle to RD	σ_y(MPa)	σ_u(MPa)	A_g%	A_{50}%	n	r_p
0º	308	499	19.46	30.48	0.18	0.83
	299	499	19.69	29.28	0.19	0.67
45º	262	504	19.03	26.68	0.18	0.52
	327	502	16.67	20.81	0.17	0.66
90º	308	499	18.62	27.06	0.18	0.47
	309	499	18.95	30.07	0.18	0.68

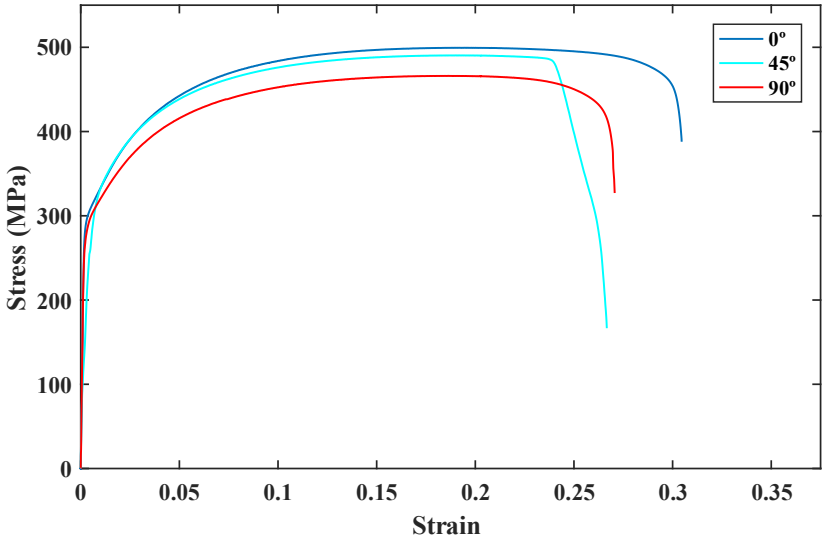

Figure 6.3 Engineering stress versus strain curves for DP450.

Interstitial free (IF) steel

Ultra-low carbon and other solute elements in the IF steel make it an excellent choice for forming applications. Low yield and ultimate strengths coupled with higher plastic anisotropy value (r_p) are characteristics of the IF steel. In low carbon steels, solute atoms such as nitrogen and carbon help strain localization and reduce dislocation density[64]. In the low carbon steels, the solute nitrogen and carbon atoms are pinned to dislocations, which leads to the formation of Luders band. Hence, IF steel is a good alternative for low carbon steel. The strength of IF steel can be increased by solid solution strengthening, and the steel is called IFHS (Interstitial free high strength) steel. Cold rolling followed by recrystallisation helps in achieving better formability and a good r_p-value. Increased carbon content in the IF steel is detrimental to the {111}/{100} ratio and thereby reducing the r_p value[65]. Nitrogen content also has a similar effect on crystallographic orientation in the IF steels. Titanium and niobium are added to reduce the carbon and nitrogen by forming carbides and nitrides, respectively. The niobium also suppresses the formation of {100} texture by lowering the austenite recrystallization temperature. A small amount of Sulphur helps in the formation of carbo-sulfides before the titanium carbides, which helps for recrystallization in {111} texture[3]. Alloying elements such as manganese, copper, chromium, and phosphorus can also be added to increase the IF steel's strength, and manganese is a highly preferred choice. However, excessive addition of the manganese will be deleterious to texture in the {111} direction[66] (all the above crystallographic direction is mentioned with respect to normal direction).

Table 6.3 shows the chemical composition of elements by weight percentage of the IF steel used in this work. As expected, shallow carbon and nitrogen contents are present and low strength is attributed to the absence of solute elements. Figure 6.4 and Figure 6.5 show the IF steel's microstructure in both optical microscope and scanning electron microscope, respectively. Table 6.4 shows the mechanical properties of the IF steel from a standard tensile test. The higher r_p value is characteristic of good formability. Figure 6.6 shows the engineering stress versus strain curves for the IF steel. The continuous yielding and the absence of any visible yield point are characteristics of the curves. However, the 45º to the rolling direction sample has a rough transition during yielding. The elongation at fracture is maximum along the rolling direction and minimum along the 90º to rolling direction.

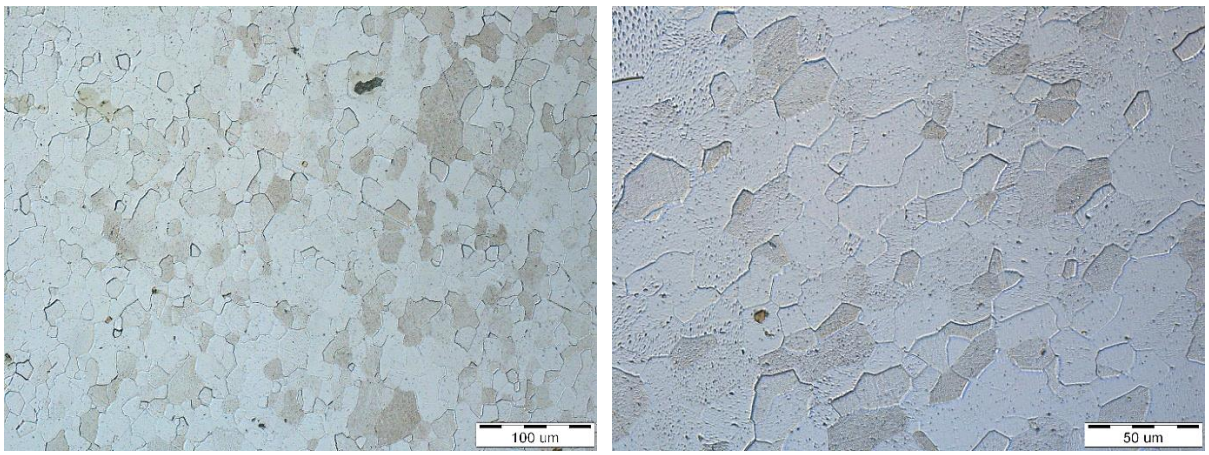

(a) (b)

Figure 6.4 Optical microscope micrographs of IF steel at different magnification: (a) 250; (b) 500.

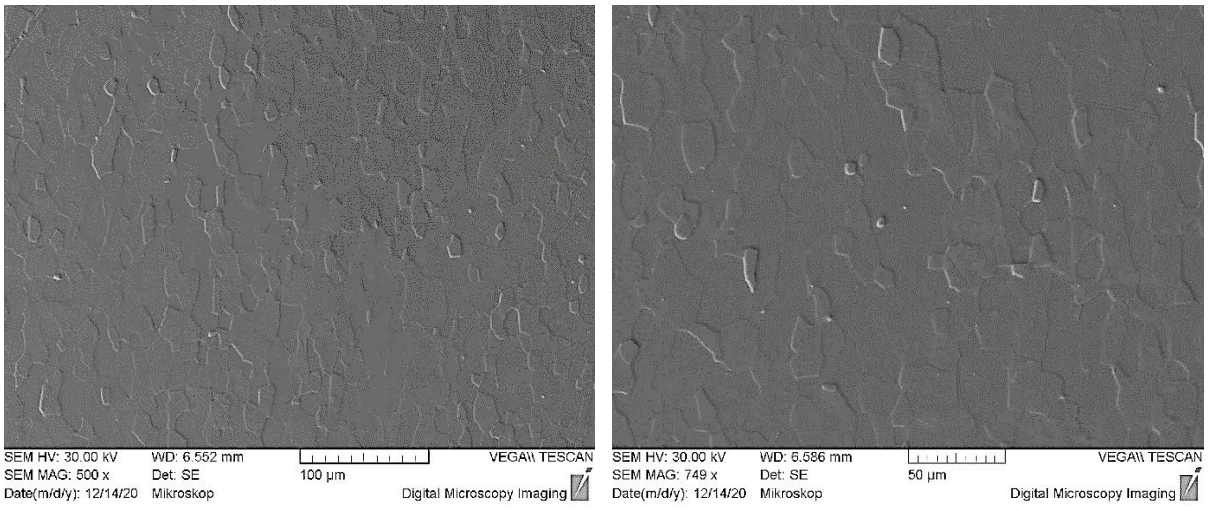

(a) (b)

Figure 6.5 SEM microstructure of IF steel at different magnification: (a) 500; (b) 750.

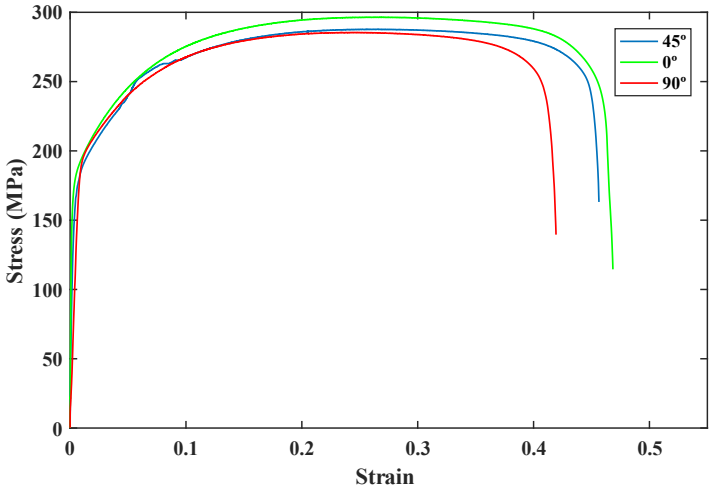

Figure 6.6 Engineering stress versus strain curves for IF steel.

Table 6.3 Chemical composition by weight % of the IF steel used in this work.

Sample	C	Mn	Si	P	S	Cr	Ni	Cu	Al	Ti	Fe
IF steel	0.0018	0.110	0.024	0.0062	0.0076	0.033	0.036	0.026	0.051	0.056	99.58

Table 6.4 Mechanical properties of tested IF steel from a standard tensile test.

Angle to RD	σ_y(MPa)	σ_u(MPa)	A_g%	A_{50}%	n	r_p
0°	168	290	26.76	46.85	0.24	1.44
	157	286	26.19	47.24	0.24	1.44
45°	165	281	25.24	47.65	0.20	1.43
	160	282	26.28	45.68	0.21	1.34
90°	187	285	24.38	41.94	0.21	1.74
	166	281	24.87	44.37	0.23	1.93

6.2 Design of experiments

The fundamental aim of this research work is to find out fracture toughness of the DP450 and the IF steels in plane-stress dominant (thin sheet) conditions, validation of EWF method, determination of microstructural influence on the fracture toughness, local strain distribution during the EWF test, and comparing the EWF results with standard tests.

DENT specimens are used in this work, and the test is carried out on a universal tensile testing machine. Material properties are determined using a standard tensile test. The steels' (DP450 and IF) chemical composition is determined using a spark atomic emission spectrometer. Fracture toughness of the material in mode-I is determined using EWF methodology. Determination of the fracture toughness in mode-II and mixed-mode is also tried using the EWF methodology. Microstructure characterization is made using Electron Back Scattered Diffraction (EBSD) technique. Local strain analysis is done using a digital image correlation (DIC) technique. Fractured surface analysis is done using a Scanning Electron Microscope (SEM).

6.2.1 Tensile test

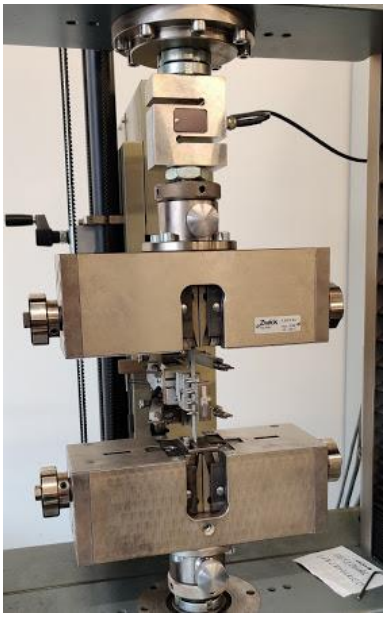

Figure 6.7 Zwick Z030/TH2A tensile testing machine used for the tensile test and EWF test.

The standard tensile test of material helps determine tensile strength, ductility, strain hardening, plastic anisotropy, and yield strength in ideal conditions. Properties of the material in real-world condition may be different and depends on various factors like environment, temperature, and many other factors. However, the tensile test results help compare different materials, material selection, design, and development of new materials. The ASTM

E8/E8M[67] is used as a standard reference in our work to conduct the tensile test. The experiments are conducted at a specified room temperature of 10-38 ºC. Since rolled sheets are used in this work, tensile strength is determined in three directions, which are, rolling direction, 90º to the rolling, and 45º to the rolling directions. Two samples are prepared in each direction for better results. The experiments are conducted in ZWICK/Roell Z030/TH2A tensile testing machine (Figure 6.7). Force on the specimen during the test is measured using an in-built load transducer. Displacement of the specimen in longitudinal (elongation) and lateral directions (reduction in width) are recorded using in-built extensometers at 50 Hertz. Figure 6.8 shows the standard dimensions of the tensile test specimen used in this work. ASTM E8/E8M flat plate standard specimen having 12.5 mm width is selected. According to the standard, 40 mm wide samples can only be used for materials having more than 5 mm thickness, and a sub-size specimen of 6 mm width is too small to fit the extensometer. The standard strain rate $\dot{\varepsilon}$ across all tensile tests is 0.002^{-1}s. The samples are prepared using a CNC milling machine without any burrs, notches, or groves, and with smooth finishing. Parameters like yield strength, ultimate strength, elongation at fracture, elongation at maximum load, strain hardening co-efficient n, and plastic anisotropy coefficient r_p are determined.

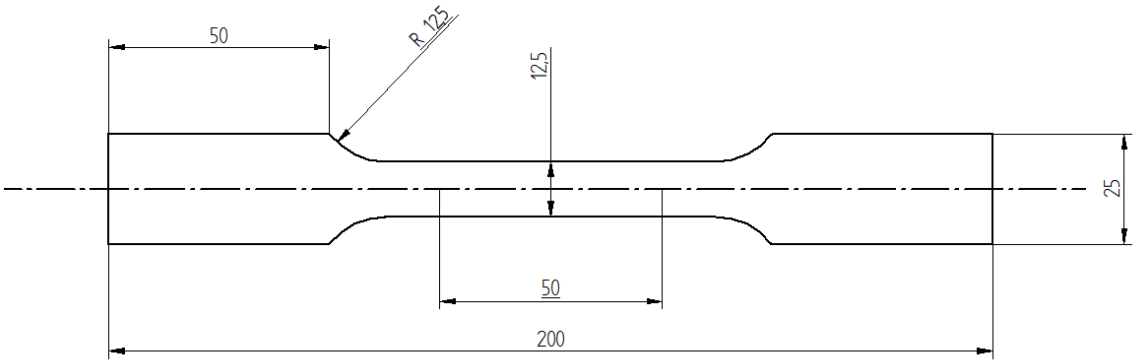

Figure 6.8 Standard tensile test sample with dimensions (mm).

6.2.2 EWF test

Essential work of fracture (EWF) methodology has been used to find out the fracture toughness of the DP450 and IF steel sheets. Section 4.2 explains the theory and methodology behind the EWF methodology. Double edge notched tension (DENT) specimens prepared from laser cutting, and EDM technology are used for the EWF test. Details of the sample preparation are explained in section 6.3. Figure 6.9 shows the DENT specimen with magnified notch-tip dimensions prepared from the laser and EDM cutting. In the EWF test, the sample is loaded in a universal tensile testing machine and pulled uniformly until the final fracture. Gauge length

is difficult to identify in DENT specimens; hence, the crosshead speed is considered a reference rather than strain rate. A uniform crosshead speed of 1 mm/minute is used in all the EWF tests. The area under the load-displacement curve is the output of the test. The force and displacement are recorded by the inbuilt load transducer and extensometer, respectively. The stress across the ligament in the EWF test is tensile; hence, no anti-buckling supports are needed. Grips on either end of the DENT specimen is free of speckle pattern for better gripping. A gripping length of approximately 25 mm is used in all the samples. For notched samples, original ligament length is considered for specific essential work of fracture w_e calculation. For fatigue precracked samples, the actual ligament length is used, i.e., fatigue precrack is subtracted from the original ligament length. The fatigue crack is measured in a scanning electron microscope after the EWF test. The validity and applicability of EWF methodology in mode-II and mixed-mode are examined using double-edge notched shear and staggered specimens, respectively. The concept of mixed-mode and mode-II loading in EWF methodology is discussed in section 4.3.6. Figure 6.10 shows the geometry of double edge notched shear specimen with dimensions. Double edge notched shear specimen produces in-plane shear strains when loaded in tension. The ASTM standard B831-19[47] *Standard Test Method for Shear Testing of Thin Aluminium Alloy Products* is used as a reference to design the double edge notched shear specimens. Figure 6.11 shows the geometry of the staggered double-edge notched tension specimen with dimensions. Cotterell et al.[44] designed the specimens for the mixed-mode loading, and the angle between the notches is selected as 30º in this work.

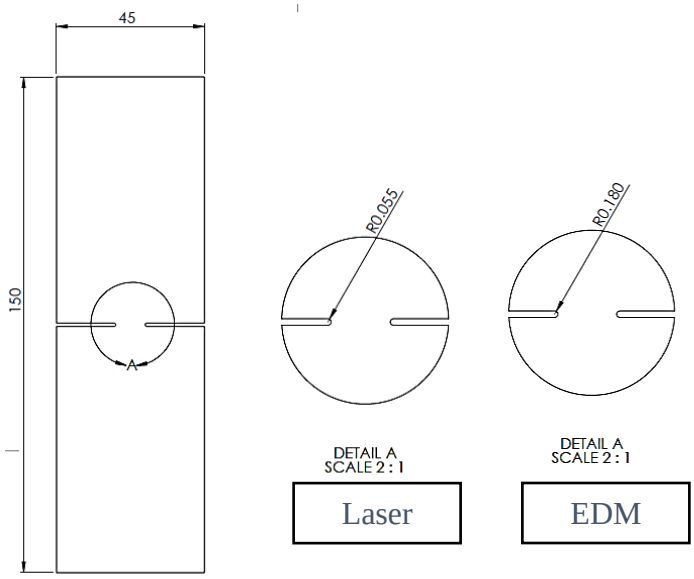

Figure 6.9 Double-edge notched tension (DENT) specimen prepared from laser and EDM technology (mm).

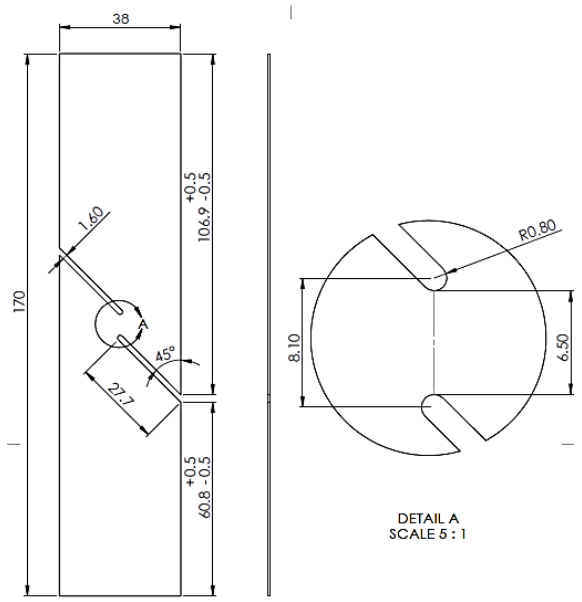

Figure 6.10 Double-edge notched shear specimen with dimensions (mm).

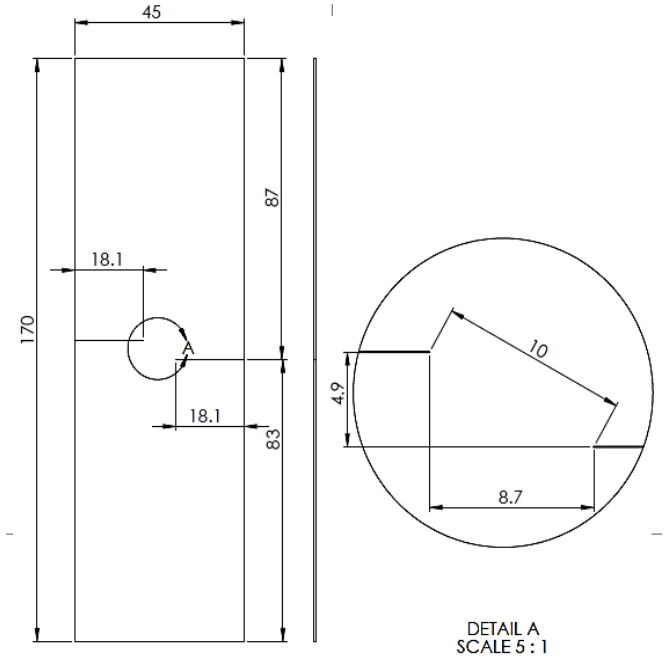

Figure 6.11 Staggered double-edge notched tension specimen (30º) with dimensions (mm).

6.3 Sample preparation

The DP450 and IF steel sheets of dimensions roughly 500*300 and 300*210 mm are collected before the stamping. The average thickness of the DP450 and IF steels are 0.565 and 0.685 mm, respectively. There are no international standards published on the dimensions of the EWF test sample. E. Q. Clutton[26&27] conducted several round-robin experiments on the essential work of fracture methodology. European structural integrity (ESIS) has published some guidelines for sample preparation. Based on various research articles and the ESIS

guidelines, a width of 45 mm and a height of 150 mm are chosen. According to B. Cotterell and J. K. Reddel[20], the ligament's lowest length should be more than three to five times the thickness. A more conservative approach is applied to the lowest length, and 5 mm is chosen. The ligament's highest length is limited to 13 mm; nine different samples with ligament lengths ranging from 5 to 13 mm are selected. A schematic representation of the sample is shown in Figure 6.12. For the essential work of fracture methodology, the sample's notch-tip radius should be as minimum as possible. A lower notch radius helps in creating fatigue cracks quickly; by increasing the stress concentration. Two different technologies are used to cut the sheet and create the notch, which are, high intensity laser and electrical discharge machining (EDM).

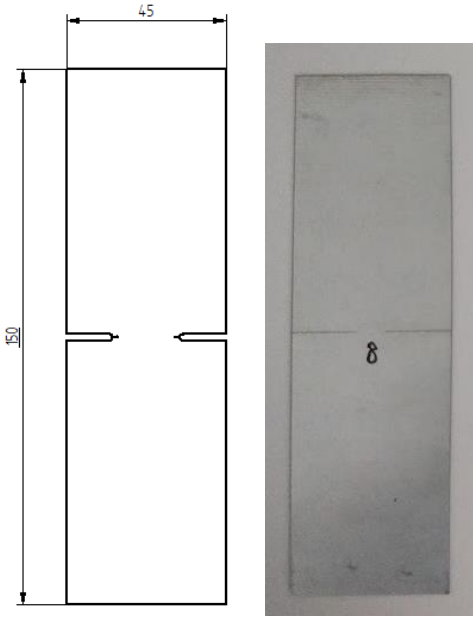

Figure 6.12 Schematic diagram and actual picture of specimen for EWF test (mm).

6.3.1 Laser cutting

A high-intensity pulsed laser beam generated by electrical discharge or lamp source is reflected inside a laser source until it gets high energy. The high-intensity monochromatic coherent light is directed using optics on the smallest possible surface area to be cut. The source of laser can be CO_2 excimer gas laser or solid-state laser. The laser head is attached to a computer numerically controlled (CNC) machine or G-code for better precision. The power of the laser beam is varied based on the sheet thickness. The laser's intensity depends on the laser source, the focal length of lenses, the laser beam mode (variation across the laser cross-section), the laser beam's wavelength, and the focal position of the laser head. Pressurized gas

is used to blow away the melted material. Oxygen, nitrogen, and other inert gases are used as cutting gases. Gases such as nitrogen and argon don't produce any combustion. In contrast, the oxygen makes an exothermic reaction and produces high temperatures near the base material. Figure 6.13 shows a simple schematic representation of laser cutting. The thickness of the material is less than a millimetre; hence, the cutting speed can be relatively fast. Because of the high-intensity laser and lower sheet thickness, the notches are cut in a single go. Figure 6.14 shows the sample prepared from laser cutting technology along with notch tip dimensions. Notch tip radius is a crucial parameter for the essential work of fracture testing, as it influences stress concentration, and thereby cracks propagation. The lowest possible laser beam width is created for the lowest possible notch-tip radius. A notch tip radius of 55 µm is achieved.

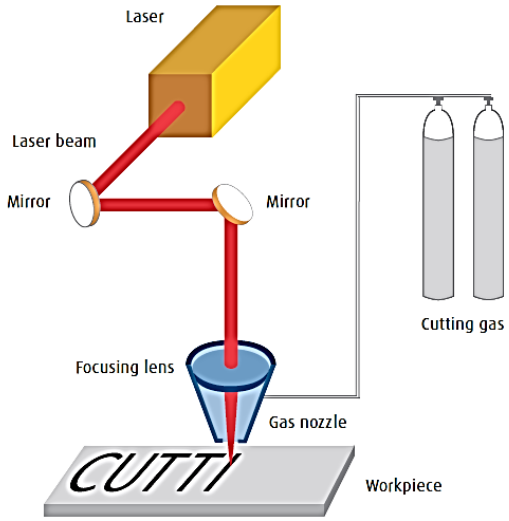

Figure 6.13 Schematic representation of laser cutting[68].

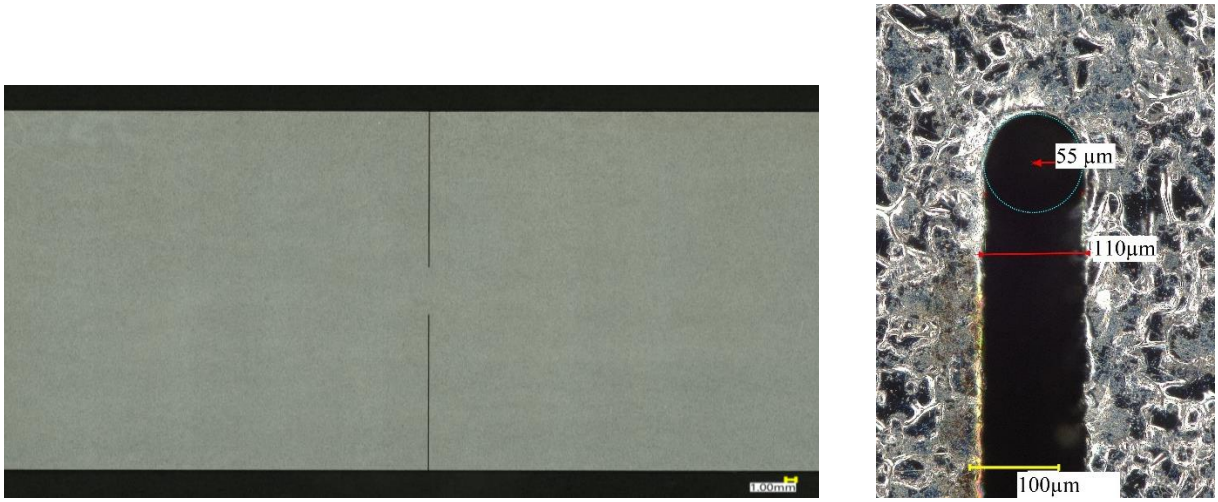

(a) (b)

Figure 6.14 (a) EWF testing sample prepared using laser cutting; (b) Notch tip dimensions from laser cutting.

The laser cutting's primary objective might be a sharp notch tip; however, the effect of heat generated during the laser cutting operation also needs to be considered. Though the heat-affected zone is relatively smaller than a standard welding or flame cutting, it is necessary to estimate the change in properties due to the laser cutting.

6.3.2 Electrical discharge machining (wire EDM)

In electrical discharge machining, the material is removed by creating an electric discharge between two electrodes in a dielectric medium: the workpiece and the tool act as electrodes. In this work, wire EDM technology is used to prepare the sample. In the wire EDM, a constantly moving wire acts as one electrode and the tool, and the workpiece to be cut as another electrode. Generally, de-ionized water is used as a dielectric medium, and it also serves to flush. Dielectric medium cools down the workpiece and the tool and flushes out the debris from the machining process. Due to the dielectric breakdown of water, an electric discharge is created between the wire and workpiece, which helps in removing the material. There isn't any contact between the workpiece, and the tool (wire), the spark generated between them melts the workpiece. Figure 6.15 shows a schematic representation of metal removal using wire-EDM. The constant changing wire during operation helps in the longevity of the tool (wire). An electric power supply (DC) is given for the tool to create an electric potential difference between the tool and the workpiece. A CNC-plotter helps in achieving better accuracy and creating complex shapes. Hard metals can also be cut using EDM, which is difficult in conventional mechanical processes. The absence of physical contact and fast cooling by di-electric medium helps achieve the low residual stress in the material. The change in material properties on the workpiece due to EDM is significantly lower than laser cutting. A smaller heat-affected zone and low residual stresses are expected in the notch tip[69–71]. A notch tip radius is 150 to 180 µm is achieved in this work. Figure 6.16 shows the sample prepared using the wire EDM process. Figure 6.17 shows the notch tip dimensions of the sample created by the wire EDM process. The notch tip radius is significantly larger than the laser cutting sample.

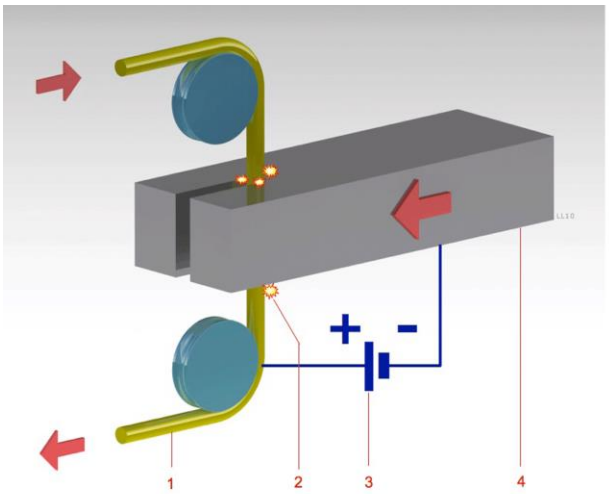

1 Wire (tool). **2** Electrical discharge (Electric arc). **3** Power supply. **4** Workpiece

Figure 6.15 Schematic representation of a wire-EDM process.

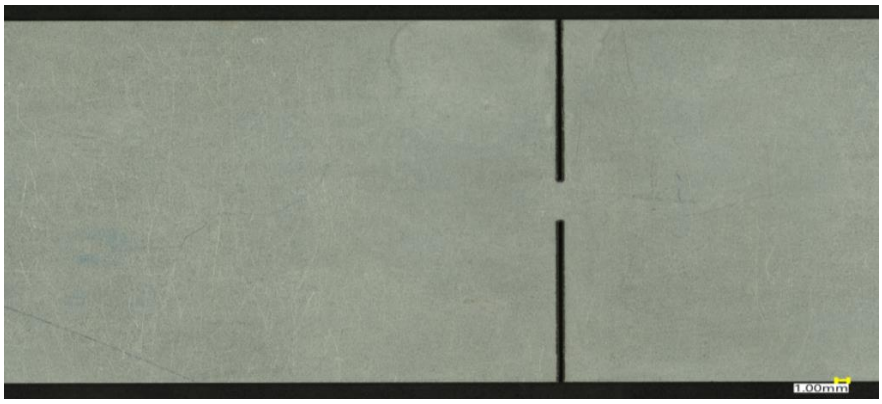

Figure 6.16 EWF testing sample created by wire EDM.

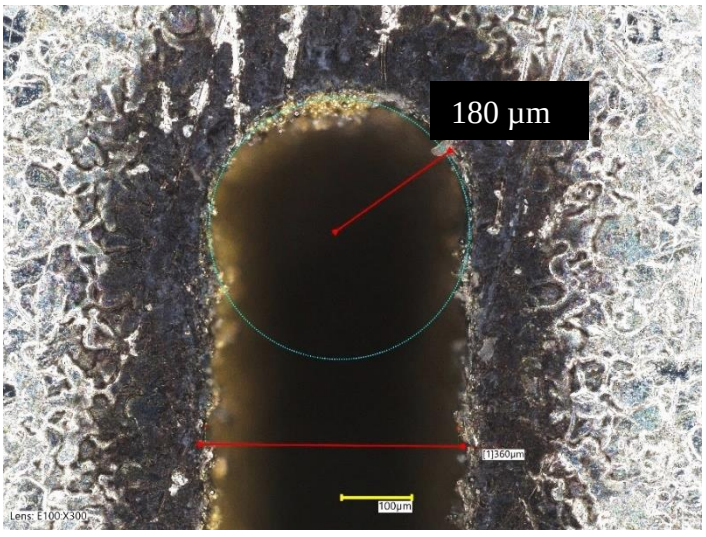

Figure 6.17 Notch tip dimensions of the sample prepared using wire EDM.

6.3.3 Fatigue precrack

The fundamental objective of a fracture toughness test is to find out the resistance of a material against crack growth. Any sharp notch produced by machining will not simulate an actual crack[11]. Fatigue crack generated from cycling loading is used in most of the research works. The count of cycles needed to initiate a crack is hard to predict and depends on factors like material properties, load, notch radius, and quality of notch. In this work, two different notch starters are present, one set of samples prepared from the laser cutting has a sharp starter notch of 55 µm radius, and the other has 150~180 µm prepared from the EDM. The primary requirement of fatigue crack for a DENT specimen is that the crack length on either side should be the same, and the crack should propagate straight forward on either side. Fatigue crack initiation can be controlled either by force or displacement. According to the ASTM E1820 standard, the maximum stress intensity K_{1max} during fatigue precrack should not exceed 70% of critical stress intensity factor K_{1C}. The ratio of minimum to maximum force R during the fatigue precrack is suggested as 0.1 for faster initiation of crack. The crack length should be more than 0.2 mm on either side (in this work). It is challenging to keep the length of fatigue cracks constant in all specimens. At least, to keep the same fatigue precrack on either notch of the DENT specimen, the sample is rotated after a few thousands of cycles regularly. Crack on either side of the ligament must be equal for simultaneous crack initiation and growth. For both the laser cutting and the wire samples, high cycle fatigue cracks are generated. The maximum load during fatigue crack generation is less than the yield strength of the material.(Fatigue precrack was prepared with the help of *COMTES FHT* a.s., Dobřany, Czech Republic)

6.4 Digital image correlation technology

Generally, strain and displacement obtained during the essential work of fracture (EWF) testing from an extensometer or a crosshead have only global data. Information obtained from the extensometer and crosshead is the sample's average deformation without considering local deformation. Digital image correlation (DIC) is a non-contact optical measurement technique, which utilizes a series of images and computation to give exact deformation at every location on a sample[72]. One or two cameras are used to capture images at several intervals during the test. One or two polarised LED lights are used for better illumination of the pattern. A commercial software having robust algorithm and post-processing helps in full-field measurement of deformation on the surface. To create the information on the sample, to

digitally analyse the images, a pattern is created. The pattern can be grids, dots, lines, random arrows, and speckle patterns. A characteristic of a good pattern is to have a high amount of information (pixel), no preferred orientation, and a non-repetitive (non-periodic) pattern for easy analysis[67.68]. ARAMIS commercial DIC (Figure 6.18) is used in this research work. The sample is first sprayed entirely with a white synthetic spray, and later a black spray is used to create a distinct stochastic pattern. Figure 6.19 shows the stochastic pattern on the sample.

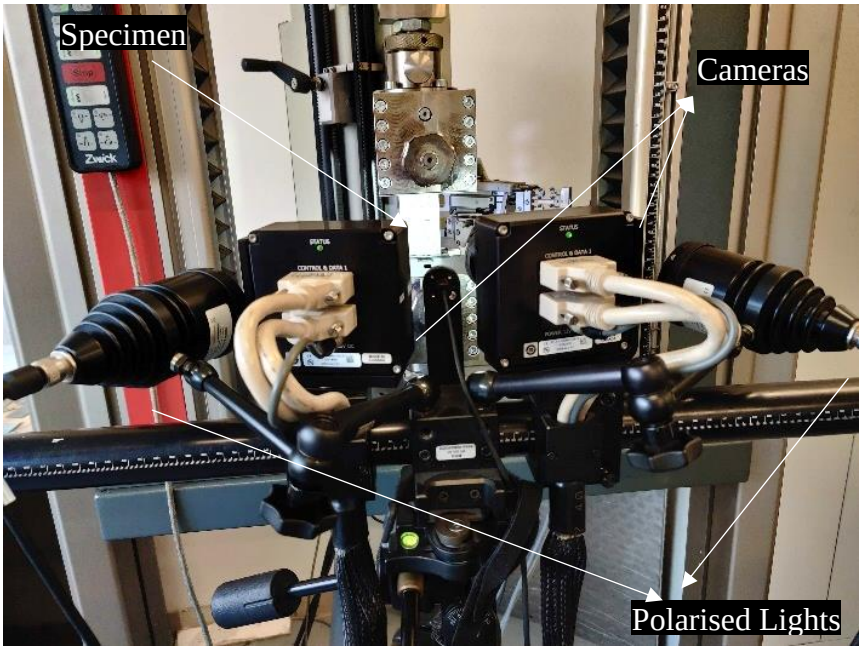

Figure 6.18 Aramis 3D digital image correlation (DIC) experimental setup.

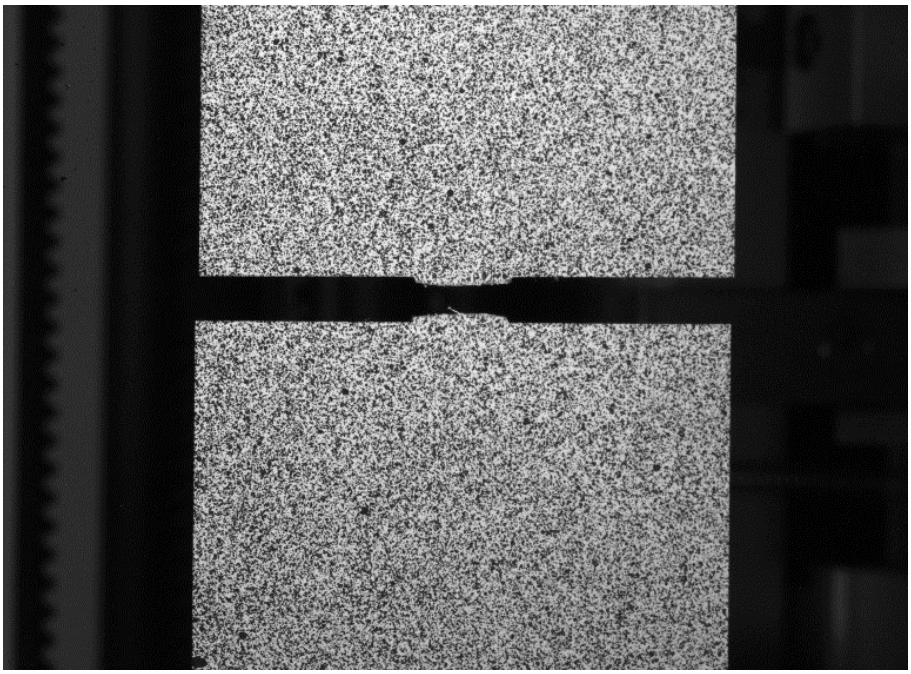

Figure 6.19 Stochastic patterns of DIC sample.

6.5 Electron backscatter diffraction

Electron backscatter diffraction (EBSD) is an additional material characterisation technique associated with SEM. It helps in analysing grain size (up to 20 nanometres), crystallographic orientation, internal grain deformation, phase identification, crystal imperfection (misorientation), and strain at the grain level[75]. Ease of sample preparation, advancement in cameras, faster processing speed, and enhanced visualisation of results made EBSD a reliable technique in the research field and industry. The distinctive diffraction pattern of Kikuchi bands was first observed in 1928[76]. EBSD is attached to a scanning electron microscope, and a high-intensity electron beam is made to fall on a finely polished surface at a tilted angle (70º). The backscattered electron with a minimum loss of energy will fall on a phosphorus screen. The backscattered electrons carry information about the crystallographic orientation of atoms, thereby generating the Kikuchi bands on screen. These unique Kikuchi bands will be compared with a database to find out the crystal and its orientation. The phosphorus screen is kept at about 20 mm from the sample and parallel to the incident electron beam. The phosphorus screen is connected to a CCD (charge-coupled device) camera to record the Kikuchi bands at the scanning location. The sample's scanning can be done by mechanical movement of the sample or digital beam scanning mode. The sample's grain size can be precisely determined, and crystallographic orientation within each grain can also be determined. Inverse pole figure (IPF) map, grain size map, misorientation (MO) maps, kernel average misorientation (KAM) map, and many more maps are generated after EBSD scanning[77–79]. Figure 6. 20 shows the simple schematic representation of the EBSD operation.

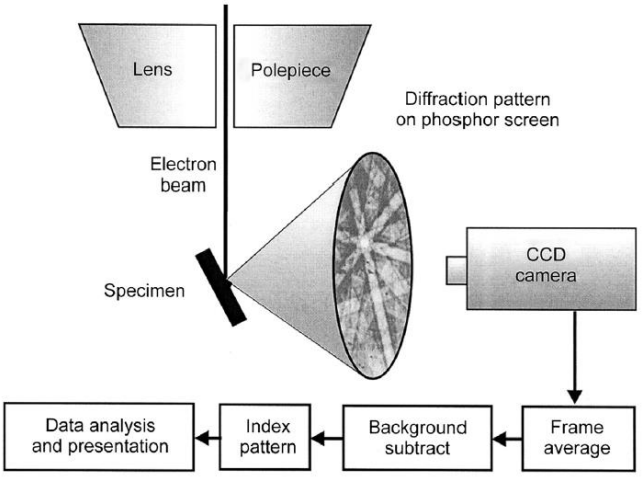

Figure 6. 20 Schematic representation of EBSD in SEM[80].

The DP450 and the IF steel samples are prepared for the EBSD analysis before and after the EWF tests. The steel sheets are cut into small rectangular shapes of 15*10 mm. These small samples are mounted onto Bakelite resin capsules using a high-pressure mounting machine. Then the samples are grinded using silicon papers ranging from 60 to 1500. The grinded samples are then polished using a diamond paste of 3 and 1 µm. The Bakelite resin is broken to remove the sample. The grinded and polished samples are cleaned using an ultrasonic cleaner for 10 minutes. The mechanically polished samples are electro-polished using struers electro-polishing machine. The technical specification for the electro-polishing is given in Table 6. 5. A specially designed holder is used to place the specimen inside the SEM. The specimen is tilted about 70º to the horizontal surface. A probe current of 20 Nano ampere, step size of 0.27 µm/pixel, 60.2 fps (frames per second), and 20 kV accelerating voltage is used.

Table 6. 5 Electro-polishing parameters for EBSD analysis.

	Area (cm^2)	Flow rate	Voltage (V)	Time (s)
DP450	1	10	23	5
IF Steel	1	10	36	7

6.6 Hole expansion test and Nakajima test

Figure 6. 21(a) shows a simple schematic representation of a **hole expansion test**. The essential components of the test are holders to hold a sample, cylindrical punch, and sample. An initial bore diameter (d_o) of the sample is selected as 35 mm. The cylindrical punch is moved into the bore until a fracture appears. The final diameter of the bore (d_f) is measured after the test. Several samples with different shearing clearance are prepared and tested (Figure 6. 21(b)). The hole expansion ratio λ is calculated using equation 6.1. (Hole expansion test, the Nakajima test, and FLD test for the DP450 and the IF steel is done in the *Technical University of Liberec* in association with *Skoda auto*).

(a) (b)

Figure 6. 21 (a) Schematic representation of hole expansion test[81]; (b) samples after the test.

$$\lambda = \frac{d_f - d_o}{d_o} \times 100 \tag{6.1}$$

Figure 6. 22 shows a schematic representation of a **Nakajima test** and sample used to create FLD. Eleven samples having a width from 40 to 120 mm are used for the test. The difference in the samples' width is used to create various strain conditions, from uniaxial tension to equi-biaxial tension. The samples are sprayed with a black and white speckle pattern, and Aramis DIC collects the strain information. The sample is gripped inside the holder, and the punch is pressed until complete fracture. The samples with centre cracks are considered for FLC calculation.

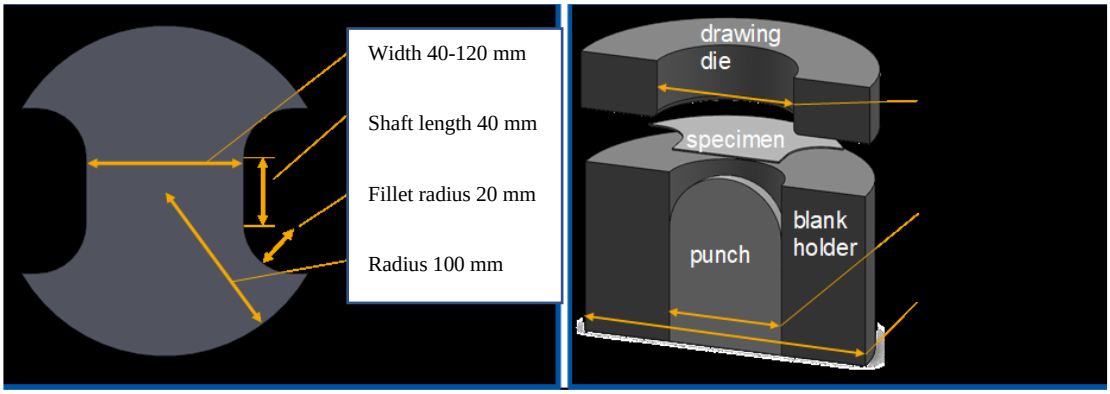

(a) (b)

Figure 6. 22 (a) Samples of Nakajima test; (b) schematic representation of Nakajima test[82].

7. RESULTS AND DISCUSSIONS OF EWF TESTS

7.1 Optimization of test specimen design

Geometry and technology used in sample preparation will have a considerable effect on test results. The methods used for the sample preparation are briefly discussed in sections 6.3.1 and 6.3.2. Figure 7.1 shows the optical microscope images of the microstructure near the notch tip of the DP450 steel. A high temperature generated by the laser during the sample preparation is affecting the microstructure. The laser is exceptionally local and precise; the size of the heat-affected zone (HAZ) is not as significant as regular welding HAZ. The grain refinement has spread a few micrometres near the cutting edge (Figure 7.1(a)). There is no grain refinement in the EDM cut (Figure 7.1(b)) because of dielectric fluid in the wire electrical discharge machining.

It is hard to quantitatively estimate the change in mechanical properties in the heat-affected zone of such a small area. Microhardness measurement is used to analyse the effect of the laser and the EDM wire cutting on the heat-affected zone. It is not a precise way to estimate the change in properties; however, it is convenient and available. For better sensitivity, HV 0.2 loading is used for the hardness measurement. Figure 7.2 shows the micro-hardness graph versus the distance from the edge for the laser and the wire EDM cut for the IF steel. The IF steel is deliberately selected against the DP450 steel because of its more homogeneous microstructure.

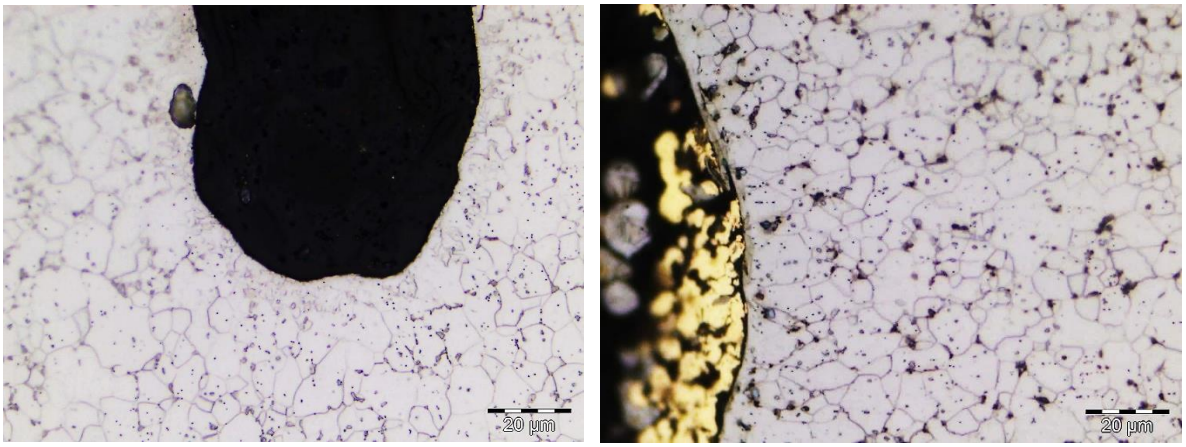

(a) (b)

Figure 7.1 Optical microscope images of microstructure at the notch tip of DP450 steel: (a) laser cutting; (b) EDM cutting.

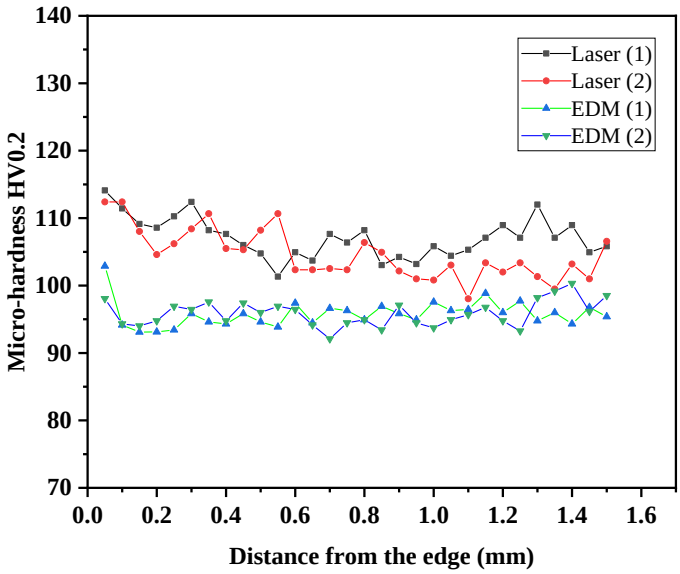

Figure 7.2 Microhardness versus distance from the edge for laser and wire EDM of IF steel.

A sharp increase of hardness can be seen near the edge and decreases as moved away from the edge. In general, the laser cut has produced higher hardness against the EDM cut. In the EDM cut, the hardness drops suddenly after one or two measurements, and the remaining values are uniform. In the case of laser-cut, the drop in hardness is more linear. From analyses of the hardness results, the EDM cut has little effect on the sample and produces smaller HAZ. The notch tip radius created by the laser cutting is 55µm and 180µm for the wire EDM. The notch tip radius created by the wire EDM is dependent on the wire diameter used. Despite the higher notch tip radius from the wire EDM process, the effect on material properties is more negligible. Though the difference in hardness is very little between the two methods, EDM is a safer and better sample preparation method. However, the presence of fatigue precrack in the sample offset the limitations of the laser.

7.2 Essential Work of Fracture test results for DP450

Several sets of samples are prepared using laser and EDM for the EWF test. Initially, notched and precracked (fatigue precracked) samples prepared from the laser are tested, and the deformation output is recorded using crosshead displacement. In the second stage, notched samples prepared from the laser and the EDM are tested, and the deformation output is recorded using an extensometer. Finally, fatigue precracked samples are tested, and the deformation is recorded using the extensometer. Section 6.2.2 describes the details of the EWF experiment and the experimental parameters. The width and the heigh of the specimen are 45 mm and 150 mm, respectively. Each sample set has nine specimens and has a ligament length from 5 to 13 mm. The length of the ligament is measured before the EWF test using a stereomicroscope. A standard crosshead speed of 1 mm/minute is used across all the EWF tests. The physical extensometer is kept at 50 mm apart, and it is well outside the plastic deformation zone. The force and the displacement are recorded until the force falls to 75% of the maximum force. The area under the force-displacement curve denotes the total work of fracture W_f. Two different methods can calculate the area under the force-displacement curve. The first method is the direct calculation of curve area by trapezoid equations, and the second method is integrating the best-fit curve. Both the methods give identical results, and the first method is used in this work.

7.2.1 Notched samples

This section is dedicated to notched samples. The notched samples prepared from the laser and the EDM are tested. The notched samples are tested in three different stages. Initially, the notched samples prepared from the laser cutting are tested, and deformation output is recorded using crosshead displacements. In the second stage, the notched samples prepared from the laser are tested, and the deformation output is recorded using an extensometer. Finally, the notched samples prepared from EDM are tested, and the deformation output is recorded using the extensometer.

Laser notched samples with crosshead displacements

Figure 7.3 shows the force-deformation (displacement) curves for the notched samples prepared from the laser, and deformation is recorded using the crosshead movement. The area under the curve increases with an increase in ligament length without changing the curve's shape. Specific work of fracture w_f is calculated by dividing the total work of fracture W_f by the initial ligament area. The maximum recorded deformation is considered as displacement at fracture v_f.

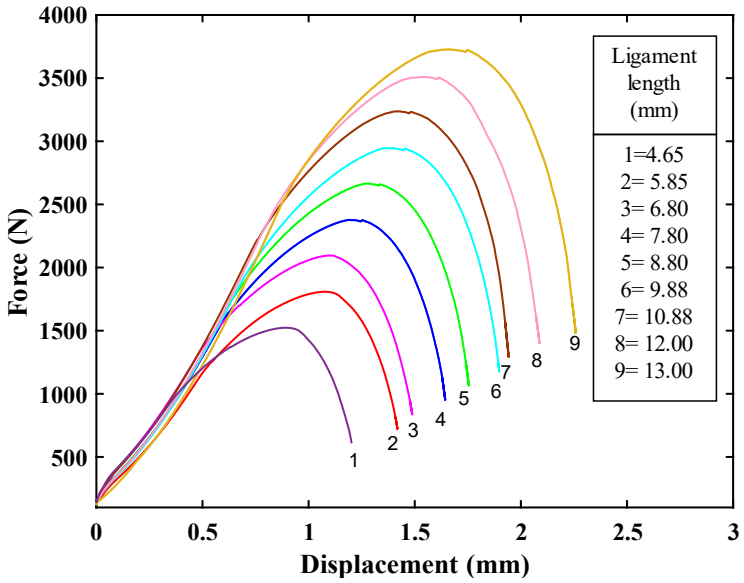

Figure 7.3 Force versus displacement (crosshead) diagram for notched samples prepared from the laser.

Table 7.1 shows the outputs and calculated parameters from the force-displacement curves of the EWF tests for the notched samples prepared from the laser (crosshead). Figure 7.5 shows the specific work of fracture wf versus original ligament length for notched samples prepared from the laser (crosshead). A linear curve is generated based on the data points to determine the specific essential work of fracture w_e and it is the zero intercept on the y-axis. In this case, the specific essential work of fracture is 352.88±8.64 kJ/m^2, and βw_p is 30.36±0.93 kJ/m^3. βw_p is the slope of the linear fitted line, and it equates to specific non-essential work of fracture(w_p). β is the shape factor of plastic deformation and is given by $^{\pi a}/_{4b}$; a and b are major and minor axis of the ellipse. Pearson correlation coefficient R^2 is an indicator for a linear relationship between abscissa and ordinate values, one being perfectly linear. The R^2 value is equal to 0.9934 (Figure 7.5), which indicates a good linear fit. The good linearity proves that the specific work of fracture increases linearly with the ligament length within the specified ligament range. Figure 7.4 shows the graph of deformation at fracture versus ligament length for notched samples prepared from the laser, and deformation is recorded from the crosshead. A linear curve is generated based on the data points to find crack tip opening displacement (CTOD) δ_c^e and crack tip opening angle (CTOA) ψ^e. The zero-ligament length intercept of the fitted line on the y-axis is the crack tip opening displacement (CTOD) δ_c^e and slope of the linear fitted line is half of the crack tip opening angle (CTOA) ψ^e. The determined CTOD δ_c^e and CTOA ψ^e from the EWF tests are 0.6890±0.038 mm and 13.65º respectively. The fitted line has an R^2 value of 0.9913.

Table 7.1 EWF tests outputs (crosshead displacements) for notched samples prepared from the laser.

Ligament length (mm)	Maximum force (N)	Maximum stress(MPa)	Total work of fracture W_f(N-mm)	w_f (kJ/m^2)	v_f (mm)
4.65	1523.99	580.070	1296.03	493.30	1.202
5.85	1809.45	547.447	1726.93	522.48	1.418
6.8	2095.94	545.534	2139.33	556.83	1.488
7.8	2377.6	539.505	2625.42	595.74	1.643
8.8	2665.15	536.032	3116.88	626.89	1.754
9.88	2946.44	527.828	3708.64	664.37	1.898
10.88	3238.13	526.765	4180.76	680.11	1.942
12	3510.9	517.832	4795.97	707.37	2.087
13	3727.63	507.506	5490.62	747.53	2.258

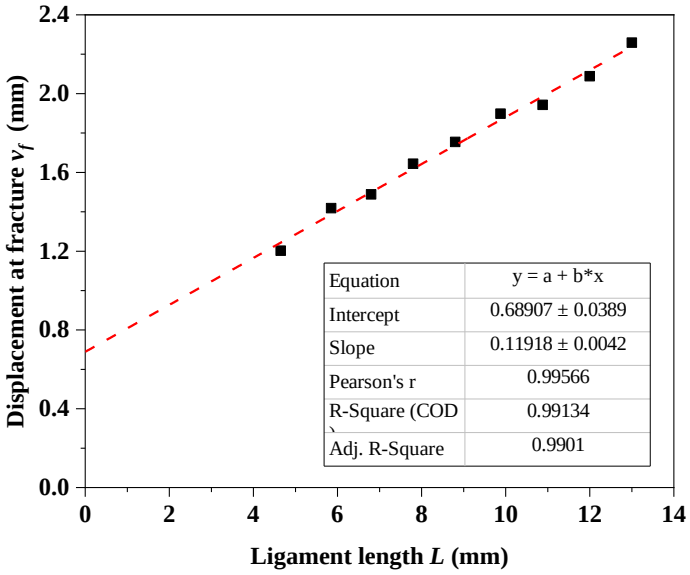

Figure 7.4 Deformation at fracture versus ligament length for notched samples prepared from the laser(crosshead).

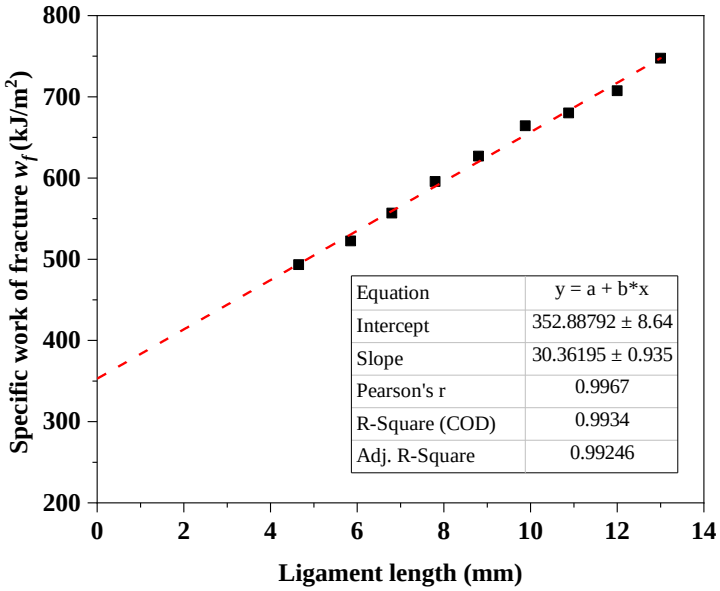

Figure 7.5 Specific work of fracture versus ligament length for notched samples prepared from the laser(crosshead).

Laser notched samples with extensometer displacements

Figure 7.6 shows the force-deformation (displacement) curves for the notched samples prepared from the laser, and deformation is recorded using an extensometer. The deformation recorded from the crosshead is much higher (Figure 7.3) in comparison to the extensometer (Figure 7.6); hence, the area under the force-displacement curve will also be larger. The higher displacement from the crosshead is attributed to high elastic energy storage in grips[83] and probable slip due to metal coating and surface paints (DIC analysis). From the visual observation and DIC images, crack initiation happens near the peak load for the notched samples. After the crack initiation, the decrease in load is not instantaneous; instead, it is more gradual. The gradual decrease in load indicates good crack growth resistance and ductile fracture during the crack growth.

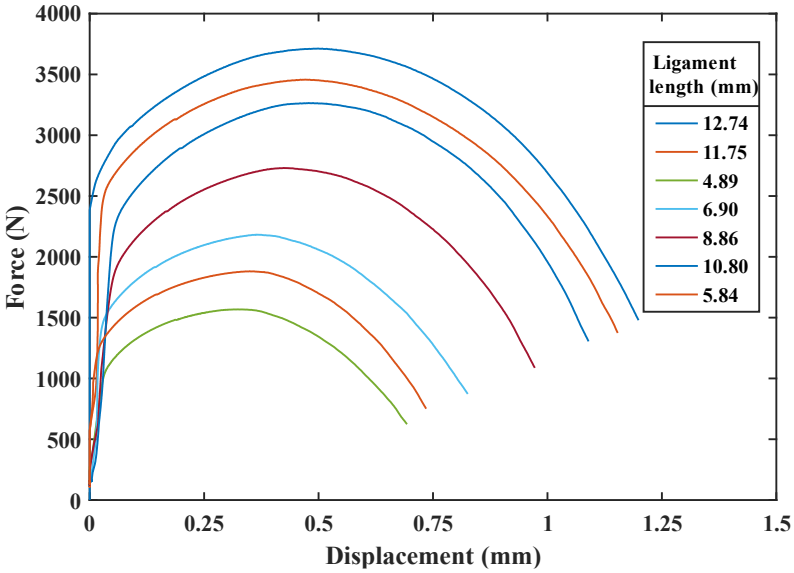

Figure 7.6 Force versus displacement (extensometer) diagram for notched samples prepared from the laser.

Table 7.2 shows the outputs and calculated parameters from the force-displacement curves of the EWF tests for the notched samples prepared from the laser (extensometer). Figure 7.8 shows specific work of fracture versus ligament length for the notched samples prepared from the laser (extensometer). The specific essential work of fracture *'w_e'* and slope of the fitted curve are 200.14±4.84 kJ/m^2 and 26.16±0.523 kJ/m^{3}respectively. An R^2 value of 0.9980 (Figure 7.8) indicates the fitted curve's good linearity. Figure 7.7 shows the graph of deformation at fracture versus ligament length for notched samples prepared from the laser (extensometer). The determined CTOD δ_c^e and CTOA ψ^e from the EWF tests are 0.3625±0.0016 mm and 7.66º respectively. The fitted line has an R^2 value of 0.9962.

Table 7.2 EWF test outputs (extensometer displacements) for notched samples prepared from the laser.

Ligament length (mm)	Maximum force (N)	Maximum stress(MPa)	Total work of fracture W_f(N-mm)	w_f (kJ/m^2)	v_f (mm)
4.89	1567.96	567.52	897.61	324.89	0.6933
5.84	1881.69	570.28	1161.41	351.99	0.7350
6.9	2182.24	559.76	1486.70	381.35	0.8258
8.86	2731.15	545.59	2194.78	438.44	0.9723
10.8	3264.99	535.07	2955.26	484.31	1.0896
11.75	3457.26	520.77	3370.35	507.68	1.1535
12.74	3713.00	515.83	3807.55	528.97	1.1988

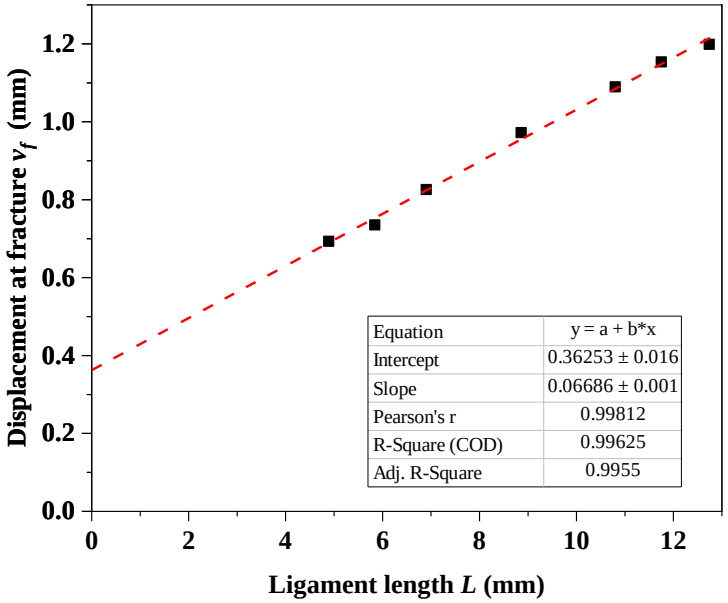

Figure 7.7 Deformation at fracture versus ligament length for notched samples prepared from the laser (extensometer).

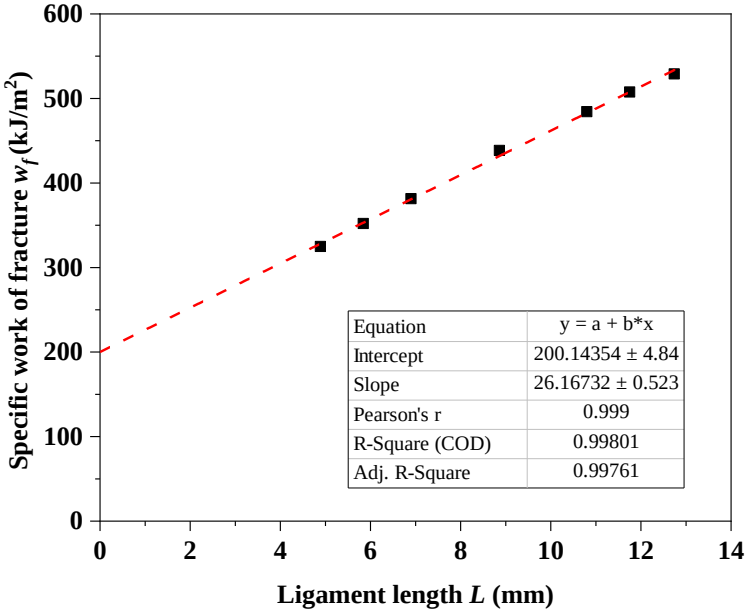

Figure 7.8 Specific work of fracture versus ligament length for notched samples prepared from the laser (extensometer).

EDM notched samples with extensometer displacements

Figure 7.9 shows the force-displacement curve for the notched samples prepared from the EDM (extensometer). In all the figures (Figure 7.3, Figure 7.6 & Figure 7.9), the curves' shape is similar for all the ligament lengths in their respective group. Like the standard stress-strain diagram (Figure 6.3), in the beginning, a linear portion is observed before plastic deformation (Figure 7.6 & Figure 7.9), and the curve is almost parabolic after deviating from the linear portion until fracture. The force will gradually increase and decrease identically before and after reaching the peak load. In the notched samples prepared from the EDM (Figure 7.9), there is a sudden dip in force after reaching the maximum load. This load drop is attributed to the beginning of the constant crack growth, but it is more visible in the EDM samples.

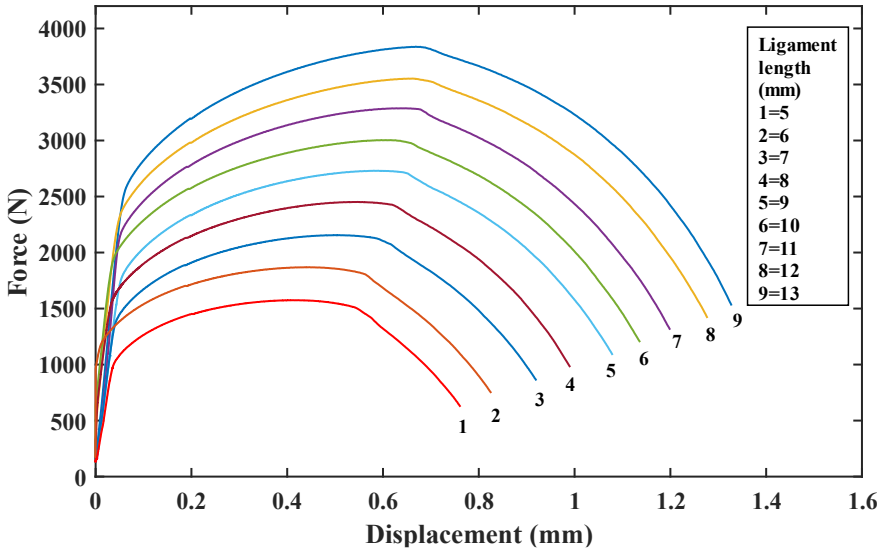

Figure 7.9 Force versus displacement (extensometer) diagram for notched samples prepared from the EDM.

Figure 7.11 shows the specific work of fracture versus ligament length for notched samples prepared from the EDM (extensometer). The specific essential work of fracture *'w_e'* and slope of the fitted curve are 225.39±6.96 kJ/m^2 and 27.35±0.74 kJ/m^{3}respectively. An R^2 value of 0.9948 (Figure 7.11) indicates the fitted curve's good linearity. Figure 7.10 shows the graph of deformation at fracture versus ligament length for notched samples prepared from the EDM, and deformation is recorded from the extensometer. The determined CTOD δ_c^e and CTOA ψ^e from EWF tests are 0.4092±0.016 mm and 8.25º respectively. The fitted line has an R^2 value of 0.9960.

Table 7.3 EWF test outputs (extensometer displacements) for notched samples prepared from the EDM.

Ligament length (mm)	Maximum force (N)	Maximum stress(MPa)	Total work of fracture W_f(N-mm)	w_f (kJ/m^2)	v_f (mm)
5	1574.84	557.47	1002.91	355.02	0.7616
6	1869.41	551.45	1316.07	388.22	0.8259
7	2155.64	545.04	1647.40	416.54	0.9200
8	2451.69	542.41	2036.36	450.52	0.9909
9	2730.37	536.95	2428.02	477.49	1.0794
10	3004.02	531.68	2850.08	504.44	1.1367
11	3287.79	529.01	3254.73	523.69	1.1994
12	3552.87	524.02	3765.17	555.34	1.2774
13	3837.61	522.48	4208.17	572.93	1.3278

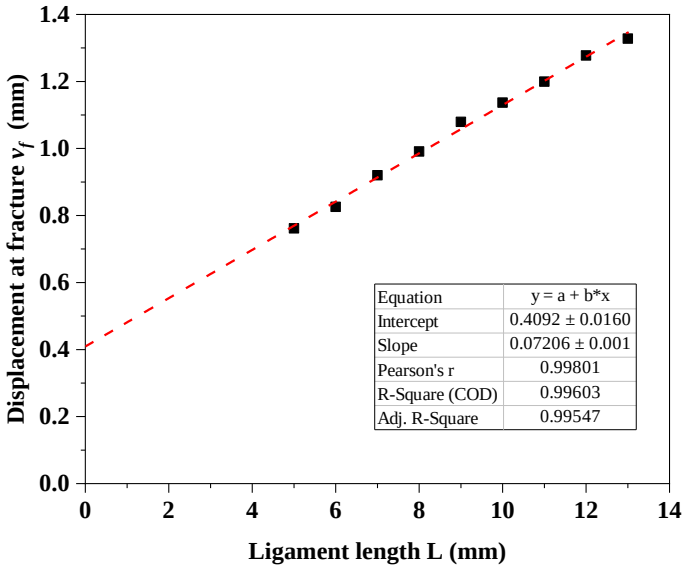

Figure 7.10 Deformation at fracture versus ligament length for notched samples prepared from EDM (extensometer).

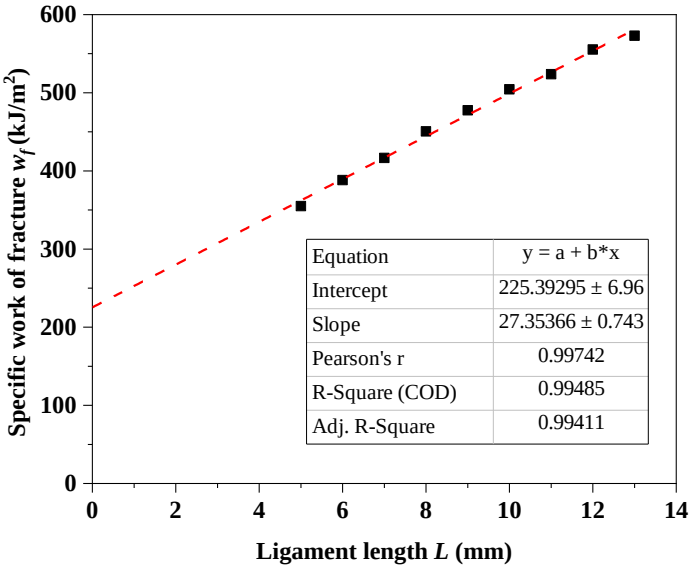

Figure 7.11 Specific work of fracture versus ligament length for notched samples prepared from EDM (extensometer).

In section 4.3.2, the experimental validity of the EWF test in terms of maximum stress is discussed in detail. One of the fundamental principles of the essential work of fracture methodology is to keep a similar stress state in all ligaments. The maximum stress in the ligament is calculated by dividing the maximum force by the initial ligament area. To verify the above condition, the maximum stress in the ligament is plotted against the ligament length. Figure 7.12 shows the maximum stress in the ligament versus the original ligament length for the notched samples prepared from the laser and the EDM. The maximum stress in the ligament is expected to be in the range of $0.9\sigma_u$ to $1.15\sigma_u$, an empirical estimation that a similar stress state (plane stress dominant) is maintained in all ligaments. In all the cases mentioned above, the maximum stress was in the specified range. Hence, a similar stress state is believed to have existed in all the ligaments during the EWF tests. The maximum stress in the ligament is slightly higher in the EDM samples than the laser samples. A general trend is that the maximum stress in the ligament increases with a decrease in the ligament length. The variation of the maximum stress is more pronounced for shorter ligaments; it indicates an increased portion of quasi-plane strain dominant condition at the crack initiation. Further increase in the ligament length would have reduced the maximum stress below the specified range.

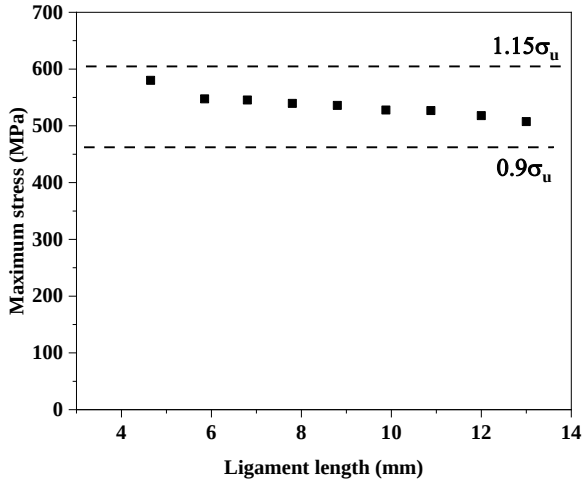

(a)

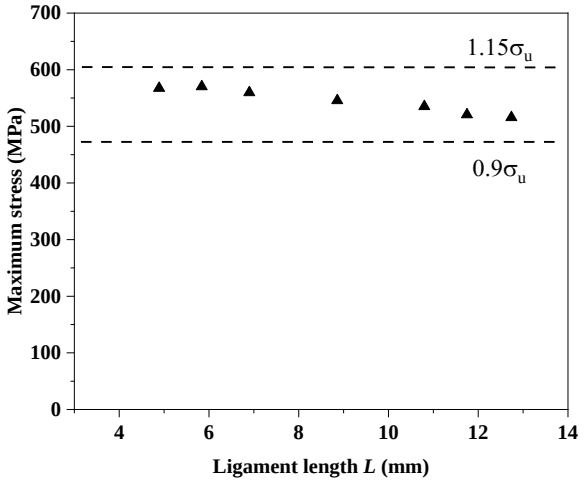

(b)

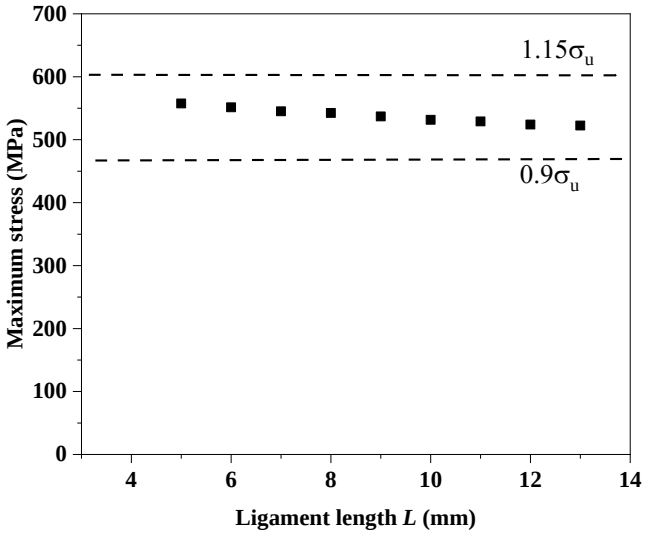

(c)

Figure 7.12 Maximum stress in ligament versus ligament length during EWF tests: (a) Laser notched(crosshead); (b) laser notched (extensometer); (c) EDM notched (extensometer).

7.2.1 Fatigue precracked samples

Fatigue pre-cracked samples are tested in two stages. In the first stage, the pre-cracked samples are tested, and deformation output is recorded from the crosshead movement. In the second stage, the pre-cracked samples are tested, and the deformation output is recorded from the extensometer. Section 5.3.3 explains the detail of the fatigue pre-crack test. Figure 7. 13 shows SEM images of the fatigue pre-crack and magnified striations of the fatigue crack.

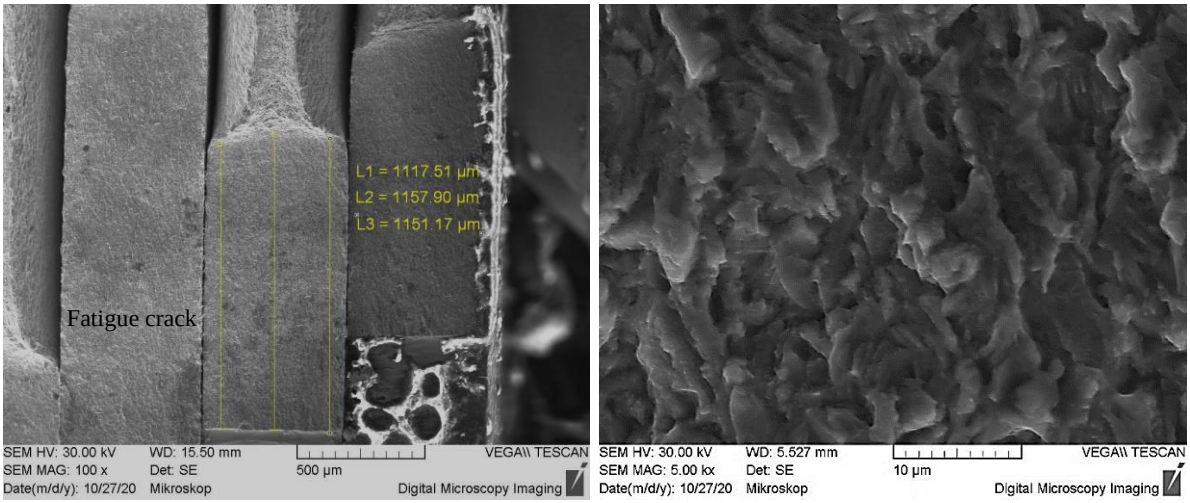

(a) (b)

Figure 7. 13 SEM images of (a) Fatigue pre-crack; (b) striations of the fatigue crack.

Table 7.4 & Table 7. 5 show the outputs and calculated parameters from force-displacement curves of EWF tests for the pre-cracked samples, and deformation is recorded from the crosshead (Table 7.4) and the extensometer (Table 7. 5), respectively. Figure 7.14 and Figure 7.15 show the force-deformation (displacement) curves for the pre-cracked samples. While in

the former, deformation is recorded using the crosshead movement and the extensometer in the latter. In Figure 7.15 (extensometer), the shape of the curves is similar for all the ligament lengths and no significant difference compared to the notched samples. However, in Figure 7.14 (crosshead), the shape of force-displacement curves is not perfectly similar for all ligament lengths. Like the notched samples, the force will gradually increase and decrease during the test. From the visual observation and the DIC images, crack initiation happens well before reaching the peak load for the precracked samples. After reaching the peak load, the decrease in load is not instantaneous rather more gradual. The gradual decrease in load indicates a good crack growth resistance and ductile fracture during the crack growth.

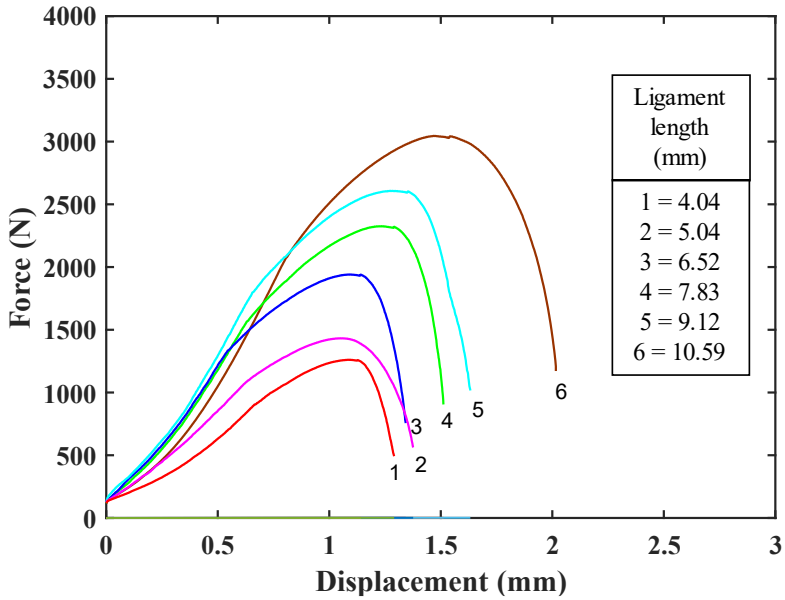

Figure 7.14 Force versus displacement (crosshead) diagram for precracked samples.

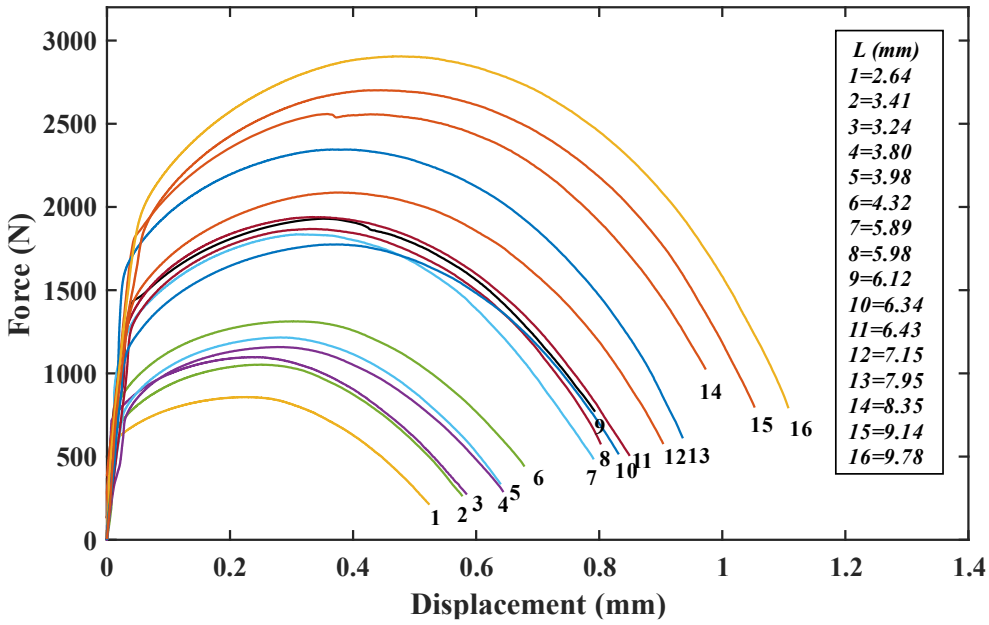

Figure 7.15 Force versus displacement (extensometer) diagram for precracked samples.

Figure 7.17 shows specific work of fracture versus ligament length for the precracked samples, and deformation is recorded from the crosshead. The specific essential work of fracture *'w_e'* and slope of the fitted curve are 266.79±17.79 kJ/m^2 and 36.88±2.01 kJ/m^3, respectively, which are significantly lower than the notched samples. An R^2 value of 0.9883 (Figure 7.17) indicates the fitted curve's decent linearity. Figure 7.16 shows the graph of deformation at fracture versus ligament length for the precracked samples, and deformation is recorded from the crosshead. The determined CTOD δ_c^e and CTOA ψ^e from EWF tests are 0.4085±0.077mm and 17.38º respectively. The fitted line has an R^2 value of 0.9868.

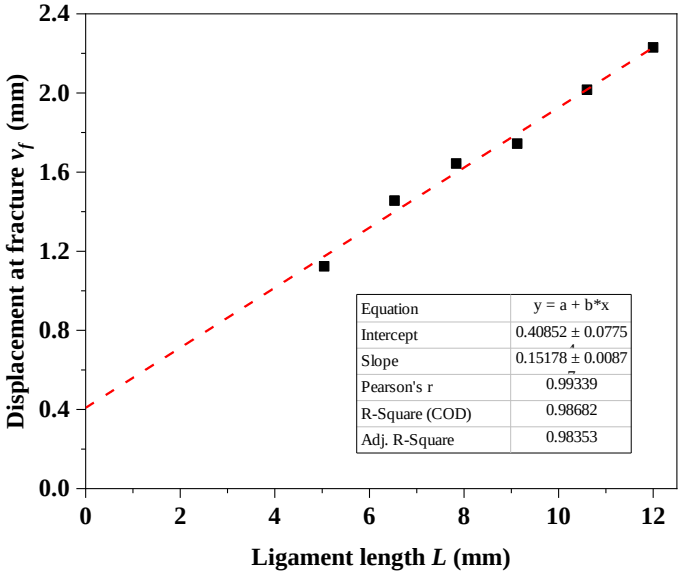

Figure 7.16 Deformation at fracture versus ligament length for precracked samples (crosshead).

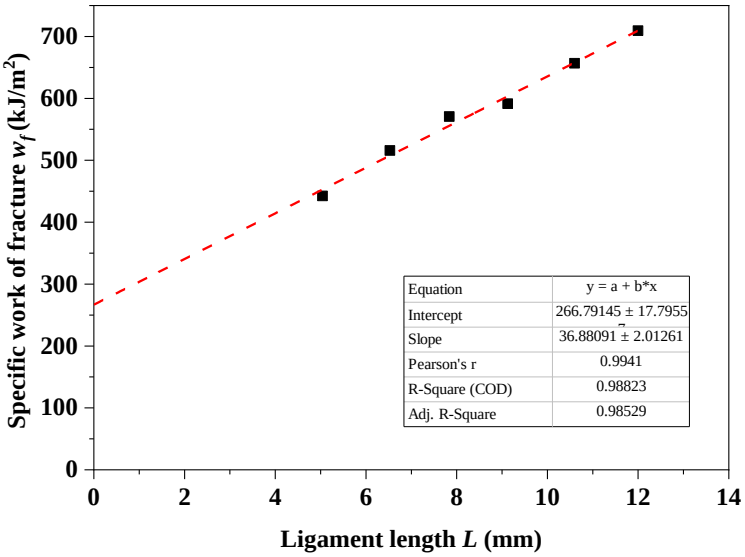

Figure 7.17 Specific work of fracture versus ligament length for precracked samples (crosshead).

Figure 7. 19 shows specific work of fracture versus ligament length for the precracked samples, and deformation is recorded from the extensometer. The specific essential work of fracture *'w_e'* and slope of the fitted curve are 154.22±7.26 kJ/m^2 and 32.34±1.15 kJ/m^3, respectively, which

are significantly lower compared to the notched samples. An R^2 value of 0.9824 (Figure 7. 19) indicates the fitted curve's decent linearity. Figure 7.18 shows the graph of deformation at fracture versus ligament length for the precracked samples, and deformation is recorded from the extensometer. The determined CTOD δ_c^e and CTOA ψ^e from EWF tests are 0.3251±0.01mm and 9.07º respectively. The fitted line has an R^2 value of 0.9917.

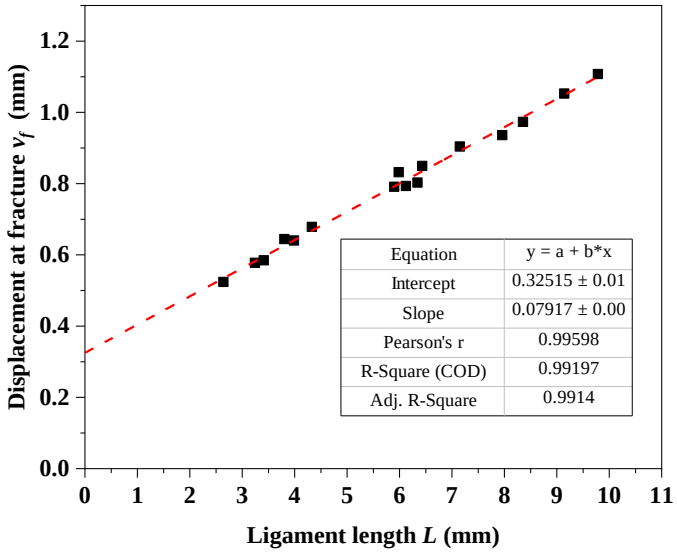

Figure 7.18 Deformation at fracture versus ligament length for precracked samples (extensometer).

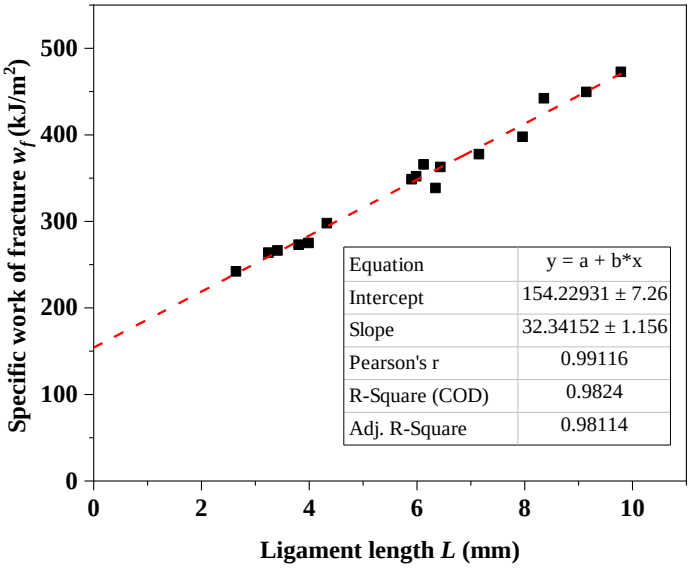

Figure 7. 19 Specific work of fracture versus ligament length for precracked samples (extensometer).

Figure 7.20 shows the maximum stress in the ligament versus the original ligament length for the precracked samples. The maximum stress in the ligament is well within the previously mentioned limit. However, the maximum stress of pre-cracked samples is slightly lower than the notched samples. Like the notched samples, the maximum stress increases with a decrease in ligament length. The variation in maximum stresses is predominant for smaller ligaments; due to increased quasi-plane strain area at the crack initiation.

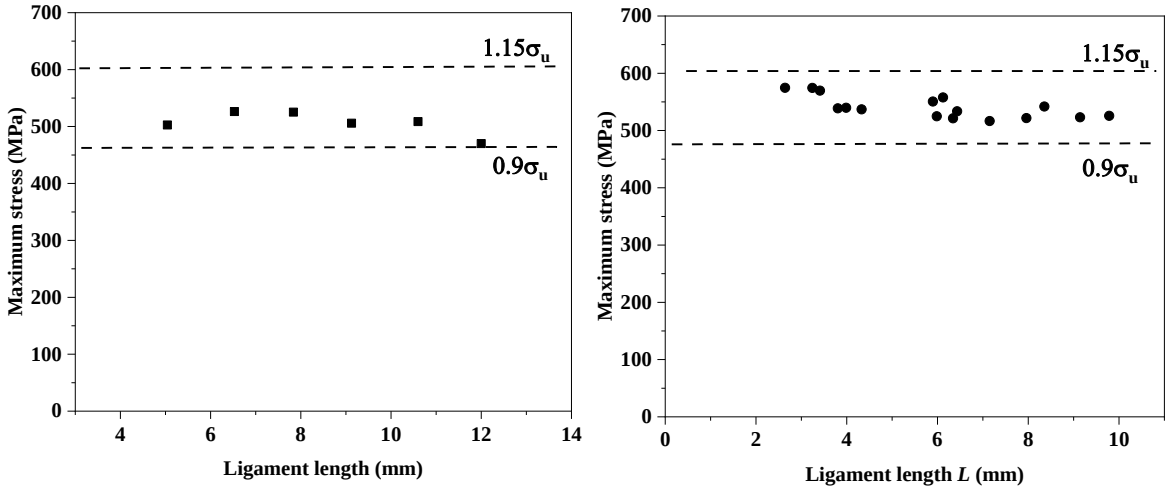

(a) (b)

Figure 7.20 Maximum stress in ligament versus ligament length during EWF tests: (a) precracked (crosshead); (b) precracked (extensometer).

Table 7.4 EWF test outputs (crosshead displacements) for precracked samples.

Effective ligament length (mm)	Maximum force (N)	Maximum stress(MPa)	Total work of fracture W_f(N-mm)	w_f (kJ/m^2)	v_f (mm)
5.04290416	1432.25	502.68	1260.76	442.49	1.1234
6.52920166	1941.48	526.29	1902.85	515.82	1.4558
7.83632666	2325.77	525.30	2526.97	570.74	1.6430
9.12559333	2607.79	505.78	3049.34	591.42	1.7437
10.5992	3046	508.64	3933.01	656.76	2.0159

Table 7. 5 EWF test outputs (extensometer displacements) for precracked samples.

Effective ligament length (mm)	Maximum force (N)	Maximum stress(MPa)	Total work of fracture N-mm(W_f)	w_f (kJ/m^2)	v_f (mm)
2.642	857.80	574.58	361.745	242.31	0.5238
3.243	1052.33	569.57	483.615	266.38	0.5777
3.411	1097.72	574.32	513.388	263.94	0.5847
3.805	1158.34	550.60	587.200	348.73	0.6443
3.987	1216.17	533.60	619.632	362.81	0.6402
4.327	1312.85	521.60	728.450	397.75	0.6786
5.899	1835.37	523.13	1162.455	449.67	0.7910
5.985	1774.89	525.56	1190.747	472.77	0.8318
6.123	1929.77	557.80	1265.791	365.87	0.7932
6.343	1868.07	541.98	1213.772	442.27	0.8028
6.432	1939.35	538.71	1318.616	273.09	0.8496
7.150	2087.01	536.92	1525.775	297.92	0.9041
7.959	2345.73	539.79	1788.782	275.02	0.9360
8.355	2558.51	521.20	2087.816	338.65	0.9732
9.141	2701.98	524.82	2322.549	352.09	1.0527
9.784	2905.48	516.62	2613.649	377.69	1.1076

7.2.3 Discussion of DP450 EWF results

Table 7. 6 tabulates the EWF test results for the notched and the precracked samples of the DP450 steel in all conditions. The main results of EWF experiments are specific essential work of fracture w_e and specific non-essential work of fracture w_p. Other parameters like crack tip opening displacement δ_c^e and crack tip opening angle ψ^e are determined from the deformation data. By comparing the results of extensometer and crosshead deformations, the crosshead deformation is larger in all specimens. Larger deformation recorded from the crosshead leads to higher specific essential work of fracture w_e and crack tip opening displacement δ_c^e. Specific essential work of fractures w_e are 352.88 kJ/m^2 and 200.14 kJ/m^2 for notched samples, where deformation is recorded from the crosshead and the extensometer, respectively. The specific essential work of fracture w_e determined from the crosshead movement is 76.31% larger than the w_e from the extensometer. Crack tip opening displacement δ_c^e determined from the crosshead movement is 100% higher than the δ_c^e from the extensometer. Parameters determined from the crosshead are significantly larger than the extensometer. Hence, parameters determined from the crosshead movement are only used for comparison and do not truly represent the actual values. From here onwards, only parameters determined from the extensometer are used for analyses.

Specific essential work of fractures w_e are 200.14 kJ/m^2 and 225.39 kJ/m^2 for notched samples prepared from the laser and EDM, respectively. Crack tip opening displacements δ_c^e are 0.3625 mm and 0.4092 mm for notched samples prepared from the laser and EDM, respectively. Specific non-essential work of fractures w_p ($w_p\beta$) are 26.16 kJ/m^3 and 27.35 kJ/m^3 for the notched samples prepared from laser and EDM, respectively. Crack tip opening angles ψ^e are 7.66º and 8.25º for the notched samples prepared from laser and EDM, respectively. The notch tip radii of 55 µm(laser) and 180 µm(EDM) have a considerable effect on the results. The DP450 steel is sensitive to variation in notch tip radius for the notched samples.

Specific essential work of fractures w_e are 200.14 kJ/m^2 and 154.22 kJ/m^2 for the notched and the precracked samples, respectively (extensometer). The specific essential work of fracture w_e for the notched samples is 30% higher than the w_e determined from the precracked samples. Crack tip opening displacement δ_c^e are 0.3625 mm and 0.3251 mm for the notched and the precracked samples, respectively (extensometer). The crack tip opening displacement δ_c^e for the notched samples is 11% higher than the δ_c^e for the precracked samples. Crack tip opening angles ψ^e are 7.66º and 9.07º for the notched and the precracked samples, respectively

(extensometer). The crack tip opening angle ψ^e for the precracked samples is 18% higher than the δ_c^e for the notched samples. Specific non-essential work of fractures w_p ($w_p\beta$) are 26.16 kJ/m^3 and 32.34 kJ/m^3 for the notched and the precracked, respectively (extensometer). The lowest possible notch tip radius is only achieved from fatigue precrack. Hence, the precracked sample result is believed to be closer to the actual fracture toughness. The parameters obtained from the EWF test of precracked samples are different from the notched sample results. The specific essential work of fracture *'w_e'* is the most sensitive to fatigue crack, and it is a significant output of the EWF test. Hence, the fracture toughness determined from the fatigue crack is believed to be the actual value. However, the crack tip opening displacement δ_c^e is less sensitive than the w_e to the fatigue precrack. The crack tip-opening angle ψ^e and the specific non-essential work of fracture *'w_p'* have the opposite effect on the presence of fatigue precrack. Both the parameters are lower for the fatigue-precracked samples compared to the notched samples. The critical information is that both the parameters (ψ^e & w_p) are determined from the slope. While the w_e and δ_c^e are determined from zero intercepts.

Table 7. 6 EWF test results for notched and precracked samples of **DP450** steel.

		$w_f = w_e + w_p L\beta$			$v_f = \delta_c^e + \frac{\psi^e}{2}L$		
Type	**Preparation method (Deformation recording)**	**w_e (kJ/m^2)**	**$w_p\beta$ (kJ/m^3)**	**R^2**	**δ_c^e(mm)**	**$\psi^e/2$ (ψ^e in θ°)**	**R^2**
Notched	Laser (Crosshead)	352.88±8.64	30.36±0.93	0.9934	0.6891±0.038	0.1192±0.004 (13.65º)	0.9913
	Laser (Extensometer)	200.14±4.84	26.16±0.52	0.9980	0.3625±0.016	0.06686±0.001 (7.66º)	0.9962
	EDM (Extensometer)	225.39±6.96	27.35±0.74	0.9948	0.4092±0.016	0.07206±0.001 (8.25º)	0.9960
pre-cracked	(Crosshead)	266.79±17.79	36.88±2.01	0.9883	0.4088±0.077	0.1517±0.008 (17.38º)	0.9868
	(Extensometer)	154.22±7.26	32.34±1.15	0.9824	0.3251±0.01	0.079117±0.038 (9.07º)	0.9917

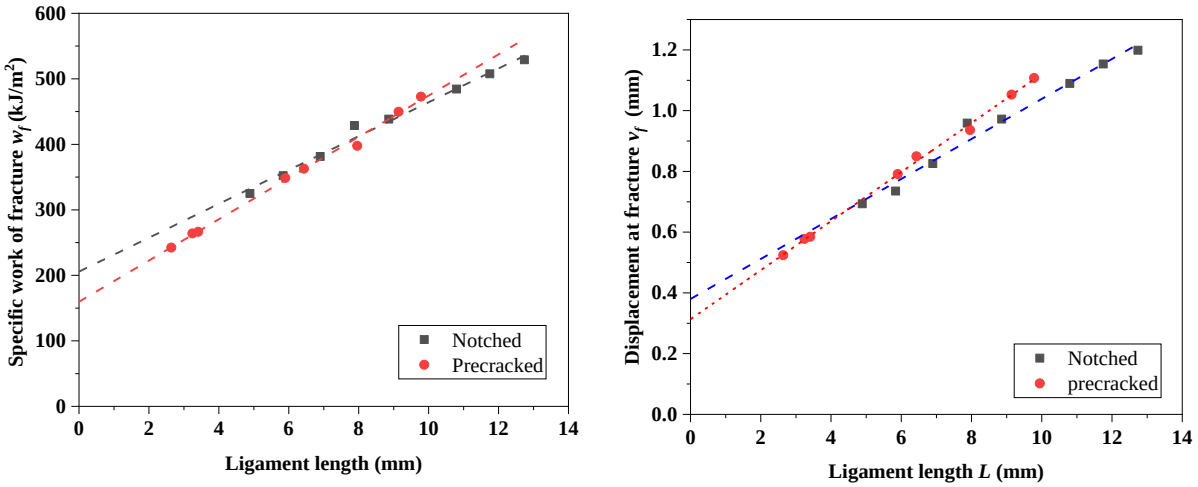

(a) (b)

Figure 7.21 (a) Ligament length vs. specific work of fracture; (b) ligament length vs. deformation at fracture for notched and precracked samples.

From Table 7. 6, it is clear that specific essential work of fracture w_e and crack tip opening displacement δ_c^e are lower for the precracked samples in comparison to the notched samples. However, it does not mean that for every ligament length, the precracked sample has less work of fracture W_f than the notched samples. Figure 7.21 shows the ligament length versus specific work of fracture (Figure 7.21(a)) and deformation at fracture (Figure 7.21(b)) for the notched and the precracked samples. For shorter ligament lengths, the total work of fracture W_f and the deformation at fracture v_f is smaller for the precracked samples. For larger ligament lengths, the total work of fracture W_f and the deformation at fracture v_f is larger for the precracked samples. Hence, the slope of the fitted curve for the notched samples is smaller than the precracked samples.

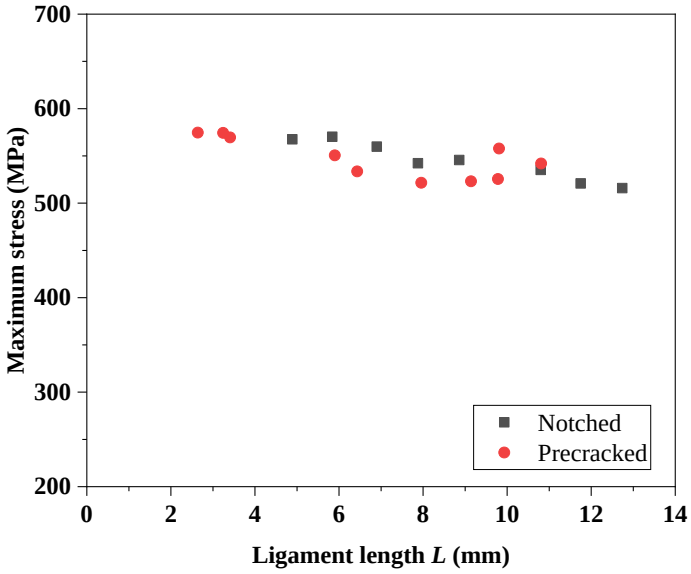

Figure 7.22 Maximum stress versus ligament length for notched and precracked samples.

The maximum force during the EWF test is directly influenced by crack initiation. As discussed earlier, the point of maximum force and the crack initiation is almost the same for the notched samples. However, for the precracked samples, the crack initiation happens well before reaching the maximum force. Figure 7.22 shows the maximum stress versus ligament length for the notched and the precracked samples. The maximum stress for the notched samples is slightly higher than the precracked samples. In the case of precracked samples, sharper crack helps in the early initiation of crack and reduces the maximum force. As ligament length increases, the energy consumed for crack propagation is more prominent than the energy consumed till the initiation.

7.3 Essential Work of Fracture test results for IF steel

The essential work of fracture tests for the IF steel is carried out identically to that of the DP450 steel. Dimensions of the sample, experimental parameters, and methodology are identical in both the IF steel and the DP450 steel. Section 7.2 explains the details of experimental data collection and methodology.

7.3.1 Notched samples

Notched samples prepared using the high-intensity precision laser are used for the EWF test of the IF steel. Deformation during the EWF test is recorded using an inbuilt extensometer.

Figure 7.23 shows the force-deformation curves for the notched samples of the IF steel. The area under the curve increases with an increase in ligament length without significant change in the curve's primary shape. Unlike the standard stress-strain curve, the force-displacement curve is parabolic in the EWF tests for the IF steel. Like the standard stress-strain diagram (Figure 6.6), in the beginning, a linear portion is observed before plastic deformation (Figure 7.23), and the curve is almost left-skewed parabola after deviating from the linear portion until fracture. Unlike the DP450 steel, the non-linear portion of the force vs. deformation curve is not symmetrical about the peak load. Similar to the DP450 notched samples, crack initiation happens near the peak load for the notched samples. After the crack initiation, the decrease in load is instantaneous compared to the DP450 steel curves (Figure 7.6). The relatively fast decrease in load is an indication of weak resistance to crack growth.

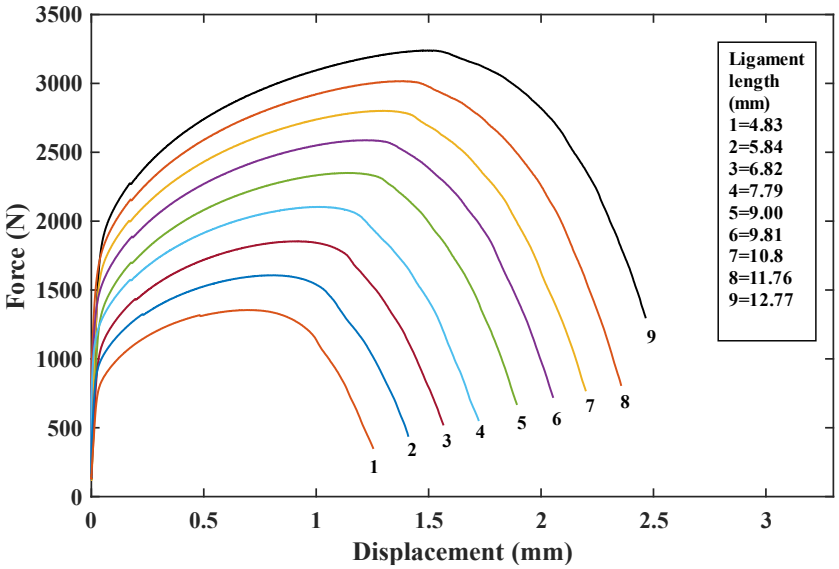

Figure 7.23 Force versus displacement diagram for notched samples of IF steel.

Table 7.7 shows the outputs and calculated parameters from force-displacement curves of the EWF tests for the notched IF steel samples. Figure 7.25 shows the specific work of fracture w_f versus original ligament length for the notched samples. From the extrapolation of data, the specific essential work of fracture is 212.63±8.45 kJ/m^2, and βw_p is 44.17±0.92 kJ/m^3. The R^2 value is equal to 0.9969 (Figure 7.25), which indicates a good linear fit. Good linearity proves that specific work of fracture increases linearly with ligament length. Figure 7.24 shows the graph of deformation at fracture versus ligament length for the notched samples. The data points are fitted with a linear curve equation to find crack tip opening displacement (CTOD) δ_c^e and crack tip opening angle (CTOA) ψ^e. The determined CTOD δ_c^e and the CTOA ψ^e from the EWF tests are 0.5042±0.02 mm and 17.86º respectively. The fitted line has an R^2 value of 0.9985.

Table 7.7 EWF test outputs for notched samples of IF steel.

Ligament length (mm)	Maximum force (N)	Maximum stress(MPa)	Total work of fracture W_f(N-mm)	w_f (kJ/m^2)	v_f (mm)
4.83	1355.27	409.62	1408.49	425.71	1.254
5.84	1607.56	401.84	1883.28	470.77	1.410
6.82	1854.36	396.93	2398.63	513.43	1.566
7.79	2103.9	394.27	2998.18	561.86	1.723
9.00	2350.53	381.27	3674.67	596.05	1.893
9.81	2587.78	385.09	4413.68	656.81	2.054
10.8	2802.11	378.76	5097.76	689.07	2.199
11.76	3017.07	374.53	5909.46	733.58	2.356
12.77	3240.60	370.46	6778.19	774.87	2.465

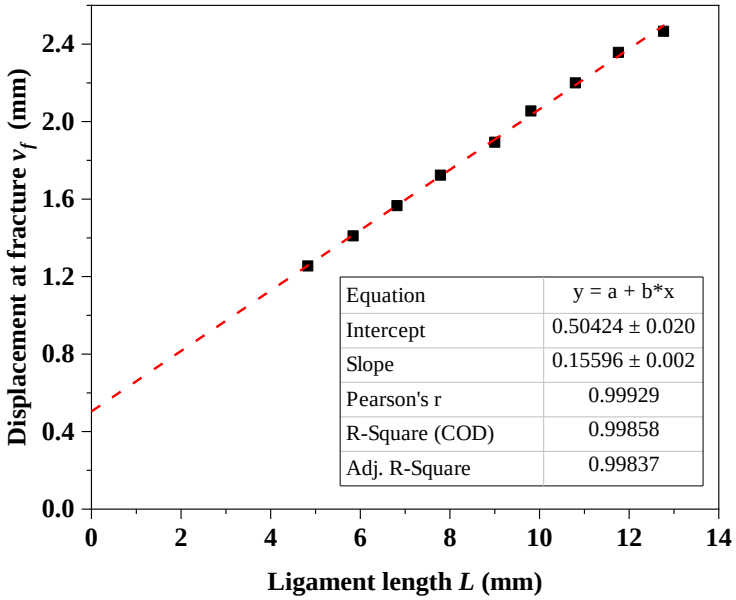

Figure 7.24 Deformation at fracture versus ligament length for notched samples of IF steel.

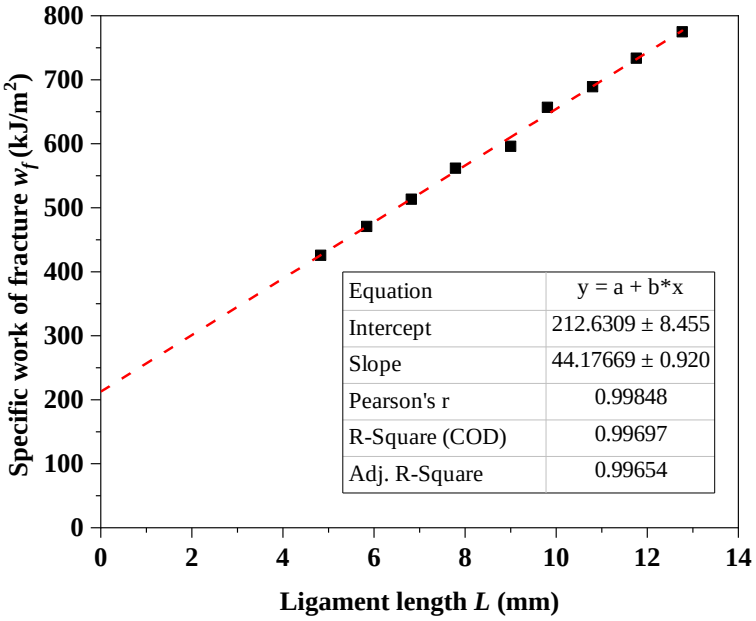

Figure 7.25 Specific work of fracture versus ligament length for notched samples of IF steel.

7.3.2 Precracked samples

Section 5.3.3 explains the detail of the fatigue pre-crack test. Figure 7.26 shows SEM images of the magnified fatigue crack. From the visual observation of the SEM images, the fatigue crack's morphology differs from the DP450 steel. In the DP450 steel, the fatigue crack path is intragranular. In the case of IF steel, the fatigue crack is partially intergranular. The presence of intergranular fatigue crack indicates relatively weaker grain boundaries[84]. The presence of carbides and nitrides along the grain boundary makes the grain boundary weaker than the rest of the grain. However, no brittle fracture is identified.

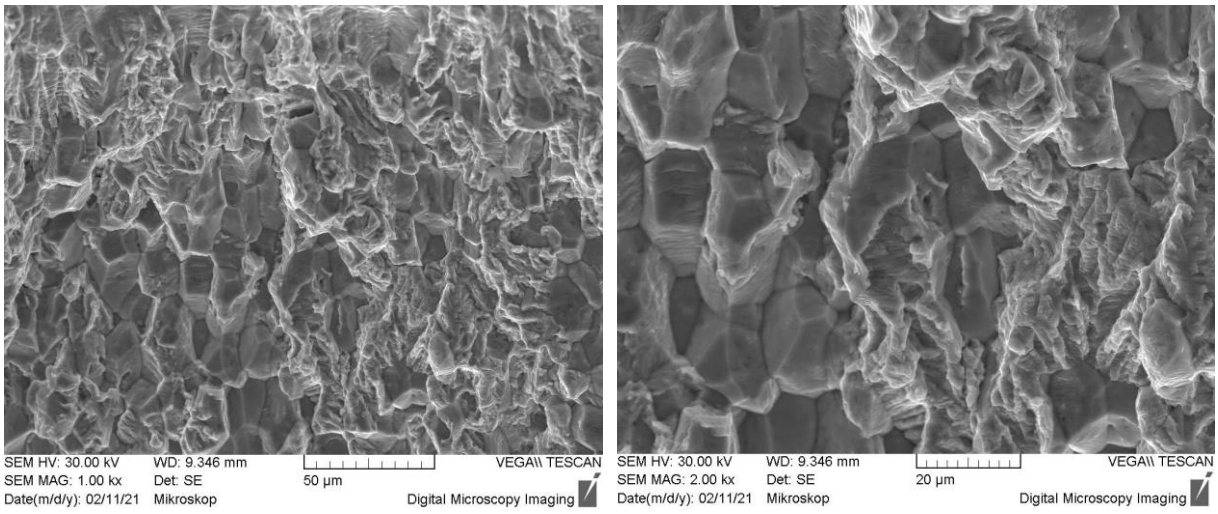

(a) (b)

Figure 7.26 SEM images of fatigue pre-crack of IF steel.

Table 7. 8 shows the outputs and calculated parameters from the force-displacement curves of the EWF tests for the pre-cracked samples. Figure 7.27 shows the force-deformation(displacement) curves for the pre-cracked samples. In Figure 7.27, the shape of the curves is identical to the notched samples. From visual observation and DIC images, crack initiation happens before reaching the peak load for the precracked samples. After reaching the peak load, the load decreases faster with shorter deformation.

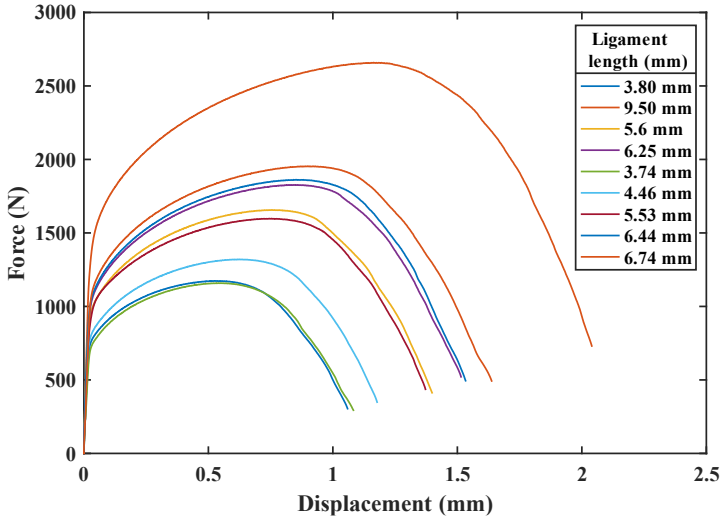

Figure 7.27 Force versus displacement diagram for precracked samples of IF steel.

Figure 7.29 shows the specific work of fracture versus ligament length for the precracked samples. The specific essential work of fracture *'w_e'* and slope of the fitted curve are 196.16±9.81 kJ/m^2 and 52.42±1.62 kJ/m^3, respectively. The R^2 value of 0.9933 (Figure 7.29) indicates the good linearity of the fitted curve. Figure 7.28 shows the graph of deformation at fracture versus ligament length for the precracked samples. The determined CTOD δ_c^e and CTOA ψ^e from the EWF tests are 0.426±0.028 mm and 19.76º respectively. The fitted line has an R^2 value of 0.9946.

Table 7. 8 EWF test outputs for precracked samples of IF steel.

Ligament length (mm)	Maximum force (N)	Maximum stress(MPa)	Total work of fracture N-mm(W_f)	w_f (kJ/m^2)	v_f (mm)
3.80	1174.12	450.82	1022.32	392.54	1.060
5.62	1657.02	429.81	1898.39	492.42	1.399
6.25	1827.27	426.17	2273.93	530.34	1.515
3.74	1159.16	451.93	1025.26	399.73	1.083
4.46	1320.57	432.25	1284.32	420.38	1.178
5.535	1597.98	421.46	1814.43	478.55	1.372
6.44	1862.67	421.76	2348.16	531.69	1.534
6.74	1954.30	422.72	2605.27	563.53	1.638
9.50	2659.06	408.41	4486.77	689.13	2.040

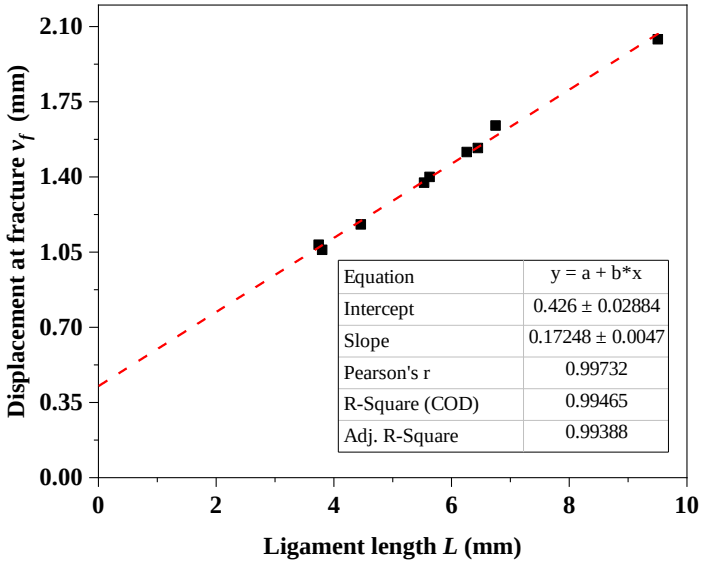

Figure 7.28 Deformation at fracture versus ligament length for precracked samples of IF steel.

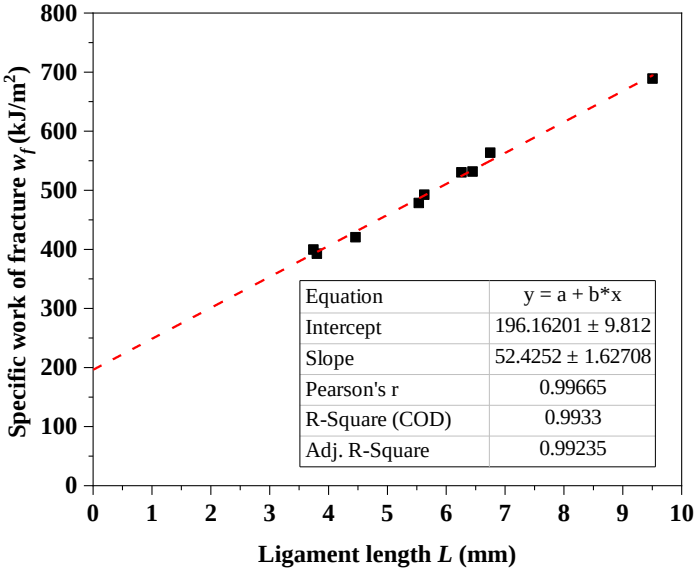

Figure 7.29 Specific work of fracture versus ligament length for notched samples of IF steel.

Figure 7.30 shows the maximum stress in the ligament versus ligament length for notched samples prepared from the laser. The maximum stresses in the ligaments are well above the range of $0.9\sigma_u$ to $1.15\sigma_u$. The maximum stress in the ligament is higher than the ultimate strength (standard tensile test). It is a clear indication that more energy is being consumed by the material away from the ligament. Hills[33] criteria to verify the plane stress condition may not be valid for the IF steel. However, if J.G. Williamson et al.[34] approach($1.1\sigma_{avg.}$-$0.9\ \sigma_{avg.}$) is used, the values are well within the limit. Like the DP450 steel, the maximum stress in the ligament increases with a decrease in the ligament length. Unlike the DP450 steel, the maximum stress is slightly higher for the fatigue pre-cracked samples.

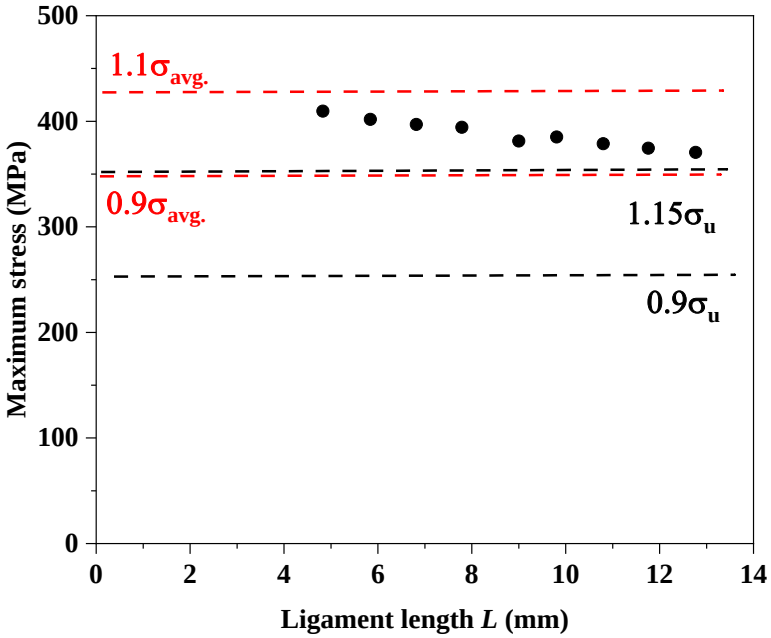

(a)

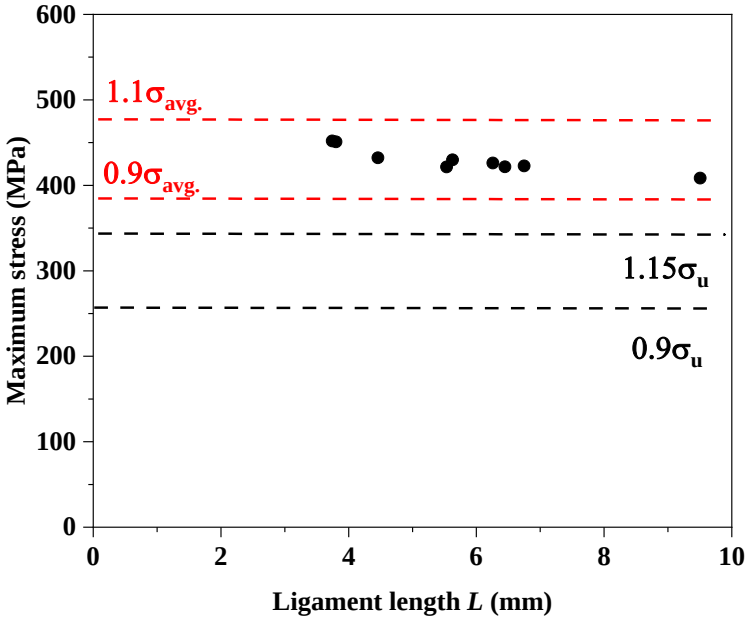

(b)

Figure 7.30 Maximum stress in ligament versus ligament length during EWF tests: (a) Notched; (b) precracked.

7.3.3 Discussion of EWF results of IF steel

Table 7. 9 tabulates the EWF test results for the notched and the precracked samples of the IF steel. The principal output of the EWF test is specific essential work of fracture we, which doesn't decrease significantly for the precracked samples compared to the notched samples. The specific essential work of fracture w_e for the notched samples is 8.39% larger than the precracked samples. Crack tip opening displacement δ_c^e for the notched samples is 17.93% larger than the precracked samples. Specific non-essential work of fracture w_p ($w_p\beta$) is higher for the precracked samples, i.e., the curve slope (specific work of fracture vs. ligament length) is higher for the precracked samples. Crack tip opening displacement δ_c^e is more sensitive than w_e to fatigue precrack. The crack tip opening angle ψ^e and the specific non-essential work of fracture *'w_p'* have an opposite effect on the presence of fatigue precrack. Both the parameters are higher for the fatigue precracked samples compared to the notched samples. The vital information is both the parameters(ψ^e & w_p) are determined from the slope. while w_e and δ_c^e are determined from zero intercepts. S.K. Chandra et al.[36] have performed EWF test for IF steel with similar mechanical properties to the steel used in this work. The w_e value for the notched sample is similar to the value found in this work; however, for the precracked samples, the difference is higher.

Table 7. 9 EWF test results for notched and precracked samples of **IF** steel.

	$w_f = w_e + w_p L\beta$			$v_f = \delta_c^e + \frac{\psi^e}{2}L$		
Type	w_e **(kJ/m²)**	$w_p\beta$ **(kJ/m³)**	R^2	δ_c^e**(mm)**	$\psi^e/2$ **(ψ^e in θ°)**	R^2
Notched	212.63±8.45	44.17±0.92	0.9969	0.5024±0.02	0.1559±0.002 (17.76°)	0.9985
pre-cracked	196.16±9.81	52.42±1.62	0.9933	0.426±0.028	0.1724±0.004 (19.76°)	0.9946

7.4 Comparison of EWF results between DP450 and IF steel

Essential work of fracture (EWF) methodology has been successfully used to calculate the fracture toughness of the Dual-phase (DP450) steel and the Interstitial free(IF) steel. These two sheets of steel have a different microstructure and mechanical properties. Both the sheets of steel have been tested in notched and precracked conditions. For comparison of notched samples, samples prepared using the laser are chosen. Table 7.10 shows the detailed comparison of the DP450 steel and the IF steel EWF test results.

Table 7.10 EWF test results for notched and precracked samples of **DP450** and **IF steel.**

		$w_f = w_e + w_p L\beta$			$v_f = \delta_c^e + \frac{\psi^e}{2} L$		
Type	**Material**	w_e **(kJ/m^2)**	$w_p\beta$ **(kJ/m^3)**	R^2	δ_c^e**(mm)**	$\psi^e/2$ **(ψ^e in θ°)**	R^2
Notched	**DP450**	200.14±4.84	26.16±0.52	0.9980	0.3625±0.016	0.06686±0.001 (7.66º)	0.9962
	IF steel	212.63±8.45	44.17±0.92	0.9969	0.5024±0.02	0.1559±0.002 (17.86º)	0.9985
pre-cracked	**DP450**	154.22±7.26	32.34±1.15	0.9824	0.3251±0.01	0.079117±0.038 (9.07º)	0.9917
	IF steel	196.16±9.81	52.42±1.62	0.9933	0.4260±0.028	0.1724±0.004 (19.76º)	0.9946

For the notched samples, the DP450 and the IF steels have w_e values of 200.14 kJ/m^2 and 212.63 kJ/m^2, respectively. The IF steel has about 6% higher w_e value than the DP450 steel. For the precracked samples, the DP450 and the IF steels have w_e values of 154.22 kJ/m^2 and 196.16 kJ/m^2, respectively. The IF steel has about **27%** higher w_e value than the DP450 steel. w_e for both the steels are approximately similar for the notched samples. However, w_e for the precracked samples have a significant difference. The presence of fatigue precrack in the DP450 steel has reduced w_e by about 23%, while only 8% for the IF steel. Crack tip opening displacement δ_c^e for the DP450 and the IF steel are 0.3625 and 0.5024 mm, respectively, for notched samples. IF steel has about **39%** higher δ_c^e value than the DP450 steel for the notched samples. Crack tip-opening displacement δ_c^e for the DP450 and the IF steel are 0.3251 and 0.4260 mm, respectively, for the precracked samples. For the precracked samples, the IF steel has about **31%** higher δ_c^e value than the DP450 steel. The presence of fatigue precrack in the DP450 steel has reduced δ_c^e by about 10%, while it is 15% for the IF steel. Specific non-essential work of fracture w_p ($w_p\beta$) for the DP450 and the IF steel are 26.16 kJ/m^3 and 44.17 kJ/m^3, respectively, for the notched samples. For the precracked samples, w_p ($w_p\beta$) for the

DP450 and the IF steel are 32.34 kJ/m^3 and 52.42 kJ/m^3, respectively. Crack tip opening angle ψ^e for the DP450 and the IF steel are 7.66º and 17.86º, respectively, for the notched samples. For the precracked samples, ψ^e for the DP450 and the IF steel are 9.07º and 19.76º, respectively.

Specific essential work of fracture w_e is sensitive to the notch tip radius; however, the sensitivity may vary from material to material. Both the DP450 and the IF steel have shown lower w_e value for the precracked samples. However, the IF steel is less sensitive to the notch tip radius than the DP450 steel**.** Based on w_e value, the IF steel's fracture toughness is higher than the DP450 steel by 27%. Crack tip opening displacement δ_c^e is also sensitive to the notch tip radius and has lower values for the precracked samples. Unlike w_e, δ_c^e is more sensitive to the notch tip radius for the IF steel. Based on δ_c^e value, fracture toughness of the IF steel is higher than the DP450 steel by 31%**.** From the comparison of both the parameters (w_e & δ_c^e) for the DP450 and the IF steel, the IF steel has higher fracture toughness than the DP450 steel.

Specific non-essential work of fracture w_p ($w_p\beta$) is the curve slope in the graph of specific work of fracture versus ligament length. For both the notched and the precracked samples, the IF steel has a higher slope ($w_p\beta$) than the DP450 steel. As discussed earlier in section 4.2, the total energy consumed to break the ligament is divided into two parts, viz, essential work of fracture and non-essential work of fracture. In the graph of specific work of fracture w_f versus ligament length L, specific essential work of fracture w_e is constant for all ligaments, and specific non-essential work of fracture w_p ($w_p\beta$) increases with an increase in ligament length. A higher slope indicates more energy (specific non-essential work of fracture w_p) consumed as ligament length increases. From the above results, the IF steel consumes a higher amount of the non-essential work of fracture energy (plastic work) as ligament length increases. In comparison, the DP450 steel's rate of the non-essential work of fracture energy (plastic work) consumption with ligament length is lower than the IF steel. The primary reason for the above difference might be the IF steel's ability to redistribute the stresses away from the ligament. The non-essential work is dependent on geometry and loading conditions; however, both the materials are tested in identical conditions, so it is fair to compare. Crack tip opening angle ψ^e is determined using slope from the graph of total elongation at fracture versus ligament length. For both the notched and the precracked samples, the IF steel has a higher ψ^e than the DP450 steel, in general, the IF steel has larger deformation at fracture for every successive ligament length.

7.5 Mode II and mixed-mode EWF tests

Section 6.2.2 explains the geometry of mode-2 and mixed-mode samples. The mode-2 and the mixed-mode tests are conducted to understand the applicability and effectiveness of the EWF method in various modes.

7.5.1 IF steel

Mode-2

Figure 7.31 shows the force-deformation (displacement) curves for the mode-2 samples of IF steel. In Figure 7.31, the shape of the curves is different compared to the mode-1 samples. From visual observation and DIC images, crack initiates in mode-1 (perpendicular to loading direction), and after a short propagation, it changes the direction to mode-2 (45º to the loading direction). After reaching the peak load, the load decreases faster with shorter deformation. Figure 7.32(a) shows the maximum stress in the ligament versus the original ligament length for the mode-2 samples. The stress in the ligament is within the limits of $1.15\sigma_u$ - $0.9\sigma_u$. Unlike the mode-1 samples, the maximum stress in the ligament is almost similar for all the ligaments. Figure 7.33 shows specific work of fracture versus ligament length for the mode-2 IF steel samples. The specific essential work of fracture *'w_e'* and slope of the fitted curve are 317.79±61.65 kJ/m^2 and 204.46±18.58 kJ/m^3, respectively. The R^2 value of 0.9603 (Figure 7.33) indicates the fitted curve's average linearity. However, the first and last values of the specific work of fractures are slightly away from the fitted line (Figure 7.33). If these two values are removed, the R^2 value increases to 0.9905; w_e and slope are changed to 365.35 kJ/m^2 and 185.11 kJ/m^3. Figure 7.32(b) shows the graph of deformation at fracture versus ligament length for the mode-2 IF steel samples. The determined CTOD δ_c^e and CTOA ψ^e from the EWF tests are 1.1788±0.260 mm and 98.52º, respectively. The fitted line has the R^2 value of 0.9599. If the first and last values (Figure 7.32(b)) are removed, the R^2 value increases to 0.9963; δ_c^e and ψ^e are changed to 1.2648 mm and 91.71º respectively.

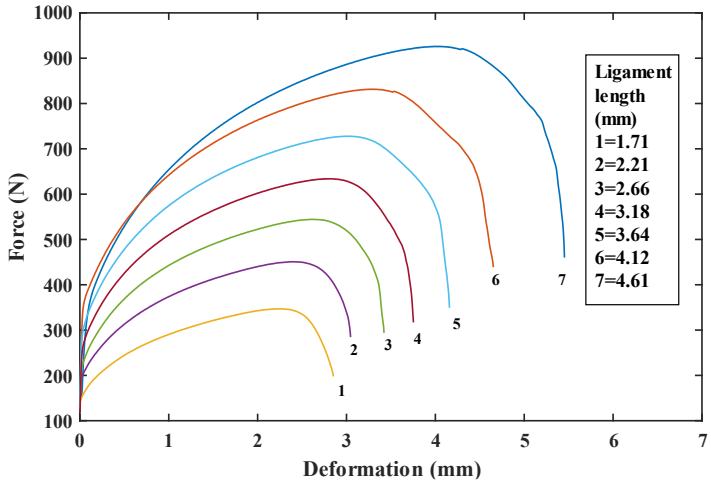

Figure 7.31 Force versus displacement diagram for mode-2 samples of IF steel.

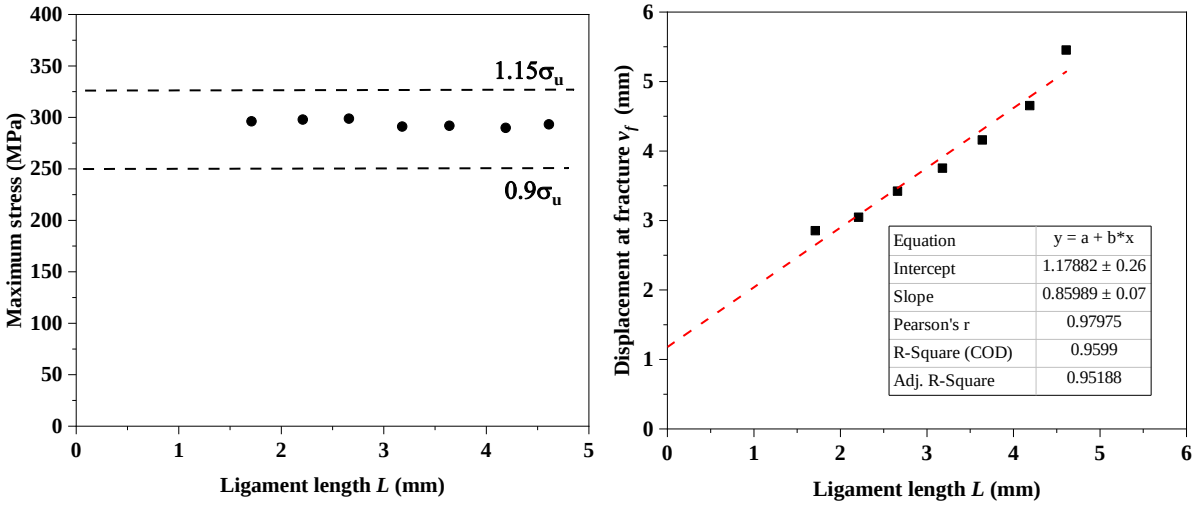

(a) (b)

Figure 7.32 (a) Maximum stress versus ligament length; (b) Deformation at fracture versus ligament length for mode-2 samples of IF steel.

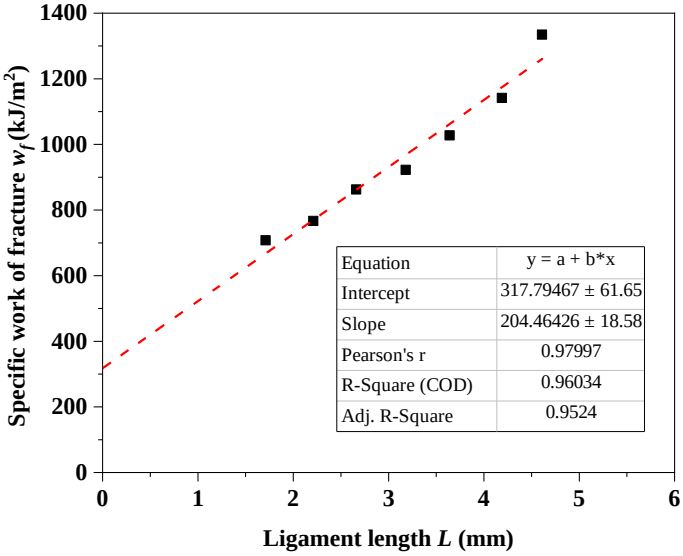

Figure 7.33 Specific work of fracture versus ligament length for mode-2 samples of IF steel.

Mixed-mode 30º

Figure 7.34 shows the force-deformation (displacement) curves for mixed-mode (30º) samples of the IF steel. In Figure 7.34, the shape of the curves is semi-circular. After reaching the peak load, the load decreases rather slowly with longer deformation. Figure 7.35(a) shows the maximum stress in the ligament versus the original ligament length for the mixed-mode (30º) IF steel samples. The stress in the ligament is almost within the limits of $1.15\sigma_u$ - $0.9\sigma_u$. Figure 7.36 shows specific work of fracture versus ligament length for the mixed-mode (30º) IF steel samples. The specific essential work of fracture *'w_e'* and slope of the fitted curve are 299.99±13.53 kJ/m^2 and 32.02±1.41 kJ/m^3, respectively. The R^2 value of 0.9883 (Figure 7.36) indicates a relatively good linearity of the fitted curve. Figure 7.35(b) shows the graph of deformation at fracture versus ligament length for the mixed-mode (30º) IF steel samples. The determined CTOD δ_c^e and CTOA ψ^e from the EWF tests are 0.9724±0.035 mm and 15.83º respectively. The fitted line has the R^2 value of 0.9957.

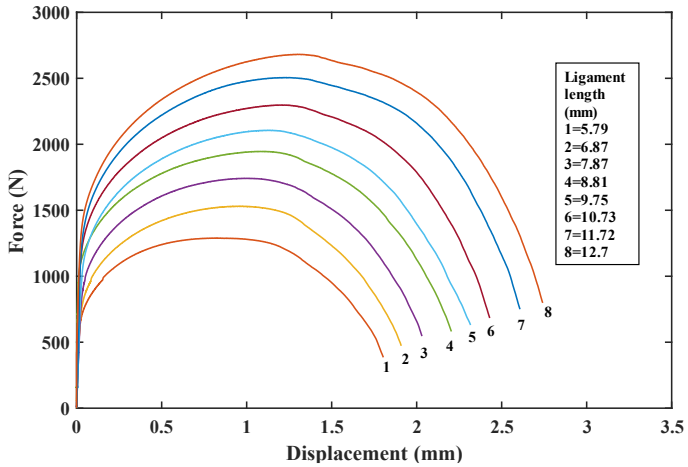

Figure 7.34 Force versus displacement diagram for mixed-mode (30º) samples of IF steel.

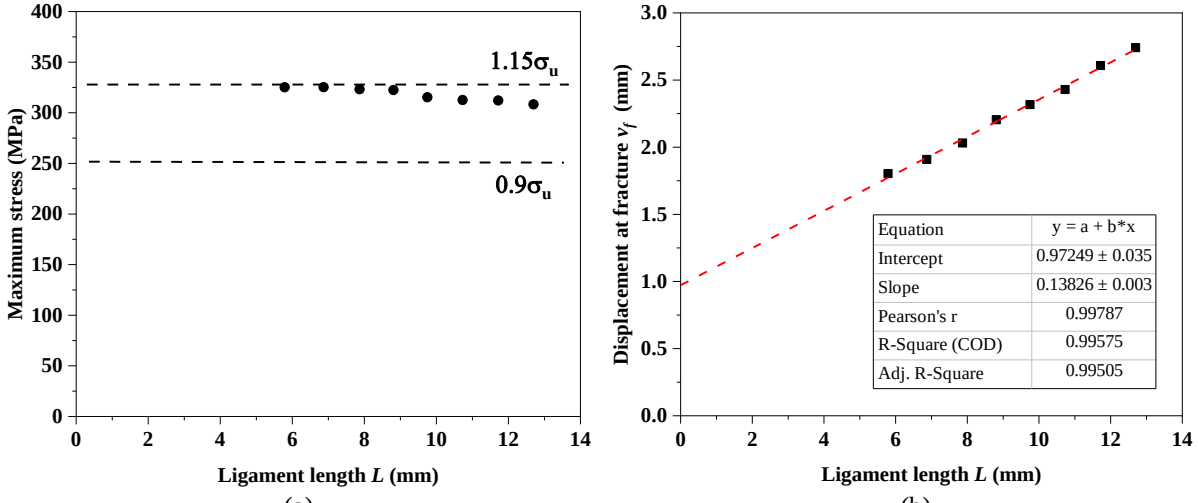

(a) (b)

Figure 7.35 (a) Maximum stress versus ligament length; (b) Deformation at fracture versus ligament length for mixed-mode (30º) samples of IF steel.

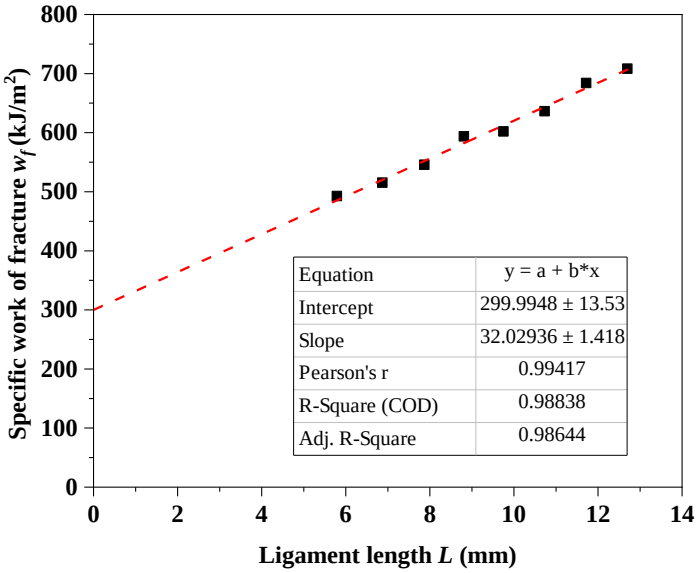

Figure 7.36 Specific work of fracture versus ligament length for mixed-mode (30º) samples of IF steel.

7.5.2 DP450 steel

Mixed-mode 30º

Figure 7.37 shows the force-deformation (displacement) curves for mixed-mode (30º) samples of the DP450 steel. In Figure 7.37, the curves' shape is not symmetrical about the peak load (right-skewed). After reaching the peak load, the load decreases slowly with larger deformation; the deformation after the peak load is larger than the deformation before the peak load. Figure 7.38(a) shows the maximum stress in the ligament versus the original ligament length for the mixed-mode (30º) DP450 steel samples. The stress in the ligament is slightly in and out of the limits of $1.15\sigma_u$ - $0.9\sigma_u$. Figure 7.39 shows the specific work of fracture versus ligament length for the mixed-mode (30º) DP450 steel samples. The specific essential work of fracture *'w_e'* and slope of the fitted curve are 215.29±14.78 kJ/m^2 and 36.12±1.61 kJ/m^3, respectively. The R^2 value of 0.9862 (Figure 7.39) indicates relatively good linearity of the fitted curve. Figure 7.38(b) shows the graph of deformation at fracture versus ligament length for the mixed-mode (30º) DP450 steel samples. The determined CTOD δ_c^e and CTOA ψ^e from the EWF tests are 0.5766±0.065 mm and 11.83º respectively. The fitted line has the R^2 value of 0.9680.

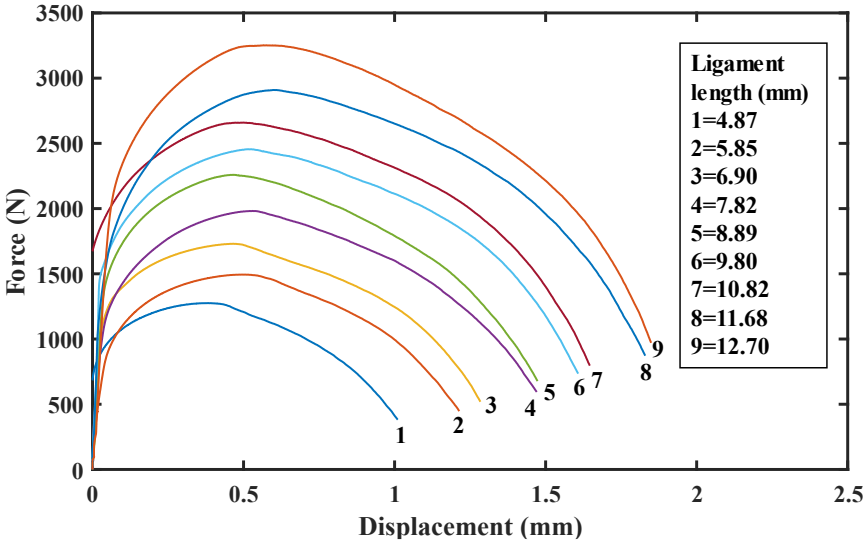

Figure 7.37 Force versus displacement diagram for mixed-mode (30º) samples of IF steel.

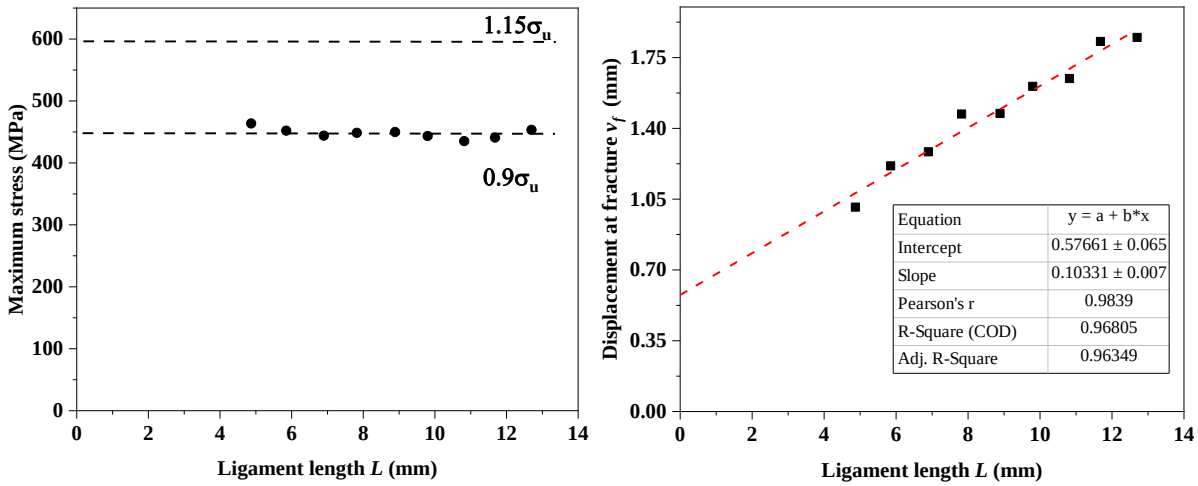

(a) (b)

Figure 7.38 Maximum stress versus ligament length; (b) Deformation at fracture versus ligament length for mixed-mode (30º) samples of DP450 steel.

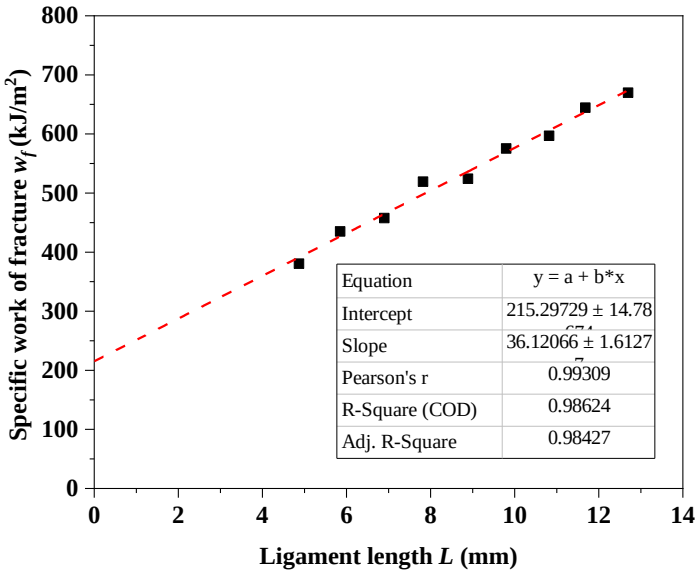

Figure 7.39 Specific work of fracture versus ligament length for mixed-mode (30º) samples of DP450 steel.

7.5.3 Discussion of mode-2 and mixed-mode results

Essential work of fracture (EWF) methodology has been applied to the IF and the DP450 steel in mode-2 and mixed-mode conditions. However, only the IF steel has been tested successfully. In the case of the DP450 steel, crack growth was not along the mode-2 direction, and the specimen experienced torsion. However, in the mixed-mode, the crack growth was through the ligament, and did not experience any torsion. Table 7.11 shows the EWF test results for the mode-2 and the mixed-mode samples of the DP450 and the IF steel.

Table 7.11 EWF test results for mode-2 and mixed-mode samples of **DP450** and **IF steel.**

		$w_f = w_e + w_p L\beta$			$v_f = \delta_c^e + \frac{\psi^e}{2} L$		
Material	**Type**	**w_e (kJ/m^2)**	**$w_p\beta$ (kJ/m^3)**	**R^2**	**δ_c^e(mm)**	**$\psi^e/2$ (ψ^e in θ°)**	**R^2**
DP450	**Mode-1**	200.14±4.84	26.16±0.52	0.9980	0.3625±0.016	0.06686±0.001 (7.66º)	0.9962
	Mixed mode (30º)	215.29±14.78	36.12±1.61	0.9862	0.5766±0.006	0.1033±0.007 (11.83º)	0.9680
IF steel	**Mode-1**	212.63±8.45	44.17±0.92	0.9969	0.5024±0.02	0.1559±0.002 (17.86º)	0.9985
	Mixed mode (30º)	299.99±13.53	32.09±1.41	0.9883	0.9724±0.035	0.1386±0.003 (15.88º)	0.9957
	Mode-2	317.79±61.65	204.46±18.58	0.9603	1.178±0.26	0.8598±0.078 (98.52º)	0.9599

All the samples are in notched condition (no fatigue precrack) due to complexity in the geometry. It is clear from the results that specific essential work of fracture w_e, crack tip opening displacement δ_c^e and crack tip-opening angle ψ^e increase as loading shifts from mode-1 to mode-2. João P. Magrinho et al.[45] have observed an increase in the slope of the curves (w_f vs. L) as loading shifts from mode-1 to mode-2 for copper and aluminium samples; however, w_e values did not follow any trend. In the case of the IF steel, both w_e and δ_c^e are higher for the mode-2 samples. The EWF methodology for mode-2 and mixed samples has yet to be adequately verified. However, this experimental testing shows that it is likely possible to apply this methodology to mode-2 and mixed-mode conditions.

8. MICROSTRUCTURAL AND FRACTOGRAPHIC EVALUATION

Research of fracture response based on energy absorption at plane stress conditions requires the comprehensive study of all influencing material parameters. The phase composition, grain size, secondary phases distribution, etc., are influencing the basic parameters driving the capacity for plastic deformation of the material during the EWF testing. Usage of an electron backscattered diffraction (EBSD) method to study the microstructure and crystallographic texture is becoming a widespread option in recent years. EBSD quantitatively measures grain size, crystallographic orientations, misorientation within the grain, phase identification, dislocation density, and local deformation.

8.1 DP450 steel

Grain size

Grain size is one of the critical parameters, which has a significant influence on a material's mechanical properties. According to the Hall-Patch relationship, the strength of the material is inversely proportional to the square of the grain size. Smaller grain size helps in blocking crack propagation. Grain size can vary from nanometres to several centimetres. In EBSD analysis, crystal lattice orientation is used as a reference to identify grain boundaries. Generally, grain boundaries have higher misorientation than the rest of the grain. Grain boundaries are classified into two categories, which are LAGB (low angle grain boundary) and HAGB (high angle grain boundary). If the misorientation angle is less than 15º, it is classified as LAGB, and for HAGB, the misorientation angle is higher than 15º.

EBSD scanning is done for as received steels and deformed steels from the EWF test. The EBSD scanning is done on an area of 118×88 µm, resolution of 512×384 pixels, exposure time of 16.4 milliseconds, accelerating current of beam 20 kV, probe current of ~20 nA, step size of 0.23 µm/pixel and 60.2 fps. Figure 8.1(a) shows the grain-size distribution (number fraction) pattern obtained from the EBSD analysis. In Figure 8.1(a), colours are used to differentiate grains, and they do not signify any quantitative data. The average grain sizes are 6.31 µm and 7.23 µm (from two analyses and without considering grains smaller than 100 pixels). Figure 8.1(b) shows the graph of grain size versus number fraction. The grain size is relatively small and not uniform. Grain refinement is an excellent method to increase the strength without

significantly affecting the DP steels' ductility [85–87]. Uniform distribution of fine-grained martensite helps in reducing strain localisation and martensitic cracking[88]. The presence of a hard martensitic phase increases stress locally as well as in adjacent ferrite and changes plastic flow pattern during plastic deformation.

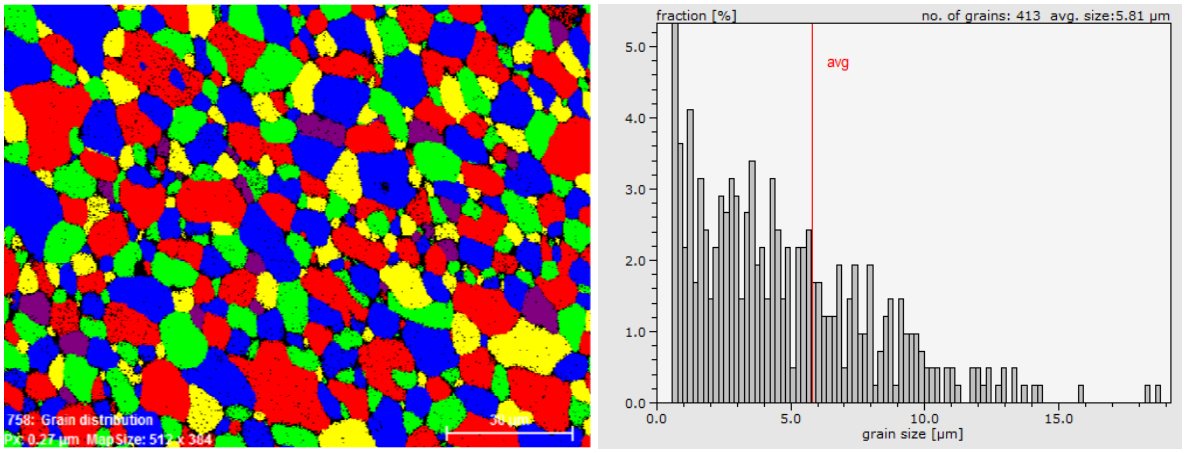

(a) (b)

Figure 8.1 (a) Grain size distribution pattern; (b) Grain size versus number fraction of DP450 steel.

Crystallographic texture maps

Ferrite and martensite have body centred cubic (BCC) and body centred tetragonal (BCT) crystal structures, respectively. Since BCC and BCT crystal structures are very similar, it is extremely hard to distinguish them in EBSD. Therefore, martensite is either wrongly identified as ferrite or not indexed at all. However, combined EDS analysis with EBSD, band slope maps, and other techniques are used to differentiate martensite from ferrite. If martensitic lattice distortion is high, it is indexed as a zero solution. If martensitic lattice distortion is low, it is wrongly indexed as ferrite[89]. The dark and the unindexed part in the IQ (image quality) map can be considered as martensite; however, some small grains of the martensite is wrongly indexed as ferrite (Figure 8.2). Phase maps are constructed based on comparing the crystal lattice at each pixel with a standard crystal lattice. Image quality maps are constructed based on a brightness level of diffraction bands and depend on phase intensity, orientation, and dislocations[90]. A slight trace of residual austenite and cementite were identified along the grain boundaries. Cementite in small quantities along grain boundaries will increase the strain hardening of ultra-fine-grained dual-phase steels.

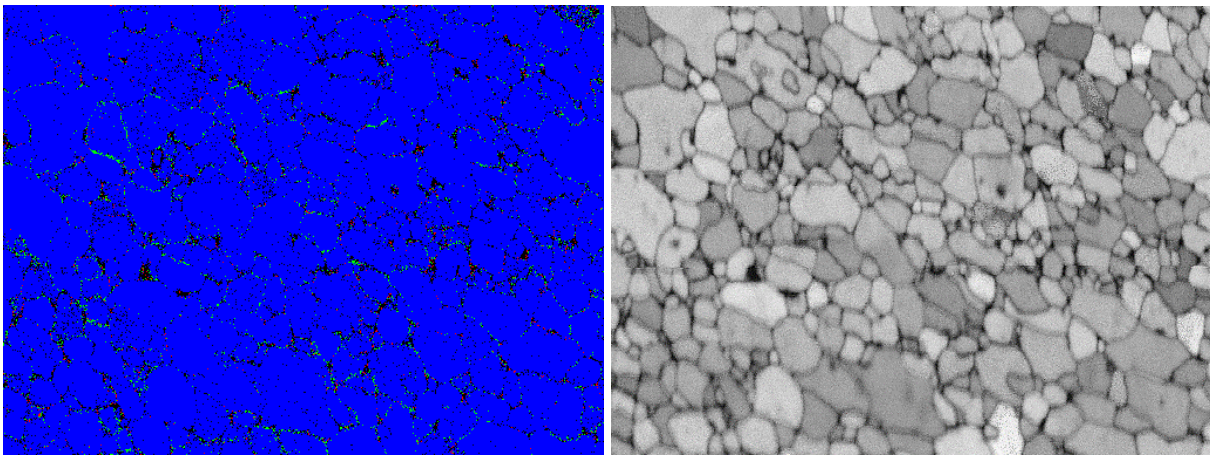

(a) (b)

Figure 8.2 (a) Phase map(blue-ferrite, green- residual austenite, and red-cementite); (b) IQ map of DP450 as-received steel.

Crystallographic orientation data obtained during EBSD scanning helps in identifying the texture of grains. The orientation of the crystal lattice in each grain may not be the same. A texture depends on heat treatment and subsequent mechanical processes during manufacturing. Pole figures are used to identify crystallographic orientation at each pixel. Each crystal lattice direction is projected in stereographic projections with respect to standard directions(rolling, transverse and normal). Inverse pole figure (IPF) map uses basic colours to assign the crystal lattice orientation at every pixel with respect to anyone's standard direction. For cubic crystals, each family of planes {111},{110} and {100} are assigned with a single colour. Figure 8.3 shows the inverse pole figure (IPF) maps in the z-direction. There is no single orientation texture seen from the figure; however, a considerable amount of γ-fiber({111}||ND) in the normal direction is visible (Figure 8.4 & Figure 8.5). The crystallographic orientation along {100} in the normal direction is detrimental for formability; a small number of grains are oriented in the {100}||ND direction (Figure 8.3). The lower ratio of {111}/{100} is an indication of poor formability. Upon deformation, the crystal lattice oriented close to {111}||ND rotated towards stable {111} and H.N. Han et al.[91] reported similar behaviour for DP steel after equi-biaxial tension. Also, the crystal lattice along {110} in the transverse direction becomes more intense.

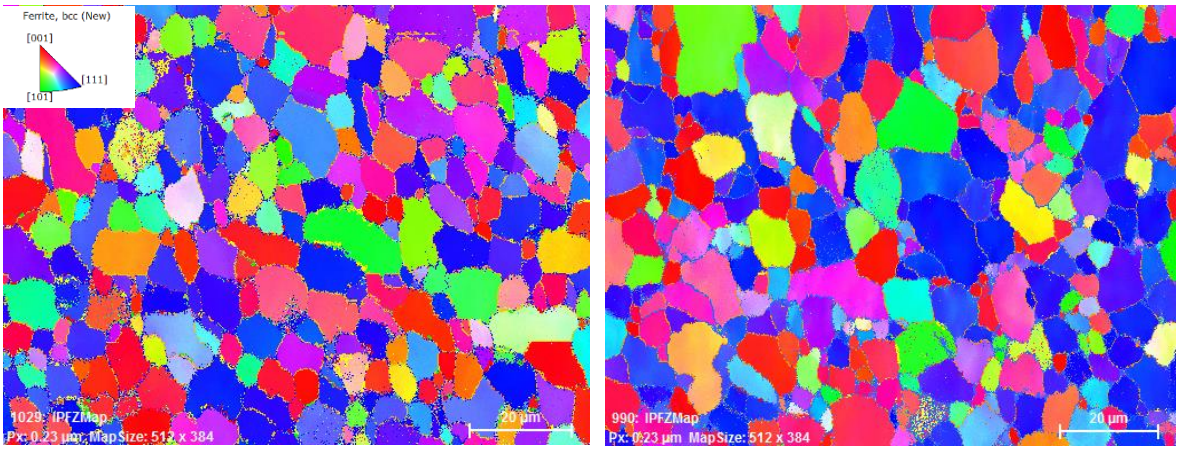

(a) (b)

Figure 8.3 (a) Inverse pole figure map of as received and; (b) after EWF test of DP450 steel in normal-direction.

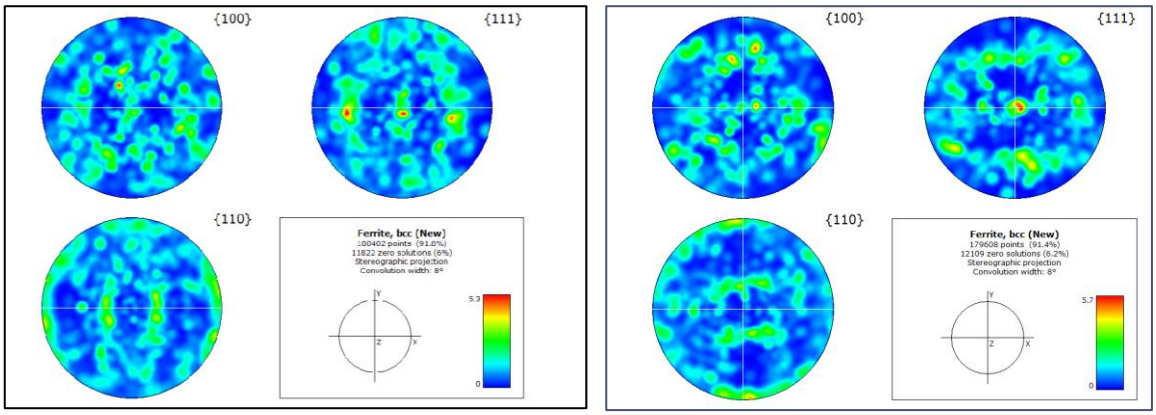

(a) (b)

Figure 8.4 (a) Pole figure of as received(X-transverse direction and Z-normal direction) and; (b) pole figure after EWF test of DP450 steel (X-rolling direction and Z-normal direction).

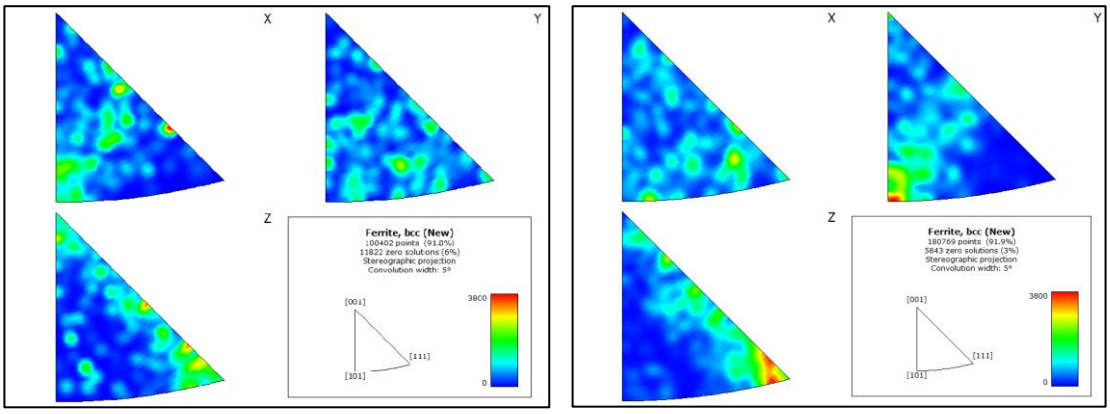

(a) (b)

Figure 8.5 (a) Inverse pole figure of as received(X-transverse direction and Z-normal direction) and; (b) inverse pole figure after EWF test of DP450 steel (X-rolling direction and Z-normal direction).

Local misorientation within a grain can be identified using Kernel misorientation maps. Kernel average misorientation(KAM) is the average misorientation difference between each pixel and its surrounding pixels in a crystal lattice. Generally, high KAM is an indication of higher misorientation, local strain, and dislocation density. Figure 8.6 shows the Kernel average

misorientation (KAM) maps of as received and after the EWF test for the DP450 steel. The secondary martensite phase induces a small amount of misorientation near the grain boundaries. Hence, KAM maps in the DP450 steel do not wholly depend on dislocation alone. From the KAM map after the EWF test(Figure 8.6(b)), the grain's deformation is not homogeneous. The deformation is concentrated mainly near the grain boundaries, while the centre portion of the ferrite grain experiences minor deformation. Several researchers have reported a similar behaviour for dual-phase steel[92,93]. During plastic deformation, the hard-secondary martensite phases are an obstacle for uniform plastic flow, enhancing the heterogeneous deformation. Small grains experience high deformation in comparison to large grains, where deformation is more heterogeneous. Martensite induces distortion even before the plastic deformation; hence, high misorientation near the grain boundary may be due to martensite. The level of deformation will increase in the necking region.

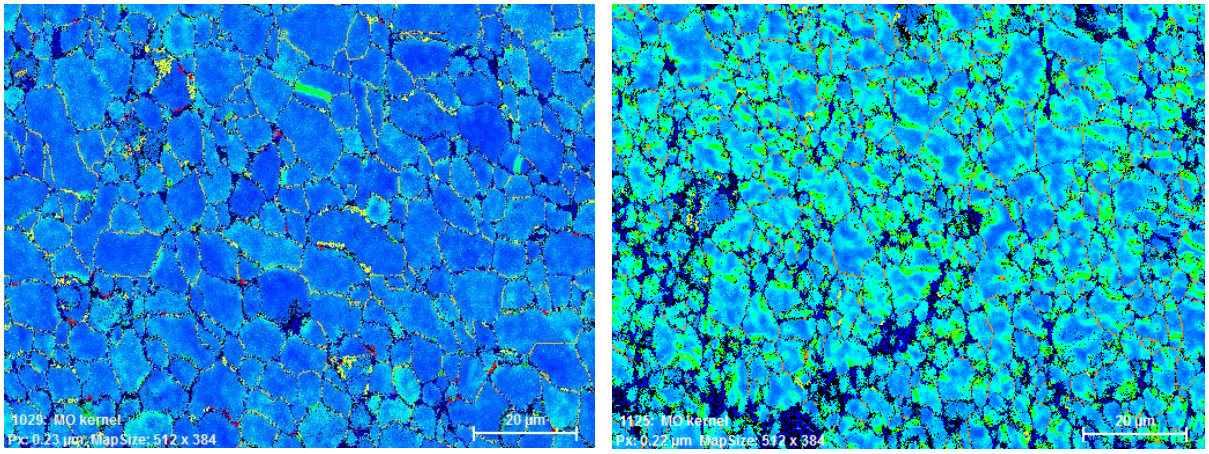

(a) (b)

Figure 8.6 Kernel average misorientation map of (a) as received; (b) after the EWF test of DP450 steel (0º-5º).

During the EWF test, the hard martensite phase acts as a path blocker for uniform plastic flow; it creates a higher dislocation density and misorientation in the ferrite phase adjacent to the martensite. The majority of the high misorientation happens close to the grain boundary. During quenching (production) of dual-phase steel, austenite will transform into martensite with a volume expansion of around 3%[89]. The volume expansion of martensite induces high misorientation and dislocation density in the ferrite (adjacent to the martensite). Figure 8.7 shows the grain boundary misorientation before and after the EWF test for the DP450 steel. However, scanning is not done in the same area, so it is not the best comparison. In any case, there has been an apparent increase in the low angle grain boundaries after deformation. The high angle grain boundary misorientation almost looks unchanged.

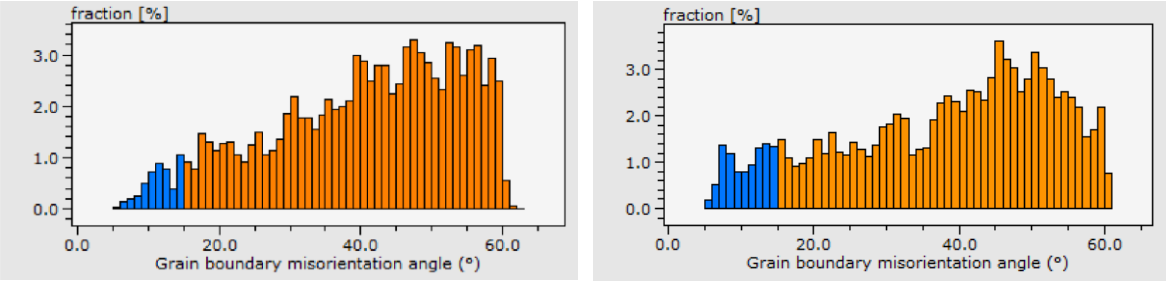

(a) (b)

Figure 8.7 Grain boundary misorientation angle of (a) as received and; (b) after EWF test of DP450 steel.

Figure 8.8 shows the misorientation inside a ferrite grain via line scan after the EWF test. Despite no change in overall crystallographic orientation, small misorientation can be seen along with the line scan.

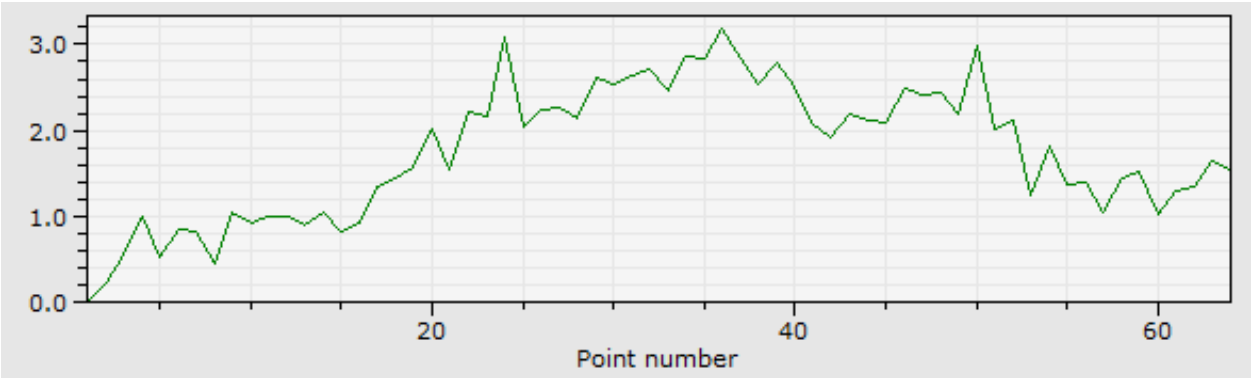

Figure 8.8 Misorientation using a line scan inside a ferrite grain after EWF test of DP450 steel.

8.2 IF steel

Grain size

Figure 8.9 shows the grain size distribution (number fraction) pattern obtained from an EBSD analysis, 18.85 µm and 15.35 µm (without considering grains smaller than 100 pixels) is the average grain size. The grain size is not entirely homogeneous and is relatively large in comparison to the DP40 steel. Grain refinement helps in increasing both strength and toughness in IF steel[94,95]. In the EBSD scanning, the step size is changed to 0.45 µm/pixel, and the rest of the parameters are the same. Figure 8.10 shows the phase map and IQ map of the IF steel in as-received condition. Primarily, the IF steel has ferrite only, and a considerable amount of LAGB is seen.

Crystallographic texture maps

Figure 8.11 shows the inverse pole figure(IPF) maps in the z-direction, before and after the EWF test. The initial crystallographic orientation of as-received IF steel has a strong γ-fiber

({111}||ND) and a partial α-fiber {110}||RD (Figure 8.11, Figure 8.12 & Figure 8.13). Recrystallization after cold rolling helped in achieving a uniform crystallographic orientation. A favourable {111} crystallographic orientation in the normal direction helps excellent plastic deformation without strain localization. Some researchers have reported that upon cold rolling γ-fiber {111}||ND and partial α-fiber {110}||RD increase in IF steel[96,97]. After plastic deformation (EWF test), the γ-fiber {111}||ND and the α-fiber {110}||RD are increased. A higher ratio of texture {111}/{100} is good for formability. Some researchers have reported an increase in γ-fiber upon plastic deformation[91], and a similar effect is also seen here. Francisco C.G. et al.[98] reported that γ-fiber({111}||ND) grains have more internal misorientation than α-fiber {110}||RD grains after plastic deformation.

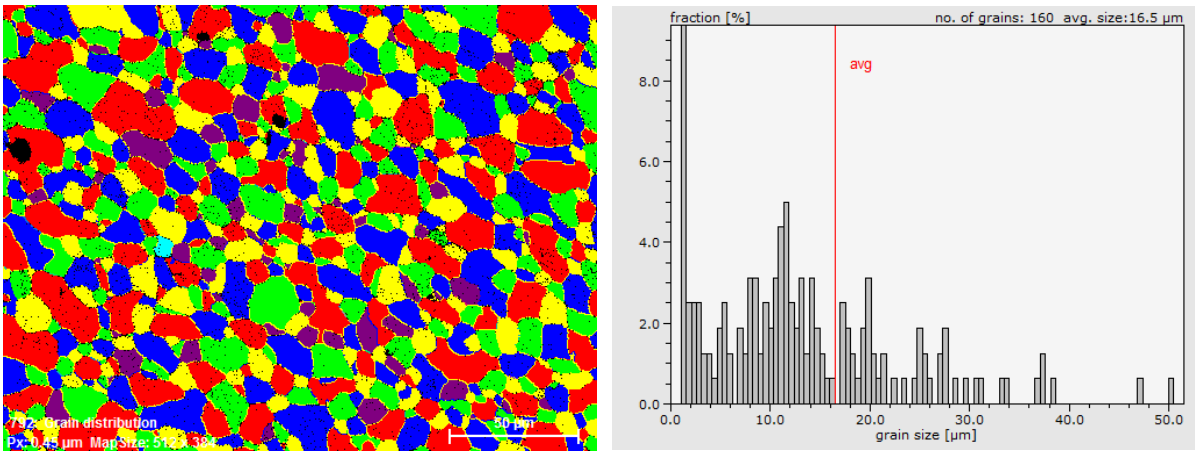

(a) (b)

Figure 8.9 (a) Grain size distribution pattern and; (b) Grain size versus number fraction of IF steel.

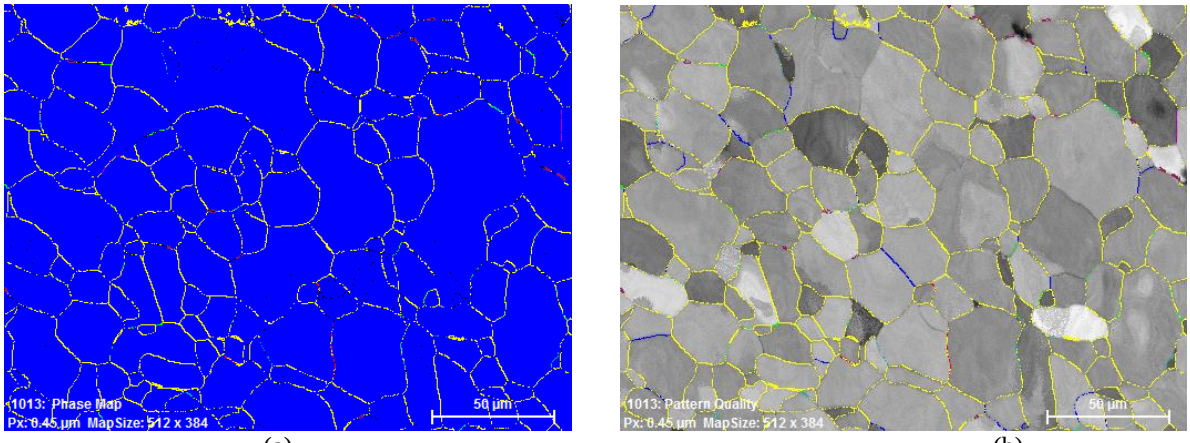

(a) (b)

Figure 8.10 (a) Phase map(blue-ferrite & white-grain boundary); (b) IQ map of IF steel in as-received condition (yellow-HAGB & blue-LAGB).

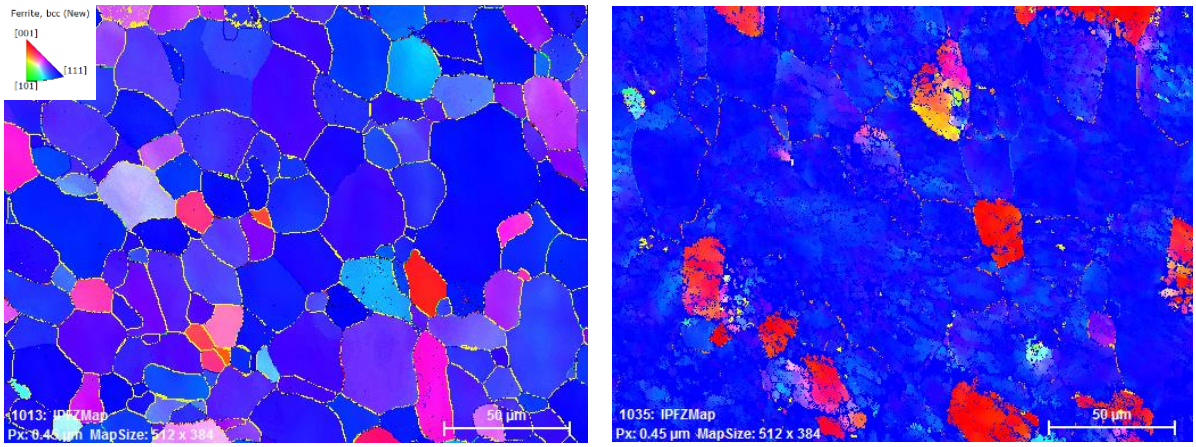

(a) (b)

Figure 8.11 Inverse pole figure maps of (a) as received and; (b) after EWF test of IF steel in normal-direction.

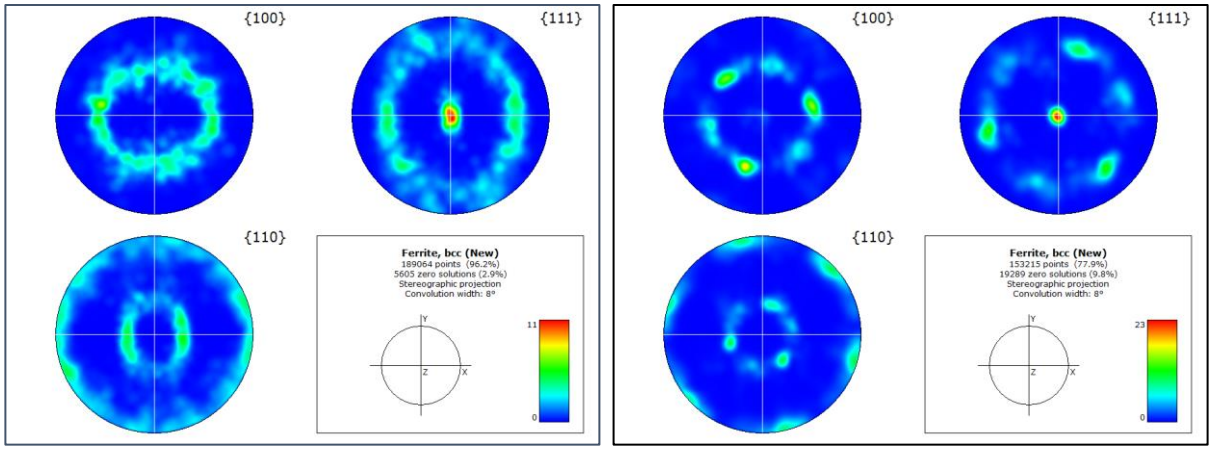

(a) (b)

Figure 8.12 (a) Pole figure of as received (X-transverse direction and Z-normal direction) and; (b) pole figure after EWF test of IF steel (X-transverse direction and Z-normal direction).

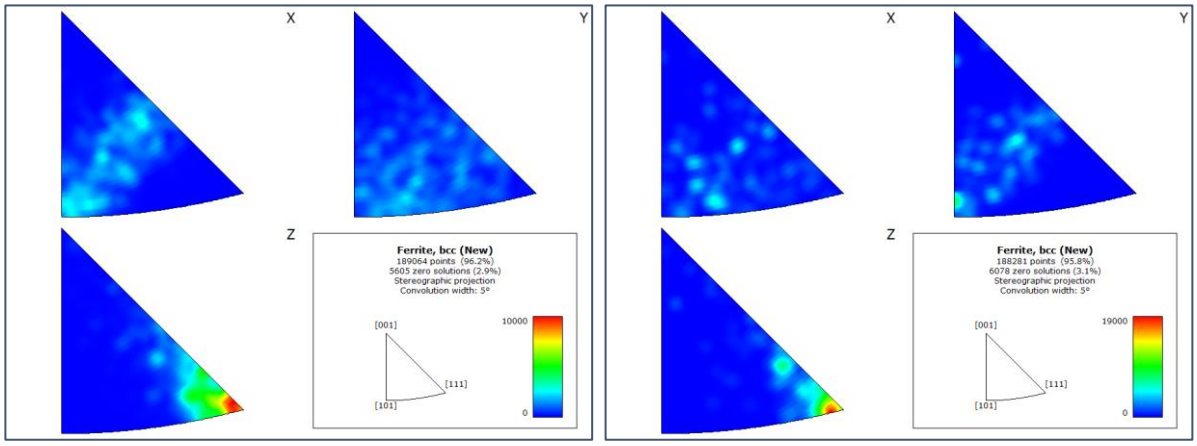

(a) (b)

Figure 8.13 (a) Inverse pole figure of as received (X-transverse direction and Z-normal direction) and; (b) inverse pole figure after EWF test of IF steel (X-transverse direction and Z-normal direction).

Local misorientation within the grain is analysed using the Kernel Misorientation maps (KAM). The local misorientation is directly linked with dislocation density. In as-received IF steel, misorientation is slightly higher in smaller grains(Figure 8.14(a)). After plastic

deformation, like the dual-phase steel, the IF steel also experiences heterogeneous deformation within ferrite grain (Figure 8.14(b)). However, the extent of heterogeneous deformation (misorientation) is less in the IF steel. The formation of sub-grains (LAGB) in the IF steels helps in accommodating more dislocations. The smaller grains experience more homogeneous and high deformation than large grains, where deformation is mostly heterogeneous. The local misorientation (or deformation) in IF steel is sensitive to strain rate, and it is well reported by Anindya Das[92].

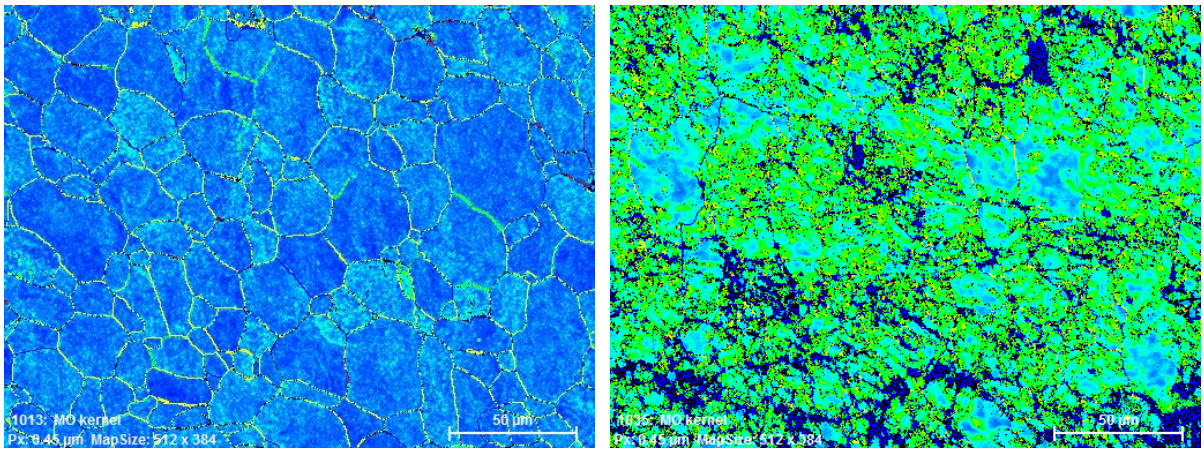

(a) (b)

Figure 8.14 Kernel average misorientation map of (a) as received and; (b) after EWF test of IF steel (0º-5º).

Figure 8. 15 shows misorientation inside a ferrite grain via line scan after the EWF test. The misorientation inside the ferrite grain is high. During plastic deformation, grains are deformed without a complete change in direction.

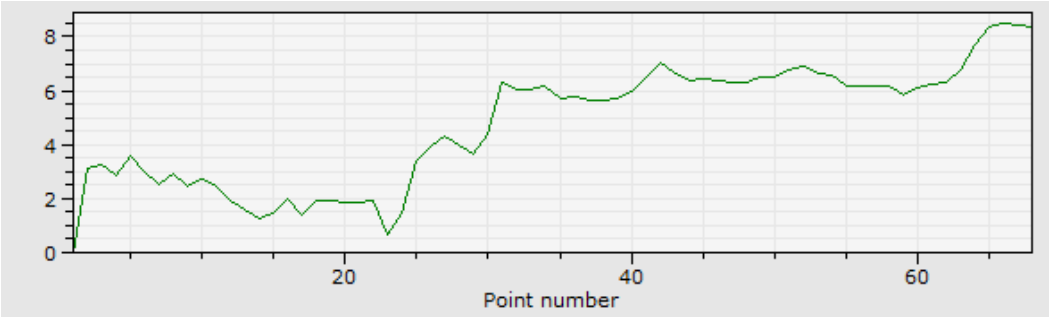

Figure 8. 15 Misorientation from line scan in the ferrite grain after EWF test in IF steel.

Figure 8.16 shows grain boundary misorientation before and after the EWF test. After Plastic deformation, the LAGB is significantly increased, and the HAGB misorientation angle is shifted. The LAGB is formed inside the ferrite grains. The HAGB misorientation angle is maximum around 20º and 55º.

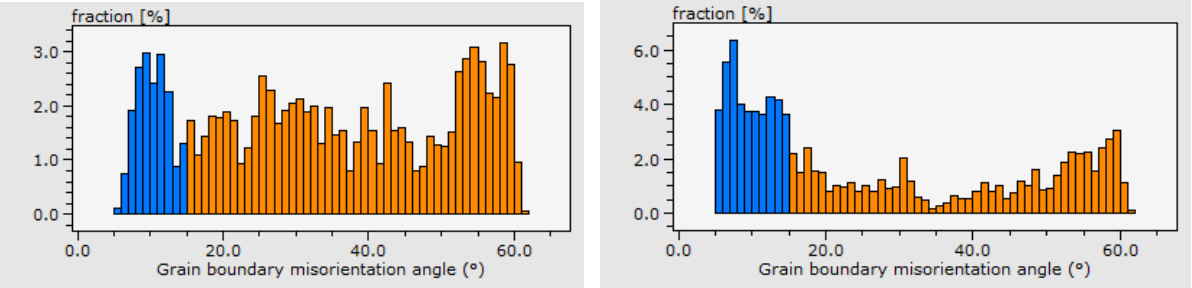

(a) (b)

Figure 8.16 Grain boundary misorientation angle of (a) as received and; (b) after EWF test of IF steel.

8.3 Fractographic evaluation

8.3.1 DP450 steel

Martensite content and distribution play a critical role in the fracture behaviour of dual-phase steel. Grain refinement has been shown to increase strength, initial strain hardening, and toughness of dual-phase steels[88]. Grain refinement has shown a positive response towards decreasing ductile-brittle transition temperature[99]. As discussed earlier in section 8.1, during quenching, the phase transformation (austenite into martensite) introduces stresses in the ferrite adjacent to the martensite. The heterogeneous dislocation density and strain in the ferrite grain causing the material to undergo early strain hardening. The carbon content of martensite plays an important role in the hardness of the martensite and ferrite. A lower amount of carbon inside martensite helps to avoid ferrite-martensite decohesion. The mode of void generation in dual-phase steel are martensite cracking, martensite-ferrite decohesion, and ferrite-ferrite decohesion[100]. Early martensitic cracking promotes strain localization and significantly reduces the ductility of dual-phase steel. The increased surface contact of ferrite and martensite helps in a high strain hardening rate.

After the EWF test, to prepare samples for fractographic evaluation, the tested samples are cut parallel to the loading axis. The samples are grinded (till 1500) and polished using a diamond paste of 3 and 1 µm. Figure 8.17 shows SEM micrographs of the DP450 steel in the necking and fracture region. In the DP450 steel, uniform distribution of martensite and smaller ferrite grain size is expected to produce a good fracture response. The ferrite matrix has undergone severe plastic strain, and the martensite plastic deformation is hard to identify from the visual analysis (but aligned in the loading direction). However, microscopically the deformation can be classified as heterogeneous. The primary mode void generation in the DP450 steel is by ferrite-martensite decohesion. The difference in plastic strain compatibility between the two phases is the primary reason for decohesion[88]. No martensite cracking or severe deformation

has been observed in the micrographs of the necking region. Martensitic cracking is a result of the extreme hardness of the martensite phase, which induces high stress on the martensite and severe strain on ferrite. The ferrite-ferrite decohesion is very rare and appeared only in proximity to martensite. Voids that appeared along the ferrite-ferrite grain boundary between closely situated martensite have grown longer (Figure 8.17(b)). In Figure 8.17(c), the decohesion that happened along the ferrite-martensite boundary has not grown larger, and the size of the martensite grain is larger. Voids formed at the end of a sharp martensite phase have grown longer. Voids also appeared in between two small martensite grains separated by a short distance.

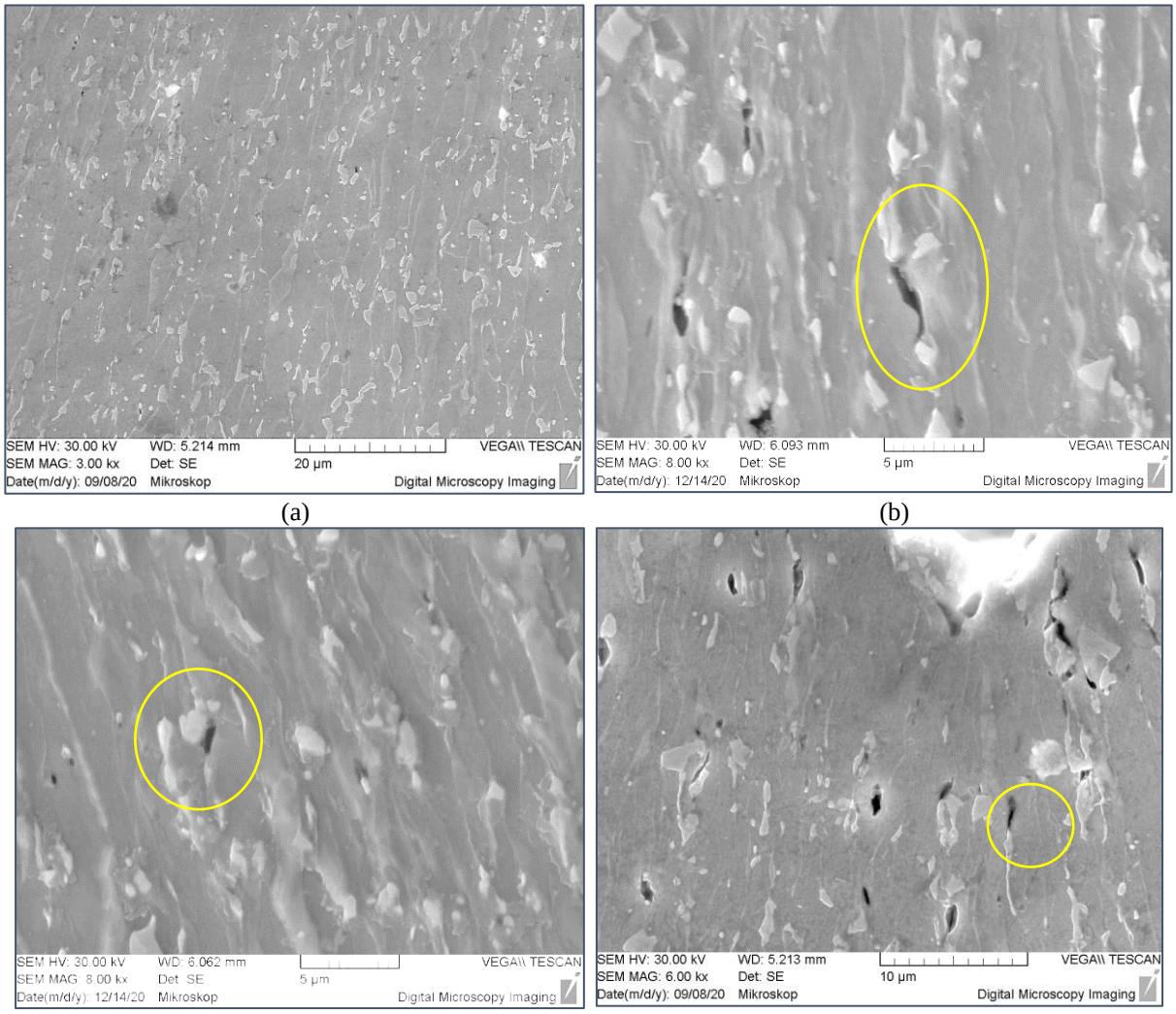

Figure 8.17 Voids formation in necking region of DP450 steel.

Figure 8.18 shows fractured surface at the crack tip and center of ligament, after the EWF test, for the laser notched (a & d), the EDM notched (b & e), and the precracked (c & f) samples. In all the conditions, morphology at the crack tip and the center of the ligament is similar. The

introduction of fatigue precrack has not changed the stress state and the fracture morphology. In all three conditions, ductile fracture prevails, which means that micro void nucleation and coalescence happened before the crack opening. Necking is wider at the beginning (Figure 8.18(a), (b) & (c)) and constantly decreases for a short distance (transitional distance) and remains constant for the rest of the ligament. At the crack tip, the stress state is quasi-plane strain and changes to the plane-stress dominant condition as the crack propagates. The distance over which the quasi-plane strain condition changes to the plane stress dominant condition is called transitional distance. The transitional distance is the same for all the ligament lengths and increases with thickness[21]. At the centre of the ligament, fractured morphology is dominated by slant fracture (45º to the loading), and a small flat fracture also visible. Type of fracture (slant or flat) is dependent on stress state, material properties, fracture strain, and many other factors. The slant fracture in the DP450 steel can be attributed to plane stress dominant condition and high strain hardening. At the beginning of the crack, the portion of the flat fracture against the slant fracture is high and decreases as the crack propagates. On the slant fractured surface, dimples are in mode-2 (45º to the loading) and disappeared at the edge.

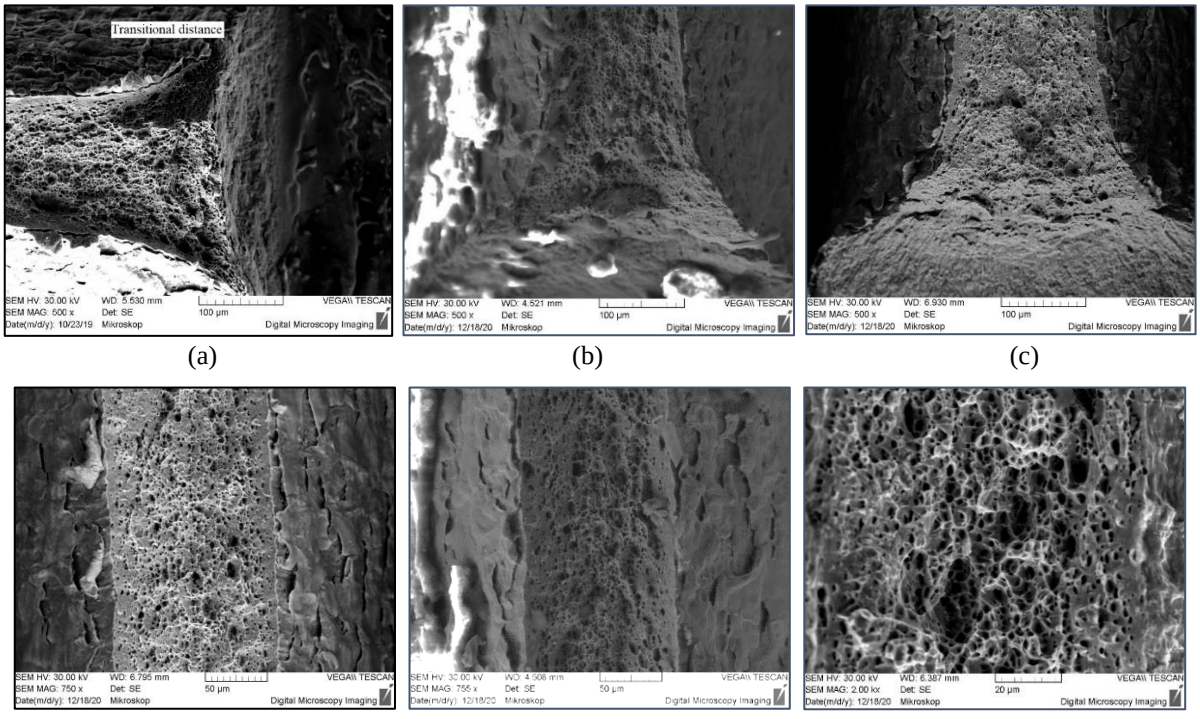

Figure 8.18 Fractured surface at crack tip and center of ligament: (a & d) laser notched; (b & e) EDM notched and; (c & f) precracked samples.

8.3.2 IF steel

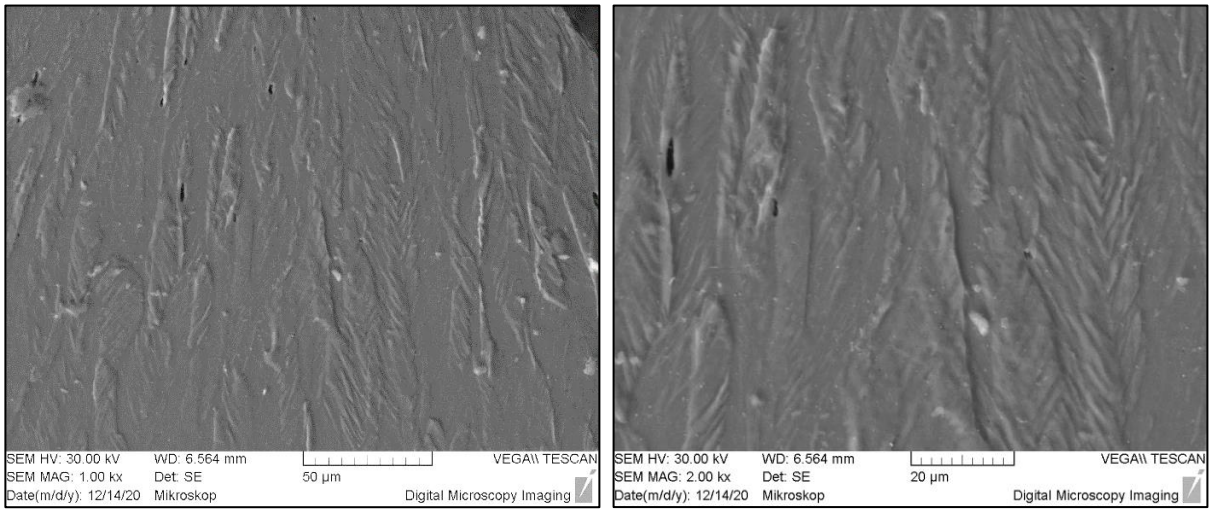

(a) (b)

Figure 8.19 Necking regions in IF steel after EWF test.

Figure 8.19 shows SEM micrographs in the IF steel necking region after the EWF test. Voids formed only at the grain boundary interactions and appeared only close to the fracture surfaces. In the EBSD analysis of the homogeneously deformed portion (away from necking), there were no slip bands, and orientation within the grain is without any abrupt change in orientation. However, in the necking region, during severe plastic deformation close to the fracture surface, slip bands are formed about 45º to the loading axis. These bands act as dislocation walls and restrict void coalescence and further increasing resistance to crack propagation. Few grains have unidirectional slip bands, and others have bidirectional slip bands. Steven Dillien et al.[89] have conducted EBSD analysis on these kinds of slip bands in IF steels and found a sudden change in lattice orientation at these slip bands.

Figure 8.20 shows the fractured surface at the crack tip and center of the ligament for the notched and the precracked IF steel. Unlike the DP450 steel, the necking intensity is very high in the IF steel. In both the conditions (notched and precracked), ductile fracture prevails, and the morphology of the cracked surface is similar. In both conditions, transitional distance is not visible (minimal), and shear-lipped slant fracture is prominent. The absence of the transitional distance in the IF steel can be attributed to high plastic fracture strain. The size of the dimples is larger and inconsistent in comparison to the DP450 steel. Thickness at the edge of the fractured surface is not constant throughout the ligament length. The ratio of the slant to the flat fracture is not constant throughout the ligament.

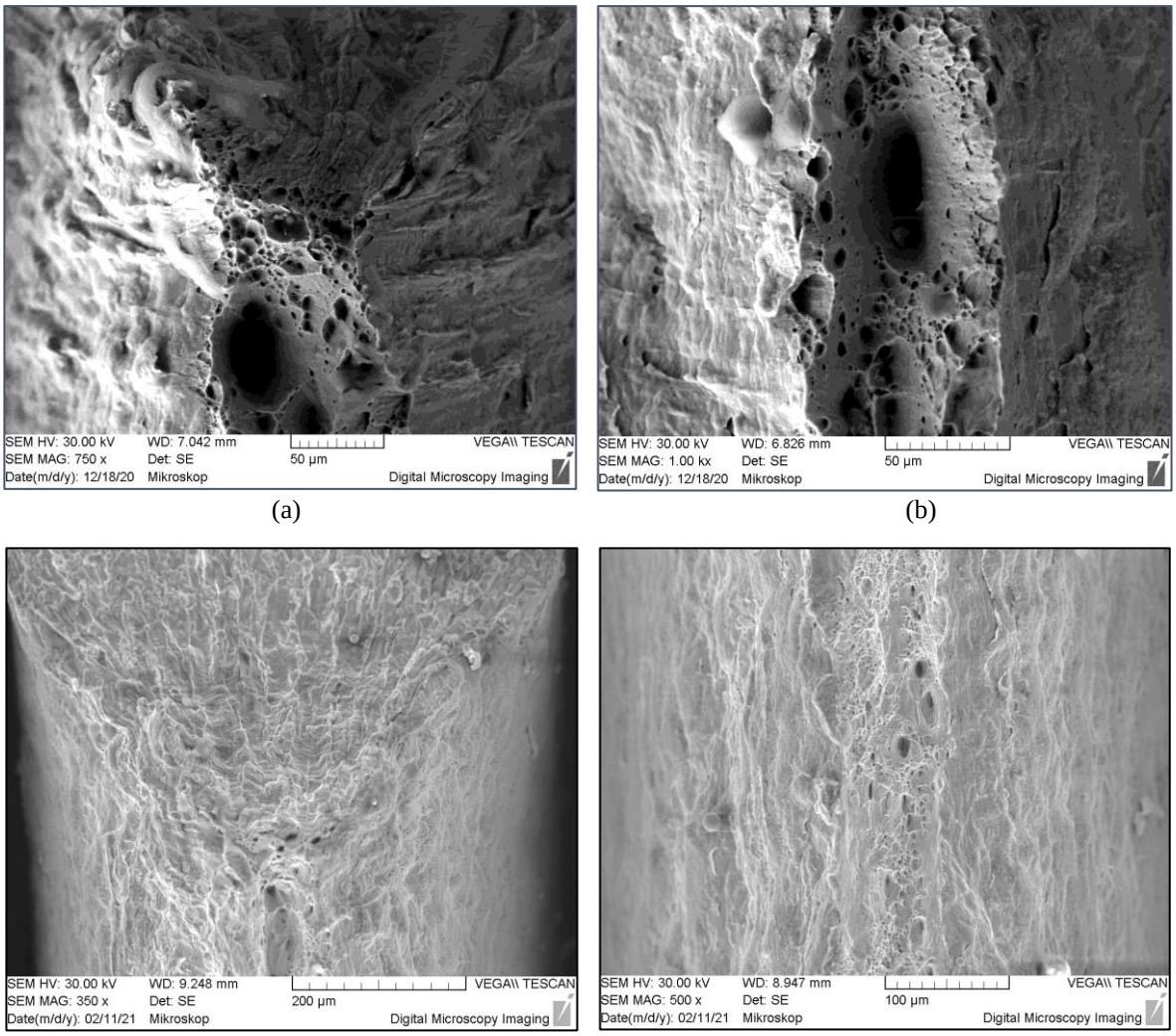

Figure 8.20 Fractured surface at the crack tip and centre of the ligament: (a & b) laser notched and; (c & d) precracked samples.

9. STRAIN ANALYSES DURING EWF TEST

9.1 Strain in EWF test

The objective of digital image correlation (DIC) technology during the EWF test is to find the variation of stresses on the test sample at various stages of loading and pattern of strain distribution. The essential validation criteria for the EWF test is that the ligament must be completely yielded before crack initiation, and plastic deformation should be limited only to the ligament. The validation criteria are also verified using the DIC system. Section 6.4 explains the experimental setup and the sample preparation for the DIC measurements.

9.2.1 DP450 steel

Figure 9.1 shows the force versus deformation diagram of an EWF test and selected points at which strains are analysed. Mises, major and minor strains are analysed at these points with the DIC diagrams' help (Figure 9.2, Figure 9.3 & Figure 9.4).

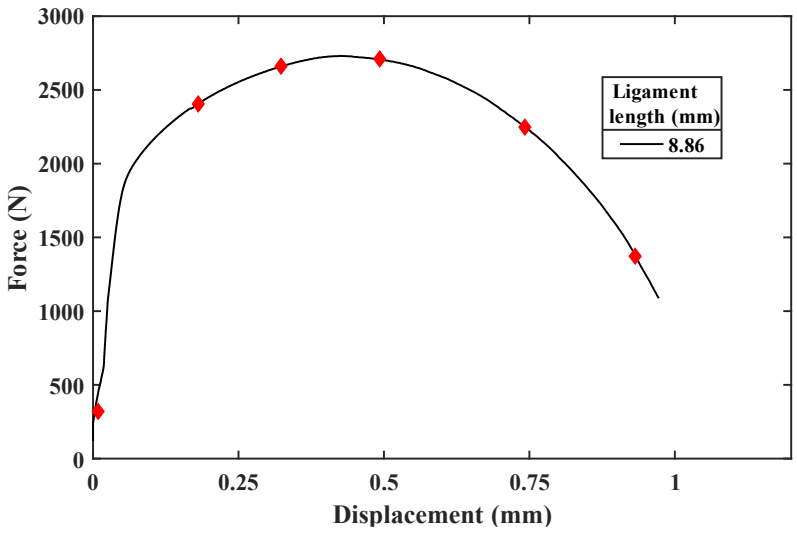

Figure 9.1 Force versus displacement diagram of EWF test of DP450 steel for ligament length 8.86 mm.

Figure 9.2 shows the Mises strain development at various stages (mentioned in Figure 9.1) during the EWF test. From the visual observation, plastic deformation is limited only to the ligament area, and the rest of the sample has no significant plastic deformation. The shape of the plastic zone around the ligament is slightly elliptical. The amount of deformation (strain) within the elliptical plastic zone around the ligament is not uniform. The area around the immediate vicinity of the ligament is called the necking zone and experienced severe deformation. The local strain inside the necking zone is significantly higher than the outer

plastic zone. During the EWF test, after complete yielding, strains near notches are higher than the rest of the ligament. Half dumbbell-shaped strain patterns are created near the notches and intersect during crack propagation. The half dumbbell-shaped strain has a gradient strain pattern, and the strain decreases as it moves away from the notch centre. Stable crack growth happens only after reaching the maximum force. After the maximum force, strain outside the necking zone will not change significantly. The shape of the plastic zone and behaviour of strain is similar for both notched and precracked samples. Figure 9.3 & Figure 9.4 show the major and minor strains at the various stages of the EWF test. The effect of minor strain, predominantly perpendicular to the loading direction, is very little. The major strain, predominantly along the loading direction, is high, and its contribution to Mises-strain is maximum. The inner portion of the ligament has little tension in minor strain direction, while the notches' surrounding has little compression. The large portion of the ligament during the EWF test is in plane strain condition (regarding FLD); hence, the strains can also be used to construct forming limit diagram (FLD) and fracture forming limit diagram (FFLD).

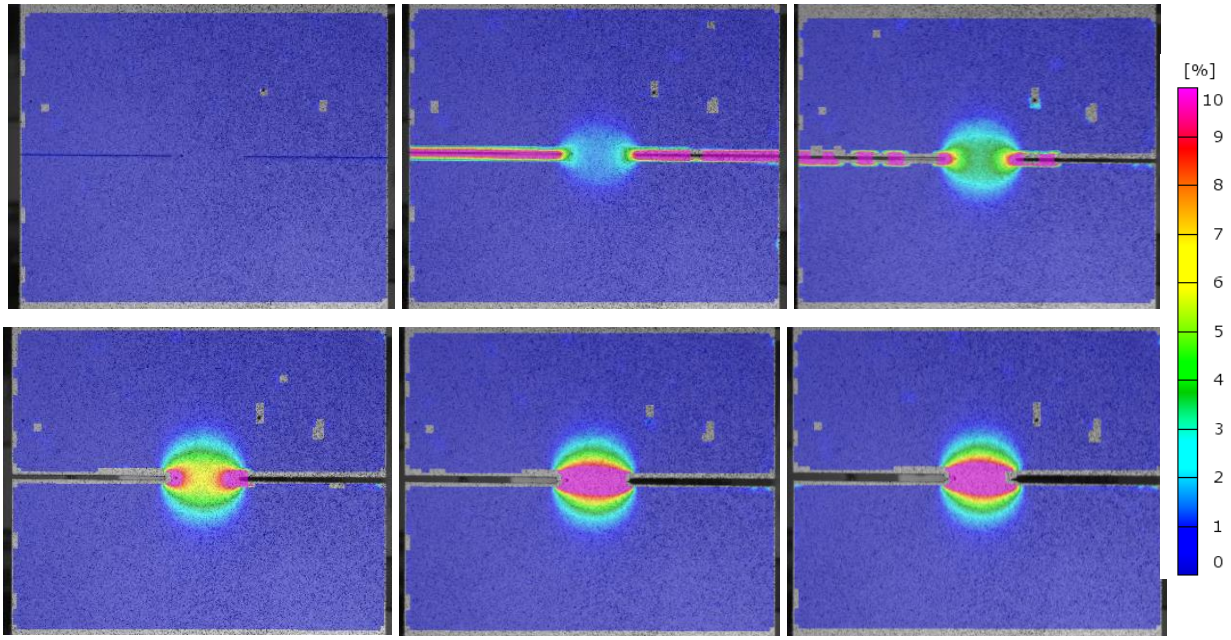

Figure 9.2 Mises strain development during the EWF test at various stages (Figure 9.1).

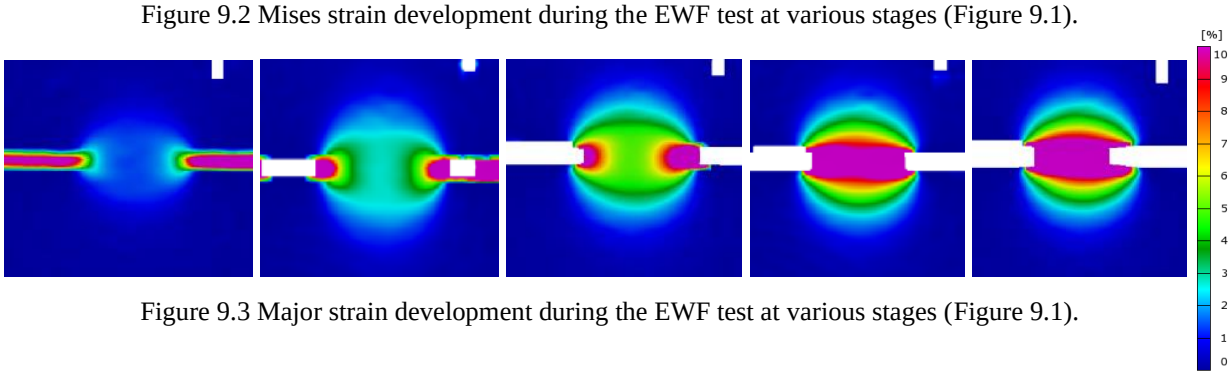

Figure 9.3 Major strain development during the EWF test at various stages (Figure 9.1).

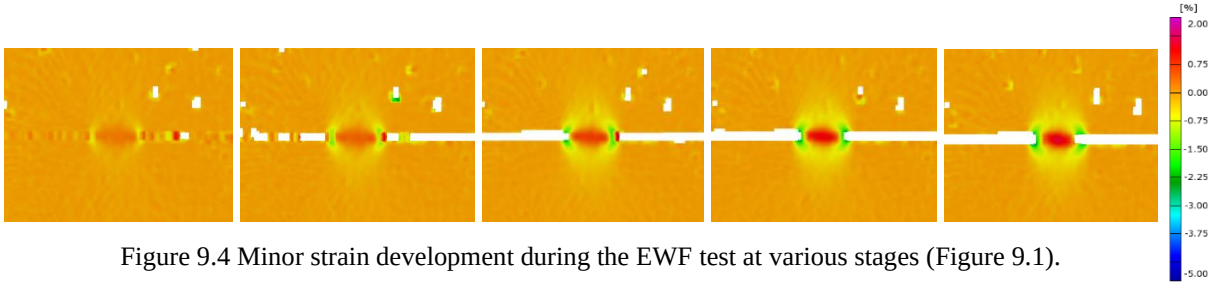

Figure 9.4 Minor strain development during the EWF test at various stages (Figure 9.1).

Figure 9. 5 and Figure 9. 6 show the Mises and minor strain, respectively, for three different sized ligament lengths at the peak load during EWF tests. The shape of the plastic zone in all three different-sized ligaments is similar. As ligament length increases, the shape of the plastic zone around the ligament becomes more elliptical, but the primary shape has not been changed noticeably. A similar strain pattern is present in all the ligaments during the EWF tests.

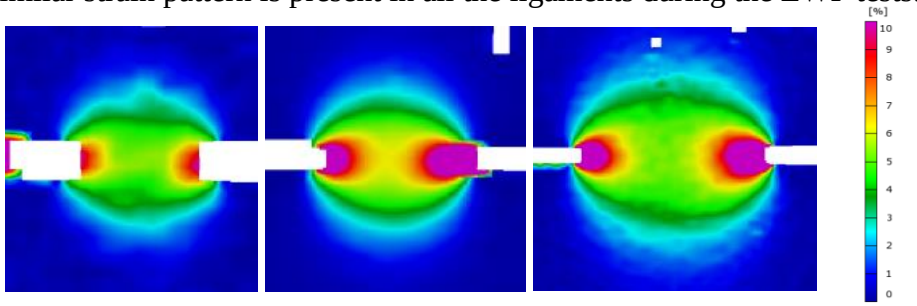

Figure 9. 5 Mises strain for 3.24, 8.86 and 12.74 mm ligament lengths (left to right) near the peak load.

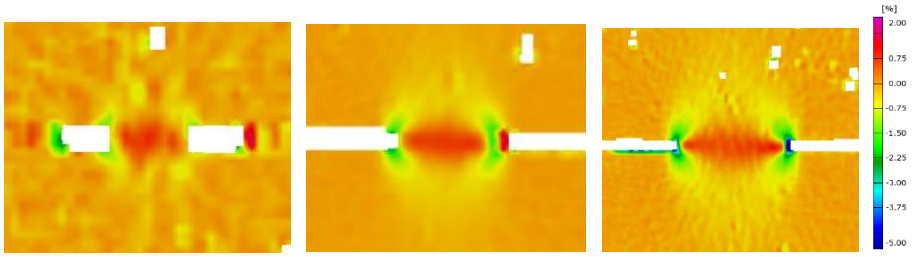

Figure 9. 6 Minor strain for 3.24, 8.86, and 12.74 mm ligament lengths (left to right) near the peak load.

Figure 9.7(a, b & c) shows the Mises, major and minor strain, respectively, for a section drawn perpendicular to the ligament. Figure 9.7(a) shows the position of the section line on the EWF sample. The maximum-recorded Mises strain is around 45%; however, the value is dependent on the last recorded value. The maximum strain (necking) happens over a section length of approximately 3 to 5 mm, mainly in the necking zone. After the initiation of necking, the strain outside the necking zone remains the same, while the narrow necking zone experiences severe strain before the final fracture. The minor strain is negative outside the necking zone and tensile in the necking zone; however, the effect is minimal, and it has no significant impact. The minor strains reach their peak values much before the last recorded values and slightly decrease before the fracture. The sharp reduction of force during the final necking reduces complimentary minor strain before fracture. Figure 9.7(d, e & f) shows the Mises, major and minor strains versus stage time at different stage points. Figure 9.7(d) shows the stage points position on the EWF

test sample. The strains are minimal before yielding, and it is attributed to low elastic strains. The stage points closer to the necking zone experience high strains and gradually decrease as points move away from the fracture zone (necking zone). As stage points move away from the fracture zone, faster they reach strain stagnation before fracture. Stage points 0 and 1 have higher strain in comparison to the rest of the stage points. Until reaching maximum force, the stage points 0 and 1 have identical strains. After reaching the maximum force, stage point 0 started to deviate from stage point 1 and experienced strains several orders higher than stage point 1.

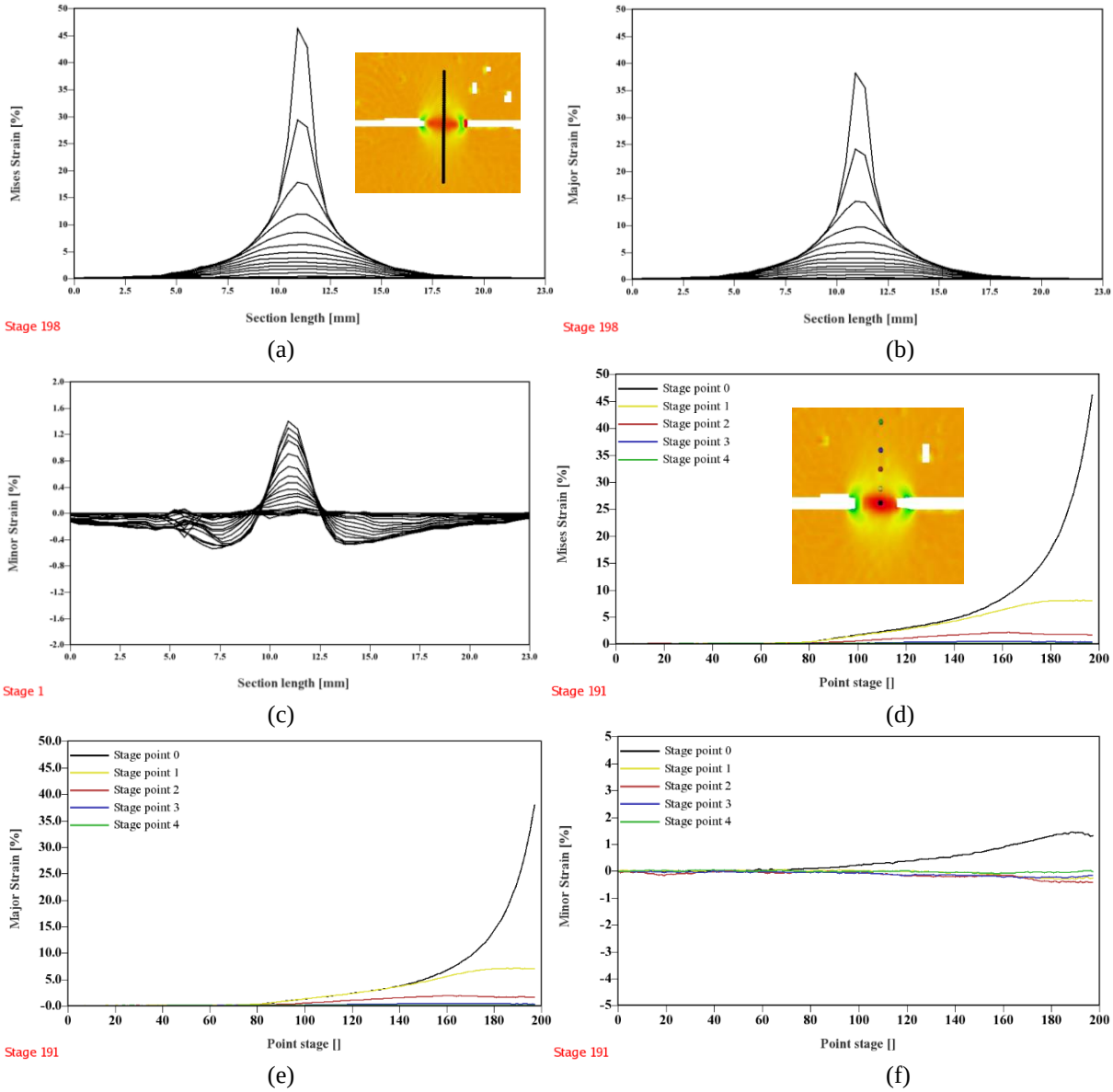

Figure 9.7 Mises, major and minor strains(a, b & c) versus section length (drawn perpendicular to the ligament) at various stages and; Mises, major and minor strains(d, e & f) versus point stage(time) for various stage points(d).

9.2.2 IF STEEL

Figure 9.8 shows the force versus deformation diagram during an EWF test, and various highlighted points at which strains are analysed. Mises, major and minor strains are analysed at these points with DIC diagrams' help (Figure 9.9, Figure 9.10 & Figure 9.11).

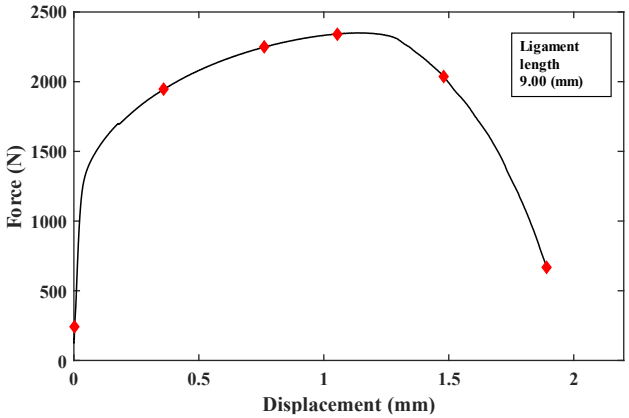

Figure 9.8 Force versus displacement diagram of EWF test of IF steel for ligament length 9 mm.

Figure 9.9 shows the Mises strain development at various stages (mentioned in Figure 9.8) during the EWF test. Like the DP450 steel, plastic deformation is limited to the ligament area, and the rest of the sample is largely unaffected. However, the spread of plasticity is much wider. The shape of the plastic deformation is slightly different in comparison to the DP450 steel. The shape of plastic deformation in the IF steel is also elliptical; however, the major axis (ellipse) is along the loading direction. During the initial loading stages, the shape of the plastic zone around the ligament is more circular. The high strain zone (more than 10%) is much wider for the IF steel than the DP450 steel. The strain gradient rings at the notches are more circular and stretched outside the fracture zone (compared to the DP450). Figure 9.10 & Figure 9.11 show the major and minor strains developed during various stages of the EWF test. Like the DP450 steel, the minor strain is very little, and the centre portion of the ligament is in plane strain condition (minor strain close to zero). The minor compressive strain around the notches is much wider and spreading out of the necking zone. The major strain acting along the loading direction has the dominant effect on the entire strain behaviour.

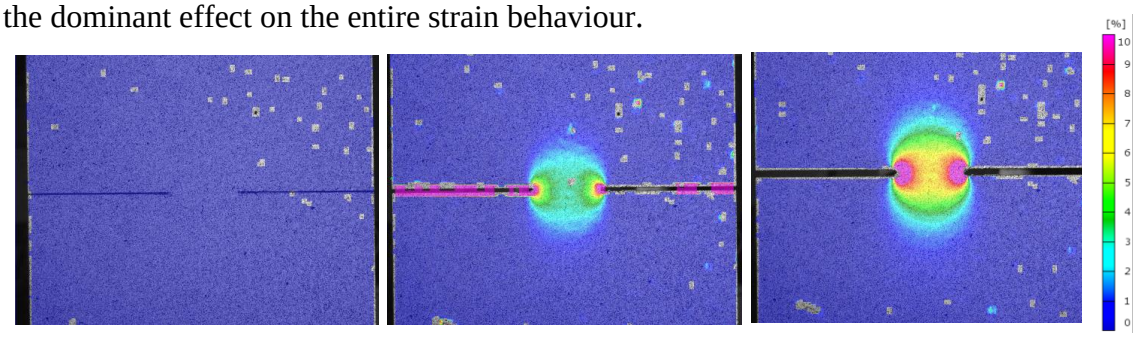

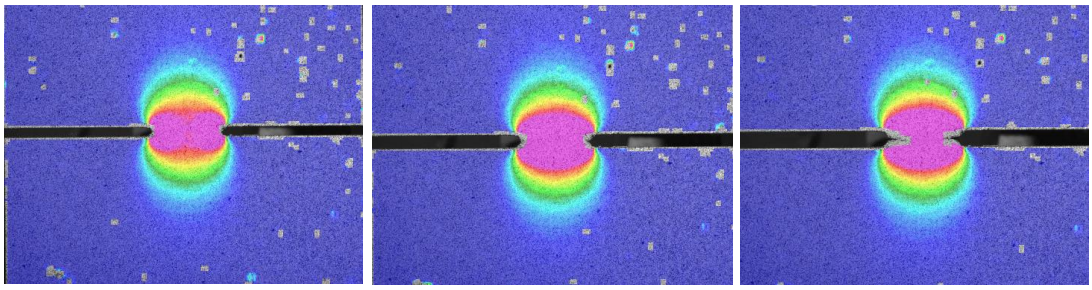

Figure 9.9 Mises strain development during EWF test at various stages (Figure 9.8) for ligament length 9 mm.

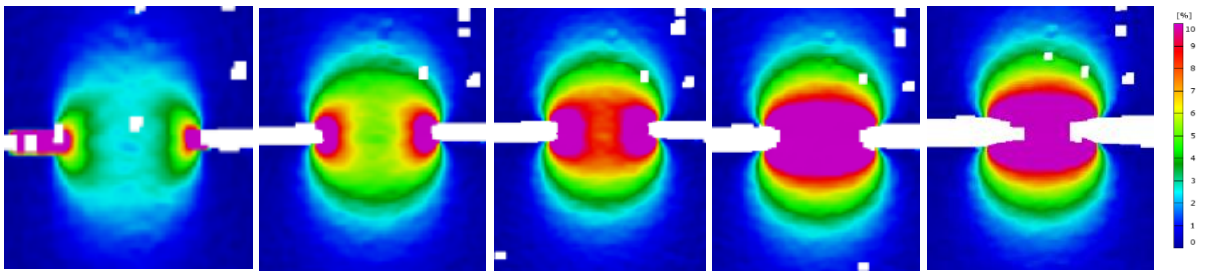

Figure 9.10 Major strain development during EWF test at various stages (Figure 9.8) for ligament length 9 mm.

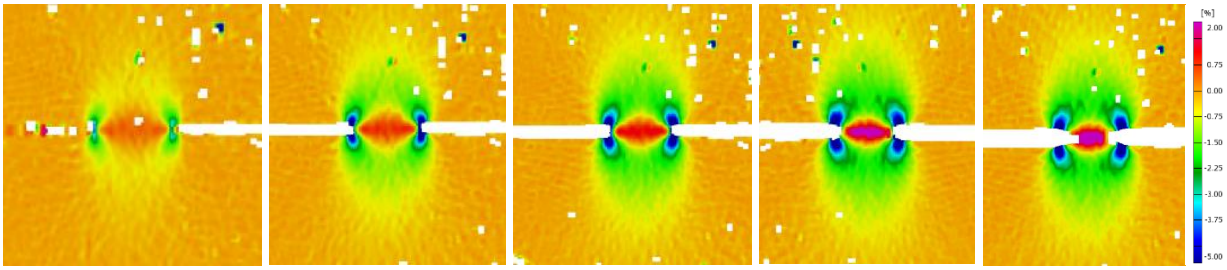

Figure 9.11 Minor strain development during EWF test at various stages (Figure 9.8) for ligament length 9 mm.

Figure 9.12 and Figure 9.13 show Mises strain and minor strain respectively for three ligaments 4.83, 9.0, and 12.77 mm. From visual observation of the mises strain, the shape of the plastic zone around the ligament is similar. The minor strain increases with an increase in ligament length; however, the effect is not significant.

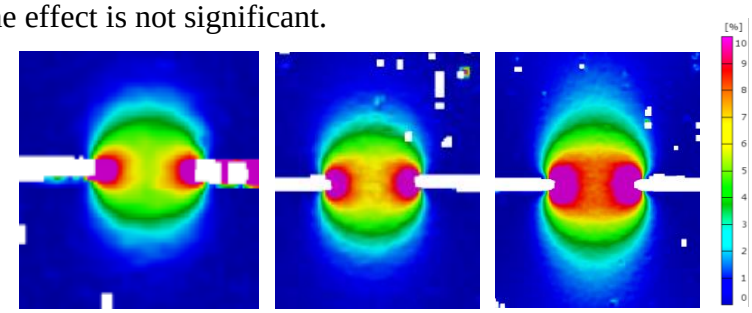

Figure 9.12 Mises strain for 4.83, 9.0, and 12.77 mm ligament length (left to right) near peak load.

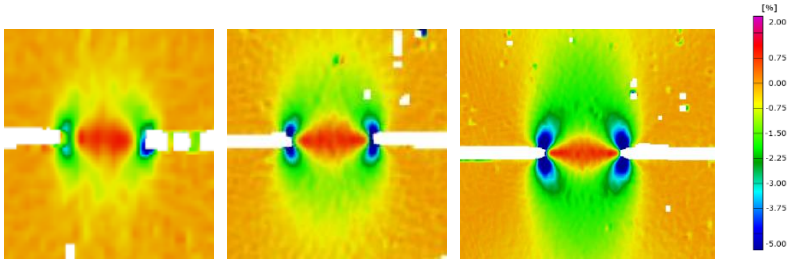

Figure 9.13 Minor strain for 4.83, 9.0, and 12.77 mm ligament length (left to right) near peak load.

Figure 9.14(a, b & c) shows Mises, major and minor strain, respectively, for a section line drawn perpendicular to the ligament. Figure 9.14(a) shows the position of the section line on the EWF sample. The maximum recorded mises strain is about 80%; however, the value is dependent on the last recorded value. The maximum strain (necking) happens over a section length of approximately 4 to 6 mm, mainly in the necking zone; it is larger than the DP450 steel. The maximum strain in the IF steel is almost twice that of the DP450 steel. Figure 9.14 (d, e & f) shows Mises, major and minor strains versus stage time for different stage points. Figure 9.14(d) shows the stage points position on the EWF test sample. The behaviour of strain development is similar to that of the DP450 steel, which was explained in the previous section.

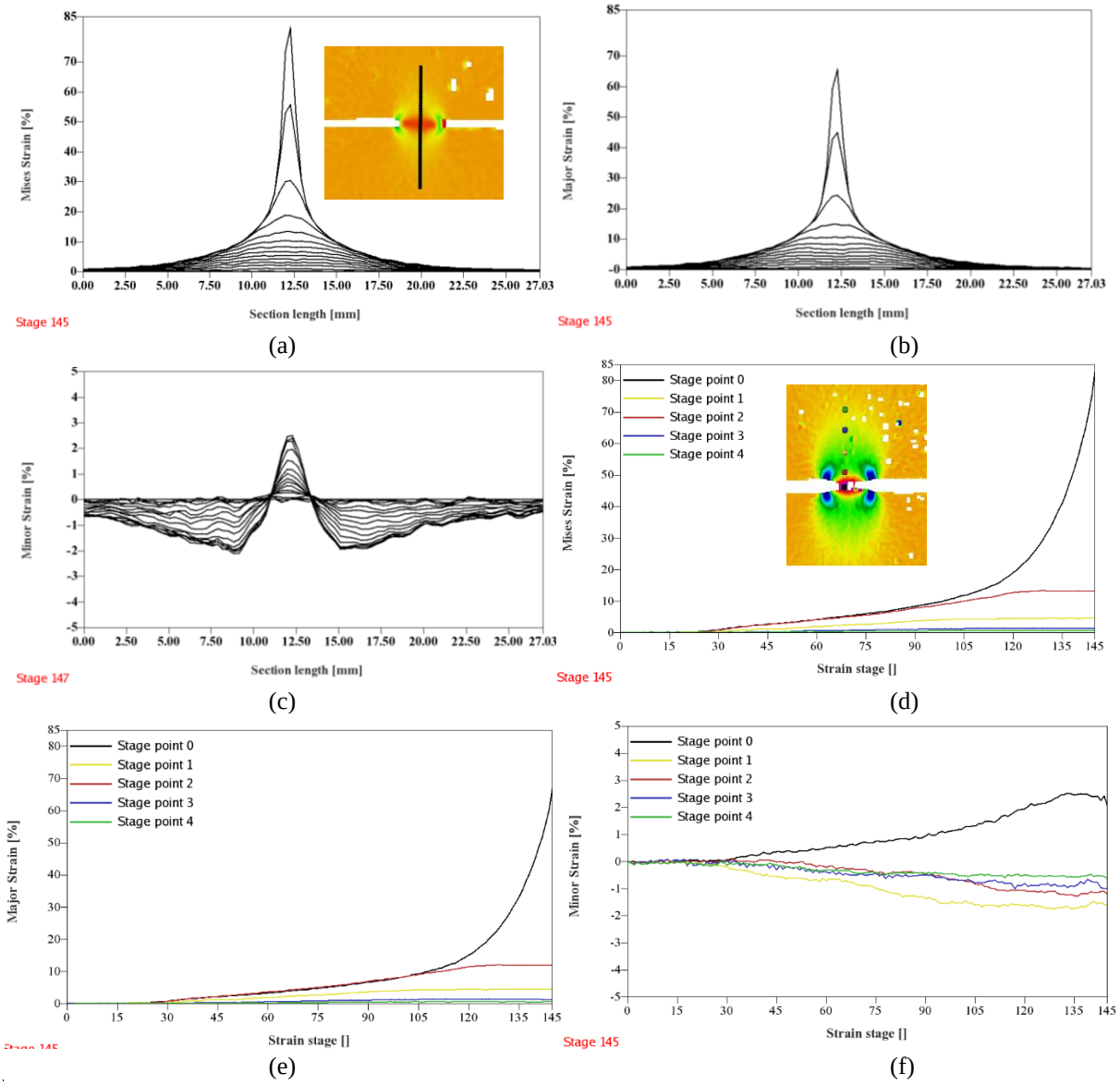

Figure 9.14 Mises, major and minor strains (a, b & c) versus section length (drawn perpendicular to the ligament) at various stages and Mises, major and minor strains (d, e & f) versus point stage (time) for various stage points(d).

9.2 Fracture forming diagrams

Figure 9.16 and Figure 9.16 show major and minor strain development (at the centre of a ligament) during EWF test for mode 1, mode-2, and mixed-mode (30º) samples of the DP450 steel (Figure 9.16) and the IF steel (Figure 9.16). The strain data is obtained using digital image correlation, and the data is collected at the centre of the ligament. The fundamental pattern of the major and the minor strain development for both the steels is almost similar. In mode-1 of the EWF test, the minor strain for the DP450 steel is slightly lower than the IF steel, and the major strain difference between the two steels at fracture is little compared to the other two modes. However, the value of major strain at the fracture is calculated using final thickness. A near plane-strain condition is present in mode-1 of EWF tests. In mode-2, both the major and the minor strains increase linearly, and the path is about 45º(slope of -1) to the minor strain baseline. In mixed-mode (30º), the strain path lies in between mode-1 and mode-2.

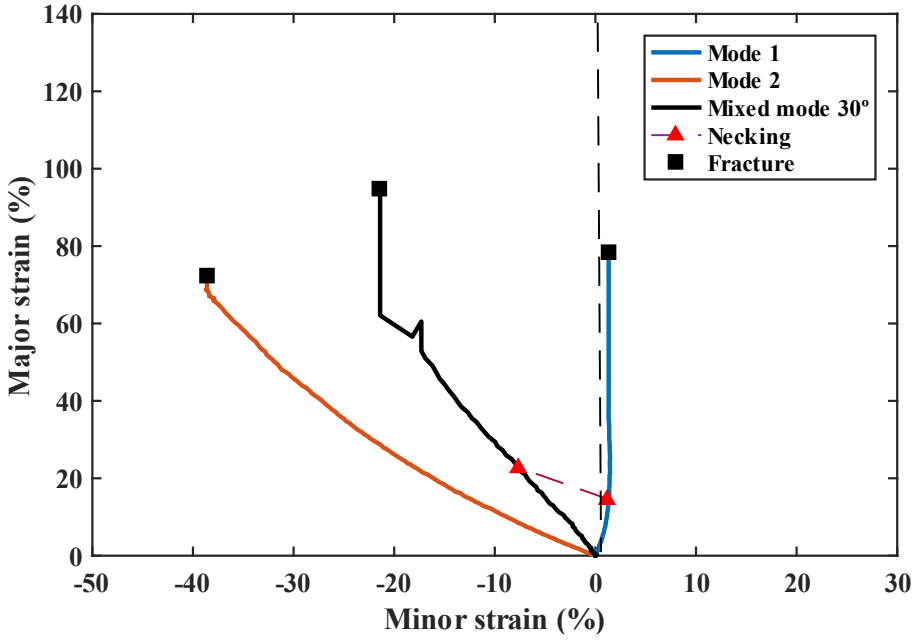

Figure 9.15 Major and minor strain development during EWF test for mode-1, mode-2, and mixed-mode of the DP450 steel.

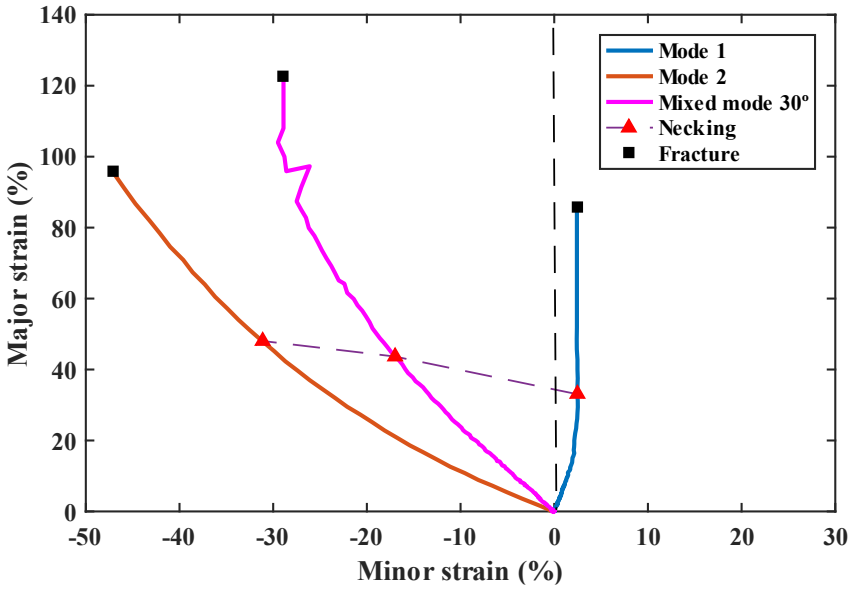

Figure 9.16: Major and minor strain development during EWF test for mode-1, mode-2, and mixed-mode of the IF steel.

Figure 9. 17(a) shows the time-dependent method used by M.B. Silva et al. [101] to determine the stage of necking. At three different points, strain data is collected (Figure 9. 17(a)). Point 1 is inside the fracture zone, point 2 is on the instability region boundary, and point 3 is outside the local instability zone. The stage at which the local major strain rate of point 2 reaches its maximum value is identified as the necking stage. The major and the minor strains of point 1 at the necking stage are considered to calculate local instability or necking. Figure 9. 17(b) shows the necking and fracture points of the DP450 and the IF steel in all EWF test modes. The major strain at fracture is calculated by the following method: the strain across thickness ε_3 is calculated from the final thickness of the sample after the test (measured in SEM microscope). The minor strain at fracture is assumed to be the same as the last recorded value. Later, the major strain at fracture is calculated from the incompressibility hypothesis ($\varepsilon_1=-(\varepsilon_2+\varepsilon_3)$).

For the IF steel, the major strain at fracture is significantly higher than the DP450 steel in all the modes. The major strain at necking is also higher for the IF steel. In mode-2 of the DP450 steel, necking was not properly visible. The difference between fracture strains of the IF and the DP steels is highest for mode-2 and lowest for mode-1. The major strains at fracture of the IF steel are 7.62%, 23.41%, and 27.70% higher than the DP450 steel in mode 1, mixed-mode, and mode-2, respectively. The major strains at necking (local instability) of the IF steel are 125.52% and 91.07% higher than the DP450 steel in mode-1 and mixed-mode, respectively.

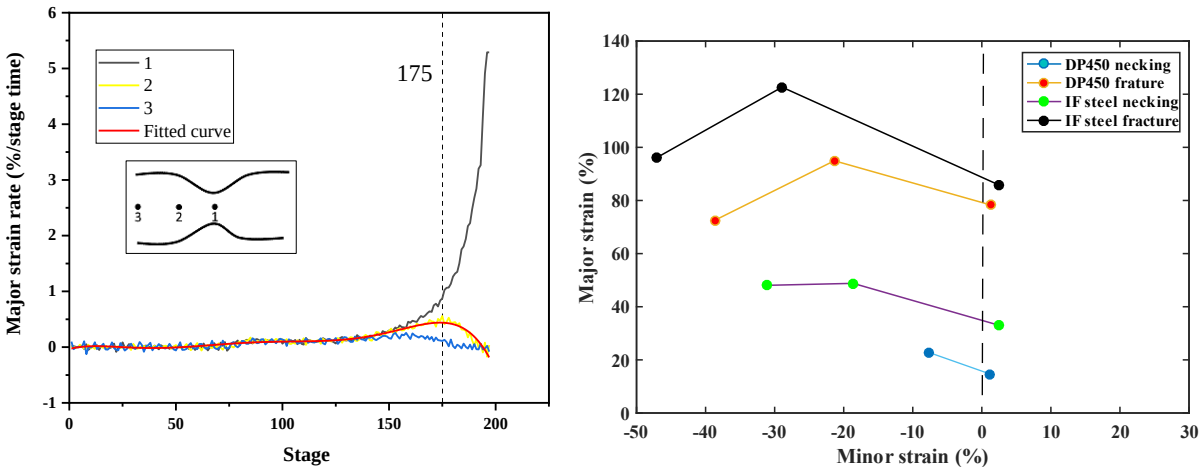

Figure 9. 17 (a) Time-dependent methodology to determine the necking stage; (b) Necking and fracture points for DP450 and IF steel in all tested modes.

Figure 9.18 shows Forming limit diagram (FLD) of the DP450 steel and the IF steel determined from the Nakajima test. Section 6.6 explains the detail of the experimental procedure of the Nakajima test. The test is conducted according to the ISO 12004-2, and necking is determined using the section-based method (DIC). From the FLC analyses of the IF and the DP450 steels, the necking strain for the IF steel is significantly higher than the DP450 steel. For the smallest width sample in the Nakajima test (close to uniaxial tension condition), at necking, the IF steel has major and minor strains 85.07% and 244.15% higher than that of the DP450 steel. For near-plane-strain conditions (minor strain close to zero), the IF steel has a major strain of 75.12% higher than that of the DP450 steel. For equi-biaxial tension condition (maximum width sample), the IF steel has the major and minor strains 24.73% and 19.46% higher than that of the DP450 steel. The difference of necking strain between the IF and the DP450 steel is maximum in the tension-compression zone. It reduces as it moves towards the plane strain condition and further reduced to the lowest difference at equi-biaxial conditions.

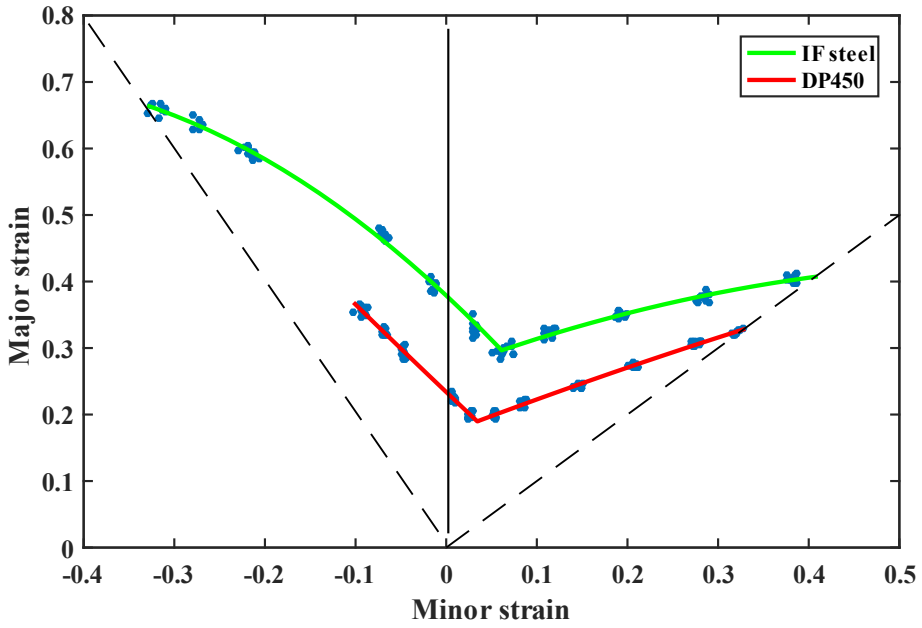

Figure 9.18 Forming limit diagram (FLD) of DP450 steel and IF steel determined from the Nakajima test.

9.2.1 Fracture strain and triaxiality

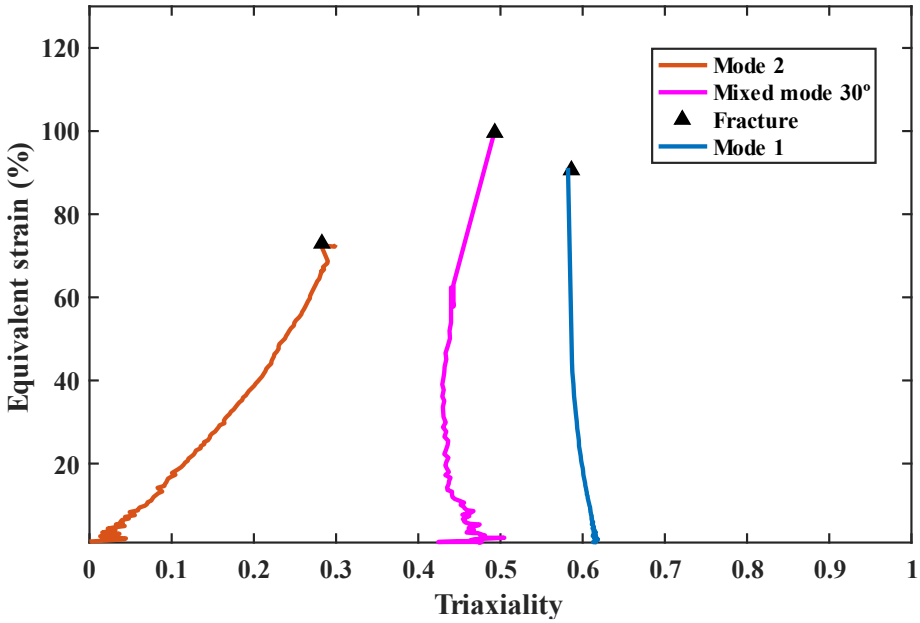

Figure 9.19 Equivalent strain versus triaxiality for mode-1, mode-2, and mixed-mode (30º) EWF test of DP450

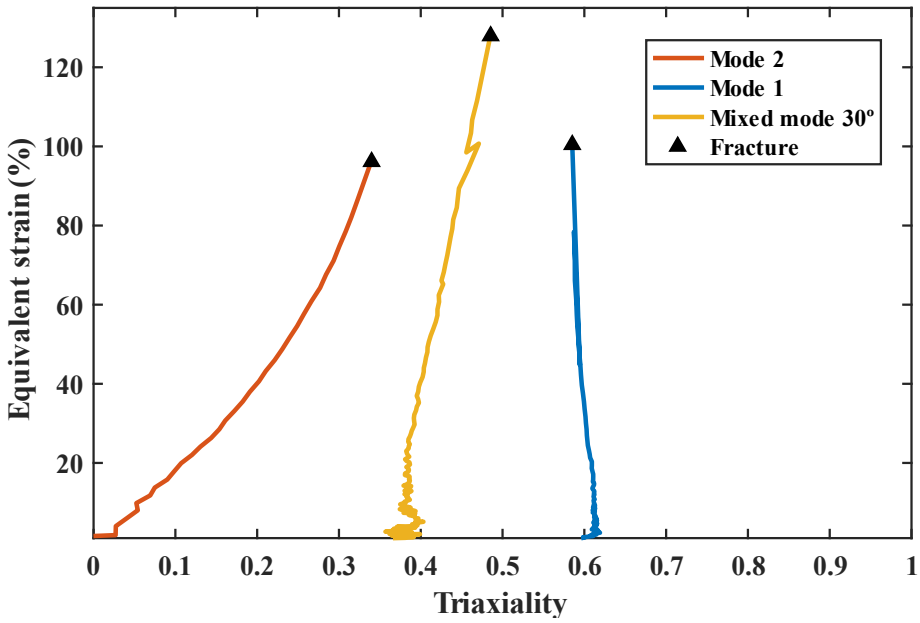

Figure 9.20 Equivalent strain versus triaxiality for mode-1, mode-2, and mixed-mode (30º) EWF test of IF steel.

Section 5.3 explains the calculation of triaxiality and equivalent strain from major and minor strains determined through the digital image correlation technique. Figure 9.19 and Figure 9.20 show the equivalent strain versus triaxiality for the DP450 and the IF steels, and the strain data are collected from three different modes of EWF tests. The equivalent strain and the triaxiality are calculated based on surface data, and actual values at the centre will be different; hence, the comparison is limited only to the surface. The strain data are collected close to fracture, which means at maximum localised strain portion. The theoretical value of triaxiality for shear mode (Mode-2) and plane strain condition (Mode-1) is zero and 0.58, respectively. In all three modes, the equivalent strain at fracture for the IF steel is significantly higher than the DP450 steel. In the mode-1 EWF test, a near plane strain condition is present (Figure 9.16), and the triaxiality is close to the theoretical value. In the plane strain condition (mode-1), the difference between equivalent strains at fracture for the IF and the DP450 is little compared to other modes. In the mixed-mode (30º), the triaxiality is slightly lower than the mode-1, and the equivalent strain is higher than the mode-1. The low triaxiality in the mixed-mode (comparing to mode-1) helps in higher ductility and fracture strain. Initial triaxiality patterns are slightly different for the IF and the DP450 steel; however, at fracture, they are identical. In the shear mode (mode-2), the initial value of triaxiality is close to the theoretical value of zero; however, it increases linearly with loading.

9.3 Hole expansion test

Table 9.1 and Table 9.2 show the hole expansion test results for the DP450 and IF steels. The original diameter of the hole is 35 mm for both the steels. Section 6.6 explains the details of the hole expansion test. Cutting clearance is the gap between punch and die; it is also expressed in the sheet thickness percentage. The hole expansion ratio of the IF steel is significantly higher than the DP450 steel. At zero clearance, the hole expansion ratio of the DP450 and IF steels are 63.14 and 185.57 percentages respectively. The hole expansion ratio of the IF steel is about three times higher than the DP450 steel. With a maximum clearance of 0.4 mm, the hole expansion ratio of the DP450 and IF steels are 9.96 and 63.75 percentages respectively. The hole expansion ratio of the IF steel is about six times higher than that of the DP450 steel.

Table 9.1 Hole expansion test results of DP450 steel.

Final average diameter d_f (mm)	**Hole expansion ratio λ (%)**	**Cutting clearance *C* (mm)**	**Cutting clearance in % of thickness *C(%t)***
57.10	63.14	0	0
47.67	36.21	0.01	1.769
42.61	21.75	0.08	14.15
39.80	13.71	0.16	28.31
39.47	12.78	0.24	42.47
38.61	10.32	0.32	56.63
38.48	9.964	0.4	70.79

Table 9.2 Hole expansion test results of IF steel.

Final average diameter d_f (mm)	**Hole expansion ratio λ (%)**	**Cutting clearance *C* (mm)**	**Cutting clearance in % of thickness *C(%t)***
99.95	185.57	0	0
85.41	144.03	0.01	1.459
78.01	122.89	0.08	11.67
75.95	117.00	0.16	23.35
65.77	87.92	0.24	35.03
62.06	77.32	0.32	46.71
57.31	63.75	0.40	58.39

Figure 9.21 shows the hole expansion ratio λ versus cutting clearance in terms of thickness (percentage) for the DP450 and IF steel. The hole expansion ratio decreases with an increase in cutting clearance, irrespective of the material. In the case of the IF steel, the hole expansion ratio decreases almost linearly with an increase in the cutting clearance; however, the drop is slightly higher in the beginning. In the case of the DP450 steel, the drop in hole expansion with

an increase in cutting clearance is significant at the beginning and very little after the initial drop. The hole expansion ratio's sensitivity to the cutting clearance is high at the beginning for the DP450 steel, and for the IF steel, it varies gradually throughout the band.

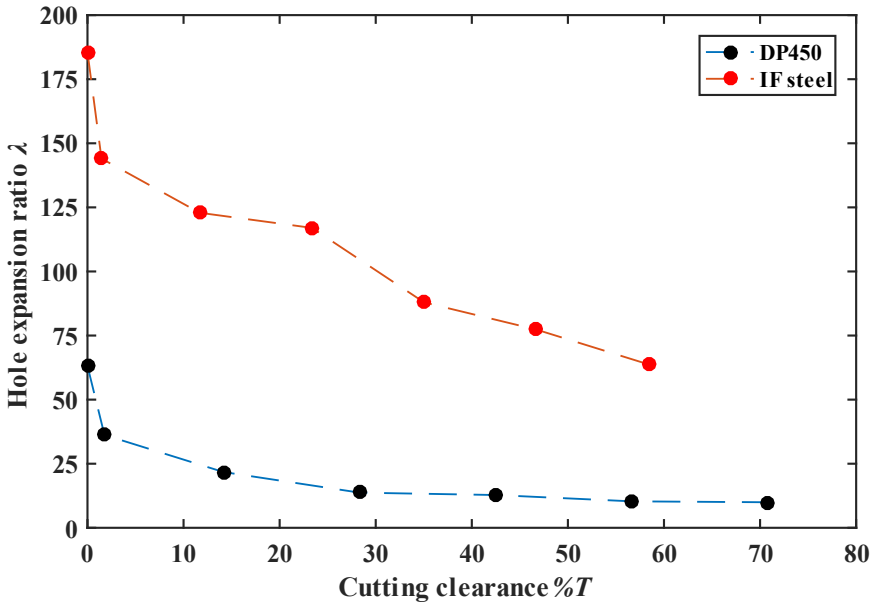

Figure 9.21 Hole expansion ratio λ versus cutting clearance for DP450 and IF steel.

9.4 Comparison of EWF test with rest of the experiments

For the precracked samples, the DP450 and the IF steel have w_e values of 154.22 kJ/m^2 and 196.16 kJ/m^2, respectively. The IF steel has about **27%** higher w_e value than the DP450 steel. Crack tip-opening displacement δ_c^e for the DP450 and the IF steels are 0.3251 and 0.4260 mm, respectively, for the precracked samples. For the precracked samples, the IF steel has about **31%** higher δ_c^e value than the DP450 steel. At zero clearance, the hole expansion ratio of the DP450 and IF steels are 63.14 and 185.57 percentages respectively. The hole expansion ratio of the IF steel is **190.88%** higher than that of the DP450 steel. In the Nakajima test, at necking, for the near plane strain condition, the IF steel has a major strain of **75.12%** higher than that of the DP450 steel.

From analyses of the above results, the IF steel has better fracture toughness (EWF test), higher resistance to local instability (necking), and a better hole expansion ratio than the DP450 steel. In the EWF test, both elongation (strain) and force (stress) are the deciding factors for the results (w_e and δ_c^e). In the Nakajima test and FLD diagram, elongation (strain) is the only deciding factor for the result, and force data is not considered. In the Nakajima test and FLD test, the difference between the IF steel and the DP450 steel is significantly higher. While in the EWF test, the difference in result between the IF steel and the DP450 steel is mediocre. The high load-bearing capacity of the DP450 steel helps in decent fracture response in the EWF test. However, due to the poor elongation characteristics and low resistance to local instability, the DP450 steel has a low hole expansion ratio and poor FLD characteristics compared to the IF steel.

10. CONCLUSION AND FUTURE WORK

Essential work of fracture (EWF) methodology has been studied, and parameters affecting the results are analysed in detail. The EWF method has been successfully used to calculate the fracture toughness of the DP450 steel and the IF steel. The EWF method can be used to characterise the strength and fracture toughness of advanced high-strength steels. This methodology helps in the selection of high-toughness and crash-resistant materials. However, the EWF methodology is sensitive to many parameters. The major parameters affecting the EWF methodology are notch tip radius (fatigue pre-crack), sample preparation method, material property, selection of ligament length, choice of the lowest ligament length, and length of fatigue crack (*a/W* ratio). For the notched samples, the number of samples required to get accurate results is low (5 to 7). However, for precracked samples, a higher number of samples need to be tested for accurate results (more than 10). The sample preparation method influences the notch tip geometry and the results. However, for precracked samples, the influence of the sample preparation method is very low. The sample prepared from the EDM method is better than the laser cutting because it does not significantly change the material properties near the notch tip. However, the laser cutting produces a sharper notch tip, and the HAZ is offset by fatigue precrack. Both notched and precracked samples can be used in the EWF methodology. The notched samples are suitable for quick and easy comparison. However, only precracked samples represent the actual fracture toughness values. Low toughness and high strength materials like advanced high strength steels are more sensitive to notch tip radius. In contrast, high toughness materials are less sensitive to the notch tip radius. However, not all materials are equally sensitive to the notch tip radius.

Following conclusions can be made from the EWF tests, EBSD analyses, Fractographic analysis, FLD tests, hole expansion test of the IF steel and the DP450 steel.

- For the precracked samples, the DP450 and the IF steels have w_e values of 154.22 kJ/m^2 and 196.16 kJ/m^2, respectively. The IF steel has about **27%** higher w_e value than the DP450 steel.
- The presence of fatigue precrack in the DP450 steel has reduced w_e by about 23%, while only 8% for the IF steel.

- For the precracked samples, crack tip-opening displacement δ_c^e for the DP450 and the IF steels are 0.3251 and 0.4260 mm, respectively. For the precracked samples, the IF steel has about **31%** higher δ_c^e value than the DP450 steel.
- For the precracked samples, ψ^e for the DP450 and the IF steels are 9.07º and 19.76º, respectively.
- The average grain sizes are 6.31 µm and 15.35 µm for the DP450 and IF steels, respectively (considering only the grains larger than 100 pixels and without martensite for the DP450 steel).
- In the IF steel, a favourable {111} crystal orientation in the normal direction helps for excellent plastic deformation; however, the DP450 steel lack a favourable {111} texture in the normal direction.
- Both the DP450 steel and the IF steel have local misorientation in as-received condition. In the IF steel, local misorientation is concentrated mainly in small grains and around LAGB. In the DP450 steel, the local misorientation is primarily concentrated around martensite and grain boundaries.
- During plastic deformation, both the DP450 steel and the IF steel experience heterogeneous deformation within the ferrite grain. However, the extent of heterogeneous deformation is less in IF steel.
- Primary mode void generation in the DP450 steel is ferrite-martensite decohesion, and voids appeared in between two small martensite grains separated by a short distance. In the IF steel, voids formed only at grain boundary interactions.
- The size of the plastic zone during the EWF test is significantly larger for the IF steel than the DP450 steel (DIC analyses). The IF steel can redistribute the stress much away from the crack tip.
- At zero clearance, the hole expansion ratio of the DP450 and the IF steels are 63.14 and 185.57 percentages respectively.
- In the FLD, for the near plane-strain condition, the IF steel has a major strain of **75.12%** higher than that of the DP450 steel.
- The IF steel has excellent necking characteristics, high elongation at fracture, good fracture toughness, better hole expansion ratio, and a favourable crystallographic orientation for better forming. The DP450 steel has decent fracture toughness, poor hole expansion ratio, poor necking characteristics, reasonable elongation at fracture, and high strength.

- In automotive body stamping, the IF steel has an edge in parts where the deep drawing (high-intensity forming) is necessary. However, the DP450 steel is still a good option for the parts, which do not require high-intensity forming but need high strength.

Future work

The essential work of fracture (EWF) technique is yet to be standardized. The methodology has great scope in industry and research applications. In the future, the author like to compare the EWF results with standard fracture toughness parameters like J-integral. Materials having different toughness will be tested in the EWF methodology, and their behaviour will be studied.

APPENDICES

Appendix A1

E.Q. Clutton[34] conducted round-robin experiments on the EWF method and parameters affecting the EWF method. Appendix A.1 shows the parameters and results of the first set of samples. The first set of Ethylene propylene polymer samples of 100 µm thickness was prepared by a single group, i.e., similar specimen dimensional parameter. Appendix A.2 shows the parameters and results of the second set. In the second set, individual groups prepared the samples.

Appendix A.1 Essential work of fracture test results of samples prepared by single group.[34]

Group	h (mm)	W (mm)	L_{max}-L_{min}	samples	Test speed (mm/min)	σ_y (MPa)	w_e (kJ/m^2)	βw_p	σ_{max} (MPa)	S (kJ/m^2)	R^2
1	50	28	6.55–15.07	25	10	27.7	36.8	10.7	29.0	3.5	0.980
2	50	28	6.46–14.29	25	10	28.6	44.2	10.8	29.8	2.8	0.987
3	80	28	6.33–14.17	25	16	27.0	40.0	10.7	30.5	2.0	0.993
4	35	28	6.29–14.15	20	10	27.5	44.9	10.7	29.5	2.8	0.991
5	35	28	6.23–14.15	25	10	27.5	44.6	11.3	29.3	2.1	0.993
6	50	28	6.31–14.14	22	10	27.0	42.9	11.6	30.1	2.9	0.987
7	50	28	6.31–14.15	25	10	26.8	52.8	10.22	28.0	3.9	0.971
8	70	28	6.20–14.35	25	20	-	48.0	10.88	32.0	4.4	0.980

Appendix A.2 Essential work of fracture test results of samples prepared by individual group.[34]

Group	h (mm)	W (mm)	L_{max}-L_{min}	samples	Test speed (mm/min)	σ_y (MPa)	w_e (kJ/m^2)	βw_p	σ_{max} (MPa)	S (kJ/m^2)	R^2
1	60	40	5.86–14.46	27	12	27.7	36.4	10.4	30.6	4.3	0.966
2	60	40	5.76–14.03	25	12	28.6	54.1	09.0	31.6	3.4	0.973
3	80	28	6.13–14.24	27	16	27.0	30.0	11.0	30.0	1.5	0.996
4	35	35	5.24–15.68	20	10	27.5	36.1	11.6	29.2	2.8	0.991
5	35	35	5.78–14.97	12	10	27.5	37.0	11.4	30.2	3.9	0.991
6	50	28	6.31–14.14	22	10	27.0	42.9	11.6	30.8	2.9	0.997
7	50	28	6.45–13.98	27	10	26.8	37.9	11.2	28.4	5.6	0.952
8	70	35	5.95–13.70	25	20	-	27.0	12.0	31.0	4.2	0.974

REFERENCE

1. Fekete, J. R.; Hall, J. N. Design of Auto Body: Materials Perspective. In *Automotive Steels: Design, Metallurgy, Processing and Applications*; Elsevier Inc., 2017; pp 1–18. https://doi.org/10.1016/B978-0-08-100638-2.00001-8.
2. Hall, J. N.; Fekete, J. R. Steels for Auto Bodies: A General Overview. In *Automotive Steels: Design, Metallurgy, Processing and Applications*; Elsevier Inc., 2017; pp 19–45. https://doi.org/10.1016/B978-0-08-100638-2.00002-X.
3. Ghosh, P.; Ray, R. K. Deep Drawable Steels. In *Automotive Steels: Design, Metallurgy, Processing and Applications*; Elsevier Inc., 2016; pp 113–143. https://doi.org/10.1016/B978-0-08-100638-2.00005-5.
4. Pereloma, E.; Timokhina, I. Bake Hardening of Automotive Steels. In *Automotive Steels: Design, Metallurgy, Processing and Applications*; Elsevier Inc., 2017; pp 259–288. https://doi.org/10.1016/B978-0-08-100638-2.00009-2.
5. Garcia, C. I. High Strength Low Alloyed (HSLA) Steels. In *Automotive Steels: Design, Metallurgy, Processing and Applications*; Elsevier Inc., 2016; pp 145–167. https://doi.org/10.1016/B978-0-08-100638-2.00006-7.
6. Fonstein, N. Dual-Phase Steels. In *Automotive Steels: Design, Metallurgy, Processing and Applications*; Elsevier Inc., 2016; pp 169–216. https://doi.org/10.1016/B978-0-08-100638-2.00007-9.
7. Keeler, S.; Kimchi, M.; Mooney, P. J. *Advanced High-Strength Steels Application Guidelines Version 6.0*; Belgium, 2017.
8. Morgans, S. *Advanced High- Advanced High-Strength Steel Technologies in the 2013 Strength Steel Technologies in the 2013 Ford Fusion*; Detroit, 2012.
9. Hall, J. N.; Coryell, J.; Wendt, B.; Adamski, D. Case Studies of Edge Fracture of Dual Phase Steel Stampings. *SAE International Journal of Materials and Manufacturing* **2015**, *8* (3), 783–788.
10. ASTM E399. *Standard Test Method for Linear-Elastic Plane-Strain Fracture Toughness of Metallic Materials*; American Society for Testing and Materials.
11. ASTME1820. *Standard Test Method for Measurement of Fracture Toughness*; American Society for Testing and Materials.
12. ASTM E561. *Standard Test Method for KR Curve Determination*; American Society for Testing and Materials.
13. T. L. Anderson. *Fracture Mechanics Fundamentals and Applications*, Fourth.; CRC Press, Taylor & Francis Group, 2017.
14. INGLIS; CE. Stresses in a Plate Due to the Presence of Cracks and Sharp Corners. *SPIE Milestone Series* **1913**, *137*, 317.
15. Griffits, A. A. The Phenomena of Rupture and Flow in Solids. *Philosophical Transactions of the Royal Society of London. Series A, Containing Papers of a Mathematical or Physical Character* **1921**, *221* (582–593), 163–198. https://doi.org/10.1098/rsta.1921.0006.
16. Rice, J. R. A Path Independent Integral and the Approximate Analysis of Strain Concentration by Notches and Cracks. *Journal of Applied Mechanics, Transactions ASME* **1964**, *35* (2), 379–388. https://doi.org/10.1115/1.3601206.
17. Lanning, W. R.; Javaid, S. S.; Muhlstein, C. L. Reconciling Fracture Toughness Parameter Contradictions in Thin Ductile Metal Sheets. *Fatigue & Fracture of Engineering Materials & Structures* **2017**, *40* (11), 1809–1824. https://doi.org/10.1111/ffe.12600.

18. Broberg, K. B. Critical Review of Some Theories in Fracture Mechanics. *International Journal of Fracture Mechanics* **1968**, *4* (1), 11–19. https://doi.org/10.1007/BF00189139.
19. M R, S. K.; Schmidova, E.; Konopík, P.; Melzer, D.; Bozkurt, F.; V Londe, N. Fracture Toughness Analysis of Automotive-Grade Dual-Phase Steel Using Essential Work of Fracture (EWF) Method. *Metals* **2020**, *10* (8), 1019. https://doi.org/10.3390/met10081019.
20. Cotterell, B.; Reddel, J. K. The Essential Work of Plane Stress Ductile Fracture. *International Journal of Fracture* **1977**, *13* (3), 267–277. https://doi.org/10.1007/BF00040143.
21. Cotterell, B.; Pardoen, T.; Atkins, A. G. Measuring Toughness and the Cohesive Stress-Displacement Relationship by the Essential Work of Fracture Concept. *Engineering Fracture Mechanics* **2005**, *72* (6 SPEC. ISS.), 827–848. https://doi.org/10.1016/j.engfracmech.2004.10.002.
22. A. S. Tetelman; A. J. McEvily. *Fracture of Structural Materials*; John Wiley & Sons Inc.: New York, 1967.
23. Hosford, W. F.; Atkins, A. G. On Fracture Toughness in Tearing of Sheet Metal. *Journal of Materials Shaping Technology* **1990**, *8* (2), 107–110. https://doi.org/10.1007/BF02833622.
24. Mai, Y.-W.; Cotterell, B. *On the Essential Work of Ductile Fracture in Polymers*; 1986; Vol. 32.
25. Frómeta, D.; Parareda, S.; Lara, A.; Molas, S.; Casellas, D.; Jonsén, P.; Calvo, J. Identification of Fracture Toughness Parameters to Understand the Fracture Resistance of Advanced High Strength Sheet Steels. *Engineering Fracture Mechanics* **2020**, *229*, 106949. https://doi.org/10.1016/j.engfracmech.2020.106949.
26. Clutton, E. Q. ESIS TC4 Experience with the Essential Work of Fracture Method. *European Structural Integrity Society* **2000**, *27* (C), 187–199. https://doi.org/10.1016/S1566-1369(00)80018-7.
27. Clutton, E. Essential Work of Fracture. *European Structural Integrity Society* **2001**, *28* (C), 177–195. https://doi.org/10.1016/S1566-1369(01)80033-9.
28. Atkins, A. G.; Mai, Y. W. Fracture Strains in Sheet Metalforming and Specific Essential Work of Fracture. *Engineering Fracture Mechanics* **1987**, *27* (3), 291–297. https://doi.org/10.1016/0013-7944(87)90147-0.
29. Frómeta, D.; Lara, A.; Grifé, L.; Dieudonné, T.; Dietsch, P.; Rehrl, J.; Suppan, C.; Casellas, D.; Calvo, J. Fracture Resistance of Advanced High-Strength Steel Sheets for Automotive Applications. *Metallurgical and Materials Transactions A: Physical Metallurgy and Materials Science* **2021**, *52* (2), 840–856. https://doi.org/10.1007/s11661-020-06119-y.
30. Frómeta, D.; Tedesco, M.; Calvo, J.; Lara, A.; Molas, S.; Casellas, D. Assessing Edge Cracking Resistance in AHSS Automotive Parts by the Essential Work of Fracture Methodology. *IOP Conf. Series: Journal of Physics: Conf. Series* **2017**, *896*, 12102. https://doi.org/10.1088/1742-6596/896/1/012102.
31. Marchal, Y.; Delannay, F. Influence of Test Parameters on the Measurement of the Essential Work of Fracture of Zinc Sheets. *International Journal of Fracture* **1996**, *80* (4), 295–310. https://doi.org/10.1007/BF00018509.
32. Paton, C. A.; Hashemi, S. Plane-Stress Essential Work of Ductile Fracture for Polycarbonate. *Journal of Materials Science* **1992**, *27* (9), 2279–2290. https://doi.org/10.1007/BF01105033.
33. Hill, R. On Discontinuous Plastic States, with Special Reference to Localized Necking in Thin Sheets. *Journal of the Mechanics and Physics of Solids* **1952**, *1* (1), 19–30. https://doi.org/10.1016/0022-5096(52)90003-3.

34. Williams, J. G.; Rink, M. The Standardisation of the EWF Test. *Engineering Fracture Mechanics* **2007**, *74* (7), 1009–1017. https://doi.org/10.1016/j.engfracmech.2006.12.017.
35. Marchal, Y.; Walhin, J. F.; Delannay, F. Statistical Procedure for Improving the Precision of the Measurement of the Essential Work of Fracture of Thin Sheets. *International Journal of Fracture* **1997**, *87* (2), 189–199. https://doi.org/10.1023/A:1007482121146.
36. Chandra, S. K.; Sarkar, R.; Bhowmick, A. D.; De, P. S.; Chakraborti, P. C.; Ray, S. K. Fracture Toughness Evaluation of Interstitial Free Steel Sheet Using Essential Work of Fracture (EWF) Method. *Engineering Fracture Mechanics* **2018**, *204*, 29–45. https://doi.org/10.1016/j.engfracmech.2018.09.026.
37. Sarkar, R.; Chandra, S. K.; De, P. S.; Chakraborti, P. C.; Ray, S. K. Evaluation of Ductile Tearing Resistance of Dual-Phase DP 780 Grade Automotive Steel Sheet from Essential Work of Fracture (EWF) Tests. *Theoretical and Applied Fracture Mechanics* **2019**, *103*, 102278. https://doi.org/10.1016/j.tafmec.2019.102278.
38. Kamat, S. V.; Hirth, J. P.; Zok, F. W. Effects of Notch Root Radius on Crack Initiation and Growth Toughnesses of a Cross-Ply Ti-6Al-4V/SiC Composite. *Acta Materialia* **1996**, *44* (5), 1831–1838. https://doi.org/10.1016/1359-6454(95)00323-1.
39. Chaudhari, V. V.; Kulkarni, D. M.; Prakash, R. Study of Influence of Notch Root Radius on Fracture Behaviour of Extra Deep Drawn Steel Sheets. *Fatigue & Fracture of Engineering Materials & Structures* **2009**, *32* (12), 975–986. https://doi.org/10.1111/j.1460-2695.2009.01401.x.
40. Faccoli, M.; Cornacchia, C.; Gelfi, M.; Panvini, A.; Roberti, R. Notch Ductility of Steels for Automotive Components. *Engineering Fracture Mechanics* **2014**, *127*, 181–193. https://doi.org/10.1016/j.engfracmech.2014.06.007.
41. Rink, M.; Andena, L.; Marano, C. The Essential Work of Fracture in Relation to J-Integral. *Engineering Fracture Mechanics* **2014**, *127*, 46–55. https://doi.org/10.1016/j.engfracmech.2014.05.006.
42. Luo, Z. C.; Liu, R. D.; Wang, X.; Huang, M. X. The Effect of Deformation Twins on the Quasi-Cleavage Crack Propagation in Twinning-Induced Plasticity Steels. *Acta Materialia* **2018**, *150*, 59–68. https://doi.org/10.1016/j.actamat.2018.03.004.
43. Rice, J. R.; Paris, P. C.; Merkle, J. G. Some Further Results of J-Integral Analysis and Estimates. In *Progress in Flaw Growth and Fracture Toughness Testing*; ASTM International: 100 Barr Harbor Drive, PO Box C700, West Conshohocken, PA 19428-2959, 1973; pp 231–245. https://doi.org/10.1520/STP49643S.
44. Cotterell, B.; Lee, E.; Mai, Y. W. Mixed Mode Plane Stress Ductile Fracture. *International Journal of Fracture* **1982**, *20* (4), 243–250. https://doi.org/10.1007/BF01130611.
45. Magrinho, J. P.; Silva, M. B.; Reis, L.; Martins, P. A. F. Formability Limits, Fractography and Fracture Toughness in Sheet Metal Forming. *Materials* **2019**, *12* (9). https://doi.org/10.3390/ma12091493.
46. Pook, L. P. The Fatigue Crack Direction and Threshold Behaviour of Mild Steel under Mixed Mode I and III Loading. *International Journal of Fatigue* **1985**, *7* (1), 21–30. https://doi.org/10.1016/0142-1123(85)90004-0.
47. ASTM B831-19. *Standard Test Method for Shear Testing of Thin Aluminum Alloy Products*; West Conshohocken, PA, 2019. https://doi.org/10.1520/B0831-19.
48. Banabic, D. Forming Limits of Sheet Metal. In *Formability of Metallic Materials*; Spinger -Verlag Berlin Heidelberg New York: Berlin, 2000; pp 173–214. https://doi.org/10.1007/978-3-662-04013-3_5.
49. Keeler, S. P. Circular Grid System — A Valuable Aid for Evaluating Sheet Metal

Formability. *SAE Transactions* **1968**, *77*, 371–379.
50. Goodwin, G. M. Application of Strain Analysis to Sheet Metal Forming Problems in the Press Shop. In *SAE Technical Papers*; SAE International, 1968. https://doi.org/10.4271/680093.
51. Atkins, A. G. Fracture in Forming. *Journal of Materials Processing Technology* **1996**, *56* (1–4), 609–618. https://doi.org/10.1016/0924-0136(95)01875-1.
52. Isik, K.; Silva, M. B.; Tekkaya, A. E.; Martins, P. A. F. Formability Limits by Fracture in Sheet Metal Forming. *Journal of Materials Processing Technology* **2014**, *214* (8), 1557–1565. https://doi.org/10.1016/j.jmatprotec.2014.02.026.
53. McClintock, F. A. A Criterion for Ductile Fracture by the Growth of Holes. *Journal of Applied Mechanics, Transactions ASME* **1964**, *35* (2), 363–371. https://doi.org/10.1115/1.3601204.
54. Gruben, G.; Fagerholt, E.; Hopperstad, O. S.; Børvik, T. Fracture Characteristics of a Cold-Rolled Dual-Phase Steel. *European Journal of Mechanics, A/Solids* **2011**, *30* (3), 204–218. https://doi.org/10.1016/j.euromechsol.2011.01.004.
55. Tasan, C. C.; Diehl, M.; Yan, D.; Bechtold, M.; Roters, F.; Schemmann, L.; Zheng, C.; Peranio, N.; Ponge, D.; Koyama, M.; Tsuzaki, K.; Raabe, D. An Overview of Dual-Phase Steels: Advances in Microstructure-Oriented Processing and Micromechanically Guided Design. *Annual Review of Materials Research* **2015**, *45* (1), 391–431. https://doi.org/10.1146/annurev-matsci-070214-021103.
56. Huang, T. T.; Gou, R. B.; Dan, W. J.; Zhang, W. G. Strain-Hardening Behaviors of Dual Phase Steels with Microstructure Features. *Materials Science and Engineering A* **2016**, *672*, 88–97. https://doi.org/10.1016/j.msea.2016.06.066.
57. Ingarao, G.; Lorenzo, R. Di; Micari, F. Analysis of Stamping Performances of Dual Phase Steels: A Multi-Objective Approach to Reduce Springback and Thinning Failure. *Materials and Design* **2009**, *30* (10), 4421–4433. https://doi.org/10.1016/j.matdes.2009.04.001.
58. Moćko, W.; Brodecki, A.; Kruszka, L. Mechanical Response of Dual Phase Steel at Quasi-Static and Dynamic Tensile Loadings after Initial Fatigue Loading. *Mechanics of Materials* **2016**, *92*, 18–27. https://doi.org/10.1016/j.mechmat.2015.07.015.
59. Das, A.; Ghosh, M.; Tarafder, S.; Sivaprasad, S.; Chakrabarti, D. Micromechanisms of Deformation in Dual Phase Steels at High Strain Rates. *Materials Science and Engineering A* **2017**, *680*, 249–258. https://doi.org/10.1016/j.msea.2016.10.101.
60. Wang, H. song; Yuan, G.; Kang, J.; Cao, G. ming; Li, C. gang; Misra, R. D. K.; Wang, G. dong. Microstructural Evolution and Mechanical Properties of Dual Phase Steel Produced by Strip Casting. *Materials Science and Engineering A* **2017**, *703*, 486–495. https://doi.org/10.1016/j.msea.2017.07.092.
61. Ennis, B. L.; Bos, C.; Aarnts, M. P.; Lee, P. D.; Jimenez-Melero, E. Work Hardening Behaviour in Banded Dual Phase Steel Structures with Improved Formability. *Materials Science and Engineering A* **2018**, *713*, 278–286. https://doi.org/10.1016/j.msea.2017.12.078.
62. Farzam Rad, V.; Khamedi, R.; Moradi, A. R. The Effect of Martensite Volume Fraction on Topography of Dual Phase Steels. *Materials Letters* **2019**, *239*, 21–23. https://doi.org/10.1016/j.matlet.2018.12.020.
63. SONG, R.; PONGE, D.; RAABE, D. Influence of Mn Content on the Microstructure and Mechanical Properties of Ultrafine Grained C-Mn Steels. *ISIJ International* **2005**, *45* (11), 1721–1726. https://doi.org/10.2355/isijinternational.45.1721.
64. Hickey, J. L. R.; Rouland, S.; Britton, T. B. Heterogeneous Local Plastic Deformation of Interstitial Free Steel Revealed Using In-Situ Tensile Testing and High Angular Resolution Electron Backscatter Diffraction. **2018**.

65. Cooman, B. *Fundamentals of Steel Product Physical Metallurgy*; AIST Association for Iron & Steel Technology: [United States], 2011.
66. Ray, R. K.; Ghosh, P.; Bhattacharjee, D. Effects of Composition and Processing Parameters on Precipitation and Texture Formation in Microalloyed Interstitial Free High Strength (IFHS) Steels. *Materials Science and Technology* **2009**, *25* (9), 1154–1167. https://doi.org/10.1179/174328409X453280.
67. ASTM E8/E8M. *Standard Test Methods for Tension Testing of Metallic Materials*; American Society for Testing and Materials.
68. Official BOC IE Online | BOConline Ireland https://www.boconline.ie/en/ (accessed Nov 1, 2020).
69. *Wire EDM Fundamentals Revolutionizing Machining*.
70. Banu, A.; Ali, M. Y. Electrical Discharge Machining (EDM): A Review. *International Journal of Engineering Materials and Manufacture* **2016**, *1* (1), 3–10. https://doi.org/10.26776/ijemm.01.01.2016.02.
71. Equbal, A.; Sood, A. K. Electrical Discharge Machining: An Overview on Various Areas of Research. *Manufacturing and Industrial Engineering* **2014**, *13* (1–2). https://doi.org/10.12776/mie.v13i1-2.339.
72. Schreier, H.; Orteu, J.-J.; Sutton, M. A.; Michael A., M. A.; Orteu, J.-J.; Schreier, H. W. Introduction. In *Image Correlation for Shape, Motion and Deformation Measurements*; Springer US, 2009; pp 1–12. https://doi.org/10.1007/978-0-387-78747-3_1.
73. Michael A., M. A.; Orteu, J.-J.; Schreier, H. W. Digital Image Correlation (DIC). In *Image Correlation for Shape, Motion and Deformation Measurements*; Springer US: Boston, MA, 2009; pp 1–37. https://doi.org/10.1007/978-0-387-78747-3_5.
74. Schreier, H.; Orteu, J.-J.; Sutton, M. A.; Michael A., M. A.; Orteu, J.-J.; Schreier, H. W. In-Plane Measurements. In *Image Correlation for Shape, Motion and Deformation Measurements*; Springer US, 2009; pp 1–55. https://doi.org/10.1007/978-0-387-78747-3_6.
75. Schwarzer, R. A.; Field, D. P.; Adams, B. L.; Kumar, M.; Schwartz, A. J. Present State of Electron Backscatter Diffraction and Prospective Developments. In *Electron Backscatter Diffraction in Materials Science*; Springer US, 2009; pp 1–20. https://doi.org/10.1007/978-0-387-88136-2_1.
76. NISHIKAWA, S.; KIKUCHI, S. Diffraction of Cathode Rays by Calcite. *Nature* **1928**, *122* (3080), 726–726. https://doi.org/10.1038/122726a0.
77. Mason, J. K.; Schuh, C. A. Representations of Texture. In *Electron Backscatter Diffraction in Materials Science*; Springer US, 2009; pp 35–51. https://doi.org/10.1007/978-0-387-88136-2_3.
78. McNelley, T. R.; Zhilyaev, A. P.; Swaminathan, S.; Su, J.; Menon, E. S. Application of EBSD Methods to Severe Plastic Deformation (SPD) and Related Processing Methods. In *Electron Backscatter Diffraction in Materials Science*; Springer US, 2009; pp 277–289. https://doi.org/10.1007/978-0-387-88136-2_20.
79. Dingley, D. J.; Wright, S. I. Phase Identification through Symmetry Determination in EBSD Patterns. In *Electron Backscatter Diffraction in Materials Science*; Springer US, 2009; pp 97–107. https://doi.org/10.1007/978-0-387-88136-2_7.
80. John Humphreys; Gregory S. Rohrer; Anthony Rollett. *Recrystallization and Related Annealing Phenomena | ScienceDirect*, 3rd ed.; Elsevier: Amsterdam, 2017.
81. Sobotka, J.; Solfronk, P.; Kolnerová, M.; Zuzánek, L. UTILIZATION OF THE CONTACT-LESS OPTICAL SYSTEM FOR THE BORE EXPANSION TEST. In *22nd-International Conference on Metallurgy and Materials*; TANGER: Brno, 2013; pp 845–850.
82. Bergs, T.; Nick, M.; Trauth, D.; Klocke, F. Damage Evolution in Nakajima Tests of

DP800 Dual Phase Steel. In *IOP Conference Series: Materials Science and Engineering*; Institute of Physics Publishing, 2018; Vol. 418. https://doi.org/10.1088/1757-899X/418/1/012048.

83. Martínez, A. B.; Segovia, A.; Gamez-Perez, J.; Maspoch, M. L. Influence of Femtolaser Notch Sharpening Technique in the Determination of Essential Work of Fracture (EWF) Parameters. *Engineering Fracture Mechanics* **2009**, *76* (9), 1247–1254. https://doi.org/10.1016/j.engfracmech.2009.01.015.
84. Dlouhy, I.; Tarafder, M.; Hadraba, H. Micromechanical Aspects of Transgranular and Intergranular Failure Competition. In *Key Engineering Materials*; Trans Tech Publications Ltd, 2011; Vol. 465, pp 399–402. https://doi.org/10.4028/www.scientific.net/KEM.465.399.
85. Nakada, N.; Arakawa, Y.; Park, K. S.; Tsuchiyama, T.; Takaki, S. Dual Phase Structure Formed by Partial Reversion of Cold-Deformed Martensite. *Materials Science and Engineering A* **2012**, *553*, 128–133. https://doi.org/10.1016/j.msea.2012.06.001.
86. Delincé, M.; Bréchet, Y.; Embury, J. D.; Geers, M. G. D.; Jacques, P. J.; Pardoen, T. Structure-Property Optimization of Ultrafine-Grained Dual-Phase Steels Using a Microstructure-Based Strain Hardening Model. *Acta Materialia* **2007**, *55* (7), 2337–2350. https://doi.org/10.1016/j.actamat.2006.11.029.
87. Son, Y. Il; Lee, Y. K.; Park, K. T.; Lee, C. S.; Shin, D. H. Ultrafine Grained Ferrite-Martensite Dual Phase Steels Fabricated via Equal Channel Angular Pressing: Microstructure and Tensile Properties. *Acta Materialia* **2005**, *53* (11), 3125–3134. https://doi.org/10.1016/j.actamat.2005.02.015.
88. Calcagnotto, M.; Adachi, Y.; Ponge, D.; Raabe, D. Deformation and Fracture Mechanisms in Fine- and Ultrafine-Grained Ferrite/Martensite Dual-Phase Steels and the Effect of Aging. *Acta Materialia* **2011**, *59* (2), 658–670. https://doi.org/10.1016/j.actamat.2010.10.002.
89. Dillien, S.; Seefeldt, M.; Allain, S.; Bouaziz, O.; Van Houtte, P. EBSD Study of the Substructure Development with Cold Deformation of Dual Phase Steel. *Materials Science and Engineering A* **2010**, *527* (4–5), 947–953. https://doi.org/10.1016/j.msea.2009.09.009.
90. Maitland, T.; Sitzman, S. Backscattering Detector and EBSD in Nanomaterials Characterization. In *Scanning Microscopy for Nanotechnology: Techniques and Applications*; Springer New York, 2007; pp 41–75. https://doi.org/10.1007/978-0-387-39620-0_2.
91. Han, H.; Rollett, A.; Kim, D.; Oh, K. H.; Lebensohn, R. Subgrain Texture Evolution during Biaxial Deformation in Interstitial Free and Dual Phase Steels; 2009.
92. Anindya Das. High Strain Rate Deformation of Automotive Grade Steels, IIT, Kharagpur, 2019.
93. Bergström, Y.; Granbom, Y.; Sterkenburg, D. A Dislocation-Based Theory for the Deformation Hardening Behavior of DP Steels: Impact of Martensite Content and Ferrite Grain Size. *Journal of Metallurgy* **2010**, *2010*, 1–16. https://doi.org/10.1155/2010/647198.
94. Ghosh, S.; Mula, S. Fracture Toughness Characteristics of Ultrafine Grained Nb–Ti Stabilized Microalloyed and Interstitial Free Steels Processed by Advanced Multiphase Control Rolling. *Materials Characterization* **2020**, *159*, 110003. https://doi.org/10.1016/j.matchar.2019.110003.
95. Dasharath, S. M.; Mula, S. Improvement of Mechanical Properties and Fracture Toughness of Low SFE Cu-Al Alloy through Microstructural Modification by Multiaxial Cryoforging. *Materials Science and Engineering A* **2017**, *690*, 393–404. https://doi.org/10.1016/j.msea.2017.03.034.

96. Deeparekha, N.; Gupta, A.; Demiral, M.; Khatirkar, R. K. Cold Rolling of an Interstitial Free (IF) Steel—Experiments and Simulations. *Mechanics of Materials* **2020**, *148*, 103420. https://doi.org/10.1016/j.mechmat.2020.103420.
97. Khatirkar, R.; Vadavadagi, B.; Haldar, A.; Samajdar, I. ND//<111> Recrystallization in Interstitial Free Steel: The Defining Role of Growth Inhibition. *ISIJ International* **2012**, *52* (5), 894–901. https://doi.org/10.2355/isijinternational.52.894.
98. Cruz-Gandarilla, F.; Salcedo-Garrido, A. M.; Bolmaro, R. E.; Baudin, T.; De Vincentis, N. S.; Avalos, M.; Cabañas-Moreno, J. G.; Mendoza-Leon, H. Microstructural Evolution and Mechanical Properties on an ARB Processed If Steel Studied by X-Ray Diffraction and EBSD. *Materials Characterization* **2016**, *118*, 332–339. https://doi.org/10.1016/j.matchar.2016.05.025.
99. Hanamura, T.; Yin, F.; Nagai, K. Ductile-Brittle Transition Temperature of Ultrafine Ferrite/Cementite Microstructure in a Low Carbon Steel Controlled by Effective Grain Size. *ISIJ International* **2004**, *44* (3), 610–617. https://doi.org/10.2355/isijinternational.44.610.
100. Kadkhodapour, J.; Butz, A.; Ziaei Rad, S. Mechanisms of Void Formation during Tensile Testing in a Commercial, Dual-Phase Steel. *Acta Materialia* **2011**, *59* (7), 2575–2588. https://doi.org/10.1016/j.actamat.2010.12.039.
101. Silva, M. B.; Martínez-Donaire, A. J.; Centeno, G.; Morales-Palma, D.; Vallellano, C.; Martins, P. A. F. Recent Approaches for the Determination of Forming Limits by Necking and Fracture in Sheet Metal Forming. In *Procedia Engineering*; Elsevier Ltd, 2015; Vol. 132, pp 342–349. https://doi.org/10.1016/j.proeng.2015.12.504.

PUBLICATIONS

1. M. R. Sunilkumar, Schmidova E, Konopík P, Melzer D. Fracture toughness examination of dual-phase and interstitial free steel using essential work of fracture method. Fatigue and Fracture of Engineering Materials and Structures. 2021;1-17. https://doi.org/ 10.1111/ffe.13555

2. M. R. Sunilkumar; Schmidova. E.; Konopík. P.; Melzer. D.; Bozkurt. F.; V Londe. N. Fracture Toughness Analysis of Automotive-Grade Dual-Phase Steel Using Essential Work of Fracture (EWF) Method. *Metals* **2020**. *10* (8). 1019. https://doi.org/10.3390/met10081019.

3. Schmidová. E.; Bozkurt. F.; Culek. B.; Kumar. S.; Kuchariková. L.; Uhríčik. M. Influence of Welding on Dynamic Fracture Toughness of Strenx 700MC Steel. *Metals* **2019**. *9* (5). 494. https://doi.org/10.3390/met9050494

4. Schmidová. E.; Sunil Kumar. M. R.; Schmid. M.; Bozkurt. F. Role of Nb in the Failure of Dual-Phase Steel in Heterogeneous Welds. *Engineering Failure Analysis* **2020**. *116*. 104708. https://doi.org/10.1016/j.engfailanal.2020.104708.

5. Sunil Kumar Meluru Ramesha; Eva Schmidova. Strength and Fracture Behaviour of Dual Phase Steel Dp450 in Static and Dynamic Conditions. *Communications - Scientific letters of the University of Zilina* **2019**. *21* (4). 63–68. https://doi.org/10.26552/com.c.2019.4.63-68.

6. Sunil Kumar. M. R.; Schmidova. E. Deformation Response of Dual Phase Steel in Static and Dynamic Conditions. *Applied Engineering Letters : Journal of Engineering and Applied Sciences* **2019**. *4* (2). 41–47. https://doi.org/10.18485/aeletters.2019.4.2.1

7. M.R. Sunilkumar, Schmidová. E, Culek. B, Hojka. P. Dynamic Strength and Fracture Behaviour of Dual-Phase High Strength Steel under High Strain Rate. *METAL 2019 - 28th International Conference on Metallurgy and Materials. Conference Proceedings 2019.* **2019**. 538–543.

8. Bozkurt. F.; Çakir. F. H.; Schmidova. E.; Sunil Kumar. M. R. The Effect of Welding Parameters on Static and Dynamic Behaviors of Spot Welded Ti6Al4V Sheets. *Journal of Materials Engineering and Performance* **2020**. 1–12. https://doi.org/10.1007/s11665-020-05202-0